Dissertations - ALL   SURFACE

December 2019

Digital Readout and Control of a Superconducting Qubit

Caleb Jordan Howington
Syracuse University

ABSTRACT

In the quest to build a fault-tolerant quantum computer, superconducting circuits based on Josephson junctions have emerged as a leading architecture. Coherence times have increased significantly over the last two decades, and processors with ~ 50 qubits have been experimentally demonstrated. These systems traditionally utilize microwave frequency control signals, and heterodyne based detection schemes for measurement. Both of these techniques rely heavily on room temperature microwave generators, high-bandwidth lines from room temperature to millikelvin temperatures, and bulky non-reciprocal elements such as cryogenic microwave isolators. Reliance on these elements makes it impractical to scale existing devices up a single order of magnitude, let alone the 5-6 orders of magnitude needed for performing fault-tolerant quantum algorithms. Here, I present results that suggesting superconducting digital logic, namely Single Flux Quantum (SFQ) logic, can replace analog control and measurement techniques, avoiding the significant overhead involved. I describe a scheme for measuring qubits with a device known as a Josephson Photomultiplier (JPM), which crucially stores the result of a qubit measurement in a classical circulating supercurrent within the device and allows for integration with SFQ detection circuitry. This technique is experimentally demonstrated, with single-shot measurement fidelity of 92%. Two methods for accessing this measurement result are presented, one utilizing ballistic fluxons, and another utilizing flux comparison. Initial experimental results of the latter are presented. In addition, I describe a scheme for controlling qubits with sequences of digital SFQ pulses. This method is then used to control a qubit without a microwave signal generator, with results of an average single-qubit gate fidelity of around 95%. When combined, these techniques form a nearly fully digital interface to superconducting qubits, which could allow these systems to scale much more easily.

DIGITAL READOUT AND CONTROL

OF A SUPERCONDUCTING QUBIT

by

Caleb Jordan Howington

B.S., Rensselaer Polytechnic Institute, 2013

Dissertation

Submitted in partial fulfillment of the requirements for the degree of
Doctor of Philosophy in Physics

Syracuse University

December 2019

Acknowledgments

Contents

List of Figures

List of Tables

Chapter 1

Introduction

Typical introductions into the field of quantum computing begin with a reference to Moore's Law, the technological phenomenon of transistor count density doubling every two years[1]. This trend, which has held true for over 5 decades, has resulted in the explosion of computer technology that has revolutionized civilization within the past century. As of this writing, commercial foundries have started offering MOSFET [1] fabrication processes utilizing **5-7 nm** nodes, which roughly correspond to the size of the transistor. Indeed, transistors that are only a handful atoms in size surely cannot be made much smaller. Even if fabrication techniques are developed to reduce this scale further, quantum effects start to dominate the behavior once sizes are reduced to **3 nm** or so (in this context quantum effects are problematic).

However, transistor density is no longer the main catalyst for computational advancement. Rather, the advancement of complementary hardware technologies such as GPUs and distrubuted computing, and new advancements in computer science such as general algorithm development, machine learning, and cloud computing, have kept computational advancements progressing at a break-neck speed. It is not necessarily the hardware that is most critical when solving the problem, it is how the hardware is used. In short, *how* one computes is important. Clever programming that reduces the complexity of an algorithm from exponential to polynomial time is significantly more useful than doubling the size or speed of the processor running the algorithm.

---

[1]Metal-Oxide-Semiconductor Field-Effect-Transistor

With this in mind, it should be emphasized that quantum computing is not the answer to transistor count. It is another, very specific manner for *how* one can compute. Quantum computers are not replacements for classical computers. They are another tool in a toolbox, especially suited to solve certain types of problems. Luckily, some of these problems happen to be exceedingly important ones. As a conventional example, modern cryptography is based on the difficulty of factoring long numbers into their prime constituents. Quantum computers of a modest size[2] can theoretically factor these long numbers in polynomial time using Shor's algorithm, rendering the entire RSA cryptosystem essentially useless [3, 4].

Other, more near term algorithms are much more scientifically interesting. It is likely that the most significant breakthroughs on near-term NISQ[3] will be in simulating other quantum systems . Quantum simulation is notoriously hard to perform classically, and useful quantum simulations can be performed using orders of magnitude less qubits than what would be required to perform the aforementioned Shor's algorithm[5].

While there have been many physical implementations of quantum computers over the years, the two current leading approaches are those utilizing ion traps, and superconducting circuits. For the rest of this work, I'll be focusing on the superconducting circuit approach. As of this writing, superconducting quantum computers have been demonstrated with roughly 50 qubits [6, 7]. These devices are already large enough that they cannot be directly simulated classically. Recent results have demonstrated a quantum sampling problem[4] that takes 200 seconds on a 53 qubit processor, compared to an estimated 10,000 years on a state-of-the-art supercomputer [6]. It is likely that either this generation or the next will provide the first demonstration of useful computations that are infeasible on even the largest supercomputers.

---

[2]After reading this thesis, the reader can decide whether the 4096 logical qubits needed to factor 2048-bit RSA numbers should be referred to as 'modest', especially considering error correcting codes require roughly 10×10^8 physical qubits [2] in order to form these logical qubits.

[3]Noisy Intermediate-Scale Quantum. Notably, devices without significant error correction.

[4]It should be noted that this sampling problem was specifically chosen to be hard to simulate classically. It is not a particularly useful algorithm.

So, what exactly is a quantum computer? A loose description can be that a quantum computer is a computer that takes advantage of quantum mechanics in some way. Traditionally this is taken to mean that the device leverages quantum phenomena such as superpositions and entanglement in order to perform computations. If a classical bit is quantized, meaning its computational basis states are eigenstates, then we can write the state of the quantum bit (qubit) as

$$|\psi\rangle = \alpha |0\rangle + \beta |1\rangle = \begin{pmatrix} \alpha \\ \beta \end{pmatrix}, \tag{1.1}$$

where $|0\rangle$ and $|1\rangle$ are the eigenstates $\begin{pmatrix} 1 \\ 0 \end{pmatrix}$ and $\begin{pmatrix} 0 \\ 1 \end{pmatrix}$, respectively. Operations on this two state vector are represented by 2×2 unitary matrices, e.g., the Pauli matrices

$$\sigma_x = \begin{pmatrix} 0 & 1 \\ 1 & 0 \end{pmatrix} \quad \sigma_y = \begin{pmatrix} 0 & -i \\ i & 0 \end{pmatrix} \quad \sigma_z = \begin{pmatrix} 1 & 0 \\ 0 & -1 \end{pmatrix}. \tag{1.2}$$

It follows that a two-qubit state can be written as

$$|\psi_1\psi_2\rangle = \alpha |00\rangle + \beta |01\rangle + \gamma |10\rangle + \delta |11\rangle, \tag{1.3}$$

with two-qubit operations becoming 4×4 unitary matrices, e.g.,

$$\text{CNOT} = \begin{pmatrix} 1 & 0 & 0 & 0 \\ 0 & 1 & 0 & 0 \\ 0 & 0 & 0 & 1 \\ 0 & 0 & 1 & 0 \end{pmatrix}, \tag{1.4}$$

which as the name implies, performs a Controlled-NOT gate, flipping the state of $|\psi_2\rangle$ only if $|\psi_1\rangle = |1\rangle$. While this is simply an analog of a classical reversible logic gate, purely quantum gates can also be constructed, such as the Controlled-Z, or CPhase, gate

$$
\text{CZ} = \begin{pmatrix} 1 & 0 & 0 & 0 \\ 0 & 1 & 0 & 0 \\ 0 & 0 & 1 & 0 \\ 0 & 0 & 0 & -1 \end{pmatrix},
\tag{1.5}
$$

which applies a phase rotation to $|\psi_2\rangle$ only if $|\psi_1\rangle = |1\rangle$. The peculiarities of quantum information can already be appreciated. Instead of an n-bit classical register, which has n entries, an n-qubit system is described by a state vector with 2^n entries. This computational space quickly becomes massive, with 50 qubits having over 10^{15} entries. Indeed, even the largest supercomputers available at present struggle with simulating qubit systems of around this size [8].

1.1   Scope of dissertation

The fundamental requirements for building a useful quantum computer have been canonized in the DiVencenzo Criteria, listed below [9].

The DiVencenzo Criteria

1. A scalable physical system with well-characterized qubits.

2. The ability to initialize the state of the qubits.

3. A universal set of quantum gates.

4. Long relevant decoherence times, much longer than the gate-operation time.

5. A qubit-specific measurement capability.

The work presented here aims to address criteria 3 and 5, within the context of criterion 1. The word scalable is particularly emphasized here.

For the remainder of this chapter, I will describe the physical system of qubits widely used in the field of superconducting quantum computing. I will also introduce a classical superconducting digital logic family that I have been working to integrate with superconducting qubits. Lastly, a general architecture is described for combining this superconducting digital logic with superconducting qubits, forming a fully integrated, cryogenic, hybrid quantum-classical processor.

In Chapter 2, I will give an outline of standard control techniques for applying quantum gates. An alternative method involving digital control is then described, and experimental results presented.

In Chapter 3, the measurement criterion is addressed. Conventional microwave techniques are described, and critically challenged from a scalability perspective. An alternative qubit measurement technique utilizing a Josephson Photomultiplier is described, with experimental results presented.

Chapter 4 presents one possible method for converting the result of a Josephson Photomultiplier-based qubit measurement to a digital signal utilizing ballistic fluxons.

Chapter 5 presents a similar approach utilizing an SFQ flux comparator rather than ballistic fluxons. This approach is experimentally demonstrated and results are discussed.

In Chapter 6, I give an overview of a general architecture for creating a cryogenic, digital interface based on superconducting digital logic.

The ideas and results presented here have been published in the following manuscripts [10–12].

1.2   Superconducting Circuits

The phenomenon of superconductivity, first discovered in 1911 by Kamerlingh Onnes [13], results in zero dc electric resistance, and almost perfect diamagnetic behavior. Superconductivity can be

achieved by cooling certain materials below a critical temperature. Superconductivity has been demonstrated in a variety of materials ranging from traditional metals like aluminum and niobium, to more exotic and newer materials such as graphene and yttrium-barium-copper-oxide [14]. The use of superconductors in digital electronics was not suggested until 1956 with the introduction of the cryotron [15]. Since then, a host of superconducting digital logic families have been developed, with varying levels of success. An interested reader is directed to [16] for an overview of superconducting electronics. The common element across all of these superconducting logic families is a device known as a Josephson junction, which is introduced below.

1.2.1   Josephson Junctions
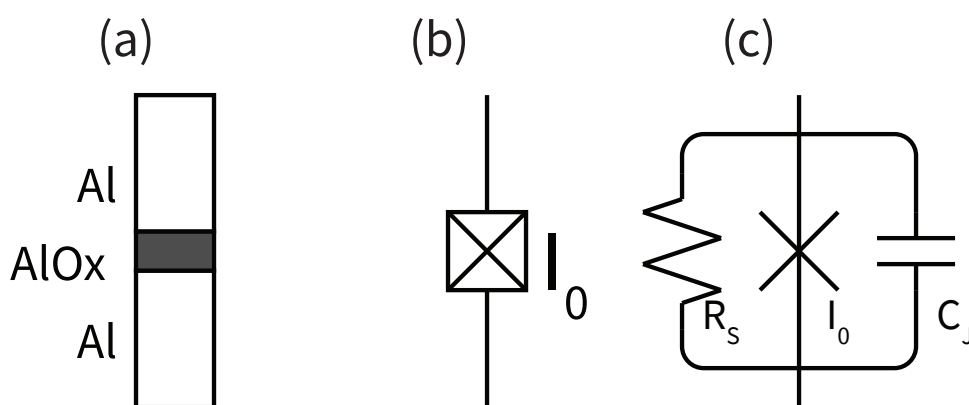
Figure 1.1: The Josephson junction is the fundamental building block of superconducting electronics. (a) Example of a Josephson junction. Two aluminum wires connected through an insulating AlOx barrier. (b) Circuit symbol for a junction. (c) Resistively and Capacitively Shunted Junction (RCSJ Model).

The fundamental building block of superconducting electronics is the Josephson junction [17]. The junction consists of two superconducting electrodes with a thin insulating barrier between them (Figure 1.1). The Cooper pairs on either side of the barrier can be described by indivdual wavefunctions with a phase difference φ. The dynamics of Josephson junctions are governed by the following two Josephson relations [18], the first of which defines the voltage across the junction as a function

of the phase dynamics. Notably, a phase dependence linear in time results in a constant voltage

$$V(t) = \frac{\Phi_0}{2\pi} \frac{\partial \varphi(t)}{\partial t}. \tag{1.6}$$

The constant in this equation is the magnetic flux quantum, $\Phi_0 = h/2e$.

The second Josephson relation defines the current flowing through the junction as a function of the phase, and some critical current I_0

$$I(t) = I_0 \sin \varphi(t). \tag{1.7}$$

It is also convenient to think of a Josephson junction as a non-linear inductor. A conventional inductance is represented by the relation between the voltage and time derivative of the current. Using the chain rule we can see

$$V = L \frac{\partial I}{\partial t} \tag{1.8}$$

$$V = L \frac{\partial I}{\partial \varphi} \frac{\partial \varphi}{\partial t}. \tag{1.9}$$

Using Eq. 1.6 to rewrite V, we can define a Josephson inductance given by

$$L_J(\varphi) = \frac{\Phi_0}{2\pi I_0 \cos \varphi(t)}. \tag{1.10}$$

The potential energy of this inductance can be found using Equations 1.6 and 1.7,

$$U(\varphi) = \int I(\varphi) V(\varphi) \, dt \tag{1.11}$$

$$= \int (I_0 \sin \varphi) \left(\frac{\Phi_0}{2\pi} \frac{\partial \varphi}{\partial t} \right) dt \tag{1.12}$$

$$= \frac{I_0 \Phi_0}{2\pi} \int \sin \varphi \, d\varphi \tag{1.13}$$

$$= -E_J \cos \varphi, \tag{1.14}$$

where we have introduced a Josephson energy

$$E_J = \frac{I_0 \Phi_0}{2\pi}. \tag{1.15}$$

It is also helpful to introduce a flux, defined as $\Phi = \int V(t) dt$. Integrating Eq. 1.6 results in

$$\varphi(t) = \frac{2\pi \Phi(t)}{\Phi_0}. \tag{1.16}$$

Josephson junctions are often characterized by their critical currents. The critical current is related to the room temperature resistance of the insulating barrier and the superconducting gap of the superconducting electrodes. The critical current multiplied by the normal state resistance defines a constant characteristic voltage of the junction [19]

$$V_c \equiv I_0 R_n = \frac{\pi \Delta(T)}{2e}. \tag{1.17}$$

Josephson junctions are primarily thought of as nonlinear inductors, but there is also an unavoidable capacitance between the two electrodes. This capacitance and inductance result in a fundamental frequency known as the plasma frequency of the junction. Since the critical current and ca-

pacitance both scale linearly with junction area, the size dependence cancels out and the plasma frequency is just a function of the critical current density J_c and the specific capacitance C_A of the insulating barrier, and should be nominally identical for all junctions defined in the same oxidation step

$$\omega_p = \frac{1}{\tau_p} \equiv 1/\sqrt{L_J C_J} = \sqrt{\frac{2\pi I_0}{\Phi_0 C_J}} = \sqrt{\frac{2\pi J_c}{\Phi_0 C_A}}. \tag{1.18}$$

When Josephson junctions are integrated into circuits, they often have some bias current I_b applied to them. It is useful to think of the phase of the junction as a particle in a particular potential. In this case, the phase particle is in a tilted washboard potential given by

$$
\begin{aligned}
U_J(\varphi) &= \int \left[I(\varphi) + I_b \right] V(\varphi) \, \mathrm{d}t \\
&= \int I(\varphi) V(\varphi) \, \mathrm{d}t + \int I_b V(\varphi) \, \mathrm{d}t \\
&= -E_J \left(\cos\varphi + \frac{I_b}{I_0} \varphi \right).
\end{aligned}
\tag{1.19}
$$

When the critical current of a junction is exceeded, the phase particle leaves the well, and the junction develops a non-zero voltage. For sufficiently weak damping, the phase particle is essentially skipping down the titled washboard at some velocity $\mathrm{d}\varphi/\mathrm{d}t$, leading to a voltage given by Eq. 1.6. Reducing I_b below I_0 does not necessarily re-trap the particle in one of the wells of the washboard. Rather, the inertia of the particle, related to the capacitance C_J can keep the junction in the voltage state, until a value lower, re-trapping current is reached. This hysteresis is measurable in a standard IV measurement, where the probe current is increased above I_0, and then reduced back to zero.

In some cases, this hysteresis is unfavorable. For example, in the digital logic discussed later in this chapter, the speed at which junctions can switch sequentially defines the rough speed limit of the

circuit. Therefore it is preferred for the junction to reset to its superconducting state as quickly as possible, and without needing to adjust any bias currents. In this case, a shunt resistor R_s can be added in parallel with the junction. This resistor leads to an LR time constant, often converted as a characteristic frequency ω_c, or characteristic voltage V_c

$$\omega_c = \frac{1}{\tau_c} \equiv \frac{R_S}{L_J} = \frac{2\pi}{\Phi_0} V_c. \tag{1.20}$$

Along the same lines, an RC time constant can be defined and related with the plasma frequency and characteristic frequency

$$\omega_{RC} = \frac{1}{\tau_{RC}} \equiv \frac{1}{R_S C_J} = \frac{\omega_p^2}{\omega_c}. \tag{1.21}$$

These frequencies are commonly represented by a dimensionless parameter known as the Stewart-McCumber Parameter,

$$\beta_c \equiv \frac{\omega_c^2}{\omega_p^2} = \frac{\omega_c}{\omega_{RC}} = \frac{2\pi}{\Phi_0} I_0 R_S^2 C_J, \tag{1.22}$$

which is a measure of the damping of the junction. A junction with $\beta_c \gg 1$ is underdamped and will experience hysteresis. A $\beta_c \ll 1$ is strongly damped and will not. Typical shunted junctions target a critical damping of $\beta_c \approx 1$.

1.2.2   Superconducting Qubits

With the Josephson junction added to our superconducting circuit toolbox (along with superconducting capacitors and inductors), non-linear circuits can be treated as potential qubits. Historically, the first qubit was a small superconducting island shorted to ground with a Josephson junc-

tion loop: the Cooper pair box [20]. This was the first charge qubit and paved the way for the rapid development of qubits over the next two decades.

The Hamiltonian for charge qubits can be developed from the Hamiltonian of a Josephson junction. In its superconducting state, the Josephson junction is simply a capacitance and a non-linear inductor (see Figure 1.1), with values given by its area and critical current density. The kinetic energy of the system is determined by the capacitance C, as well as an offset charge from a gate electrode q_g. Remembering that the charge in a superconductor is that of a Cooper pair with charge $2e$, we can write this charging energy as

$$T(N) = \frac{1}{2}\frac{Q^2}{C} \tag{1.23}$$

$$= \frac{1}{2}\frac{(Q - q_g)^2}{C} \tag{1.24}$$

$$= \frac{1}{2}\frac{4e^2}{C}(N - n_g)^2 \tag{1.25}$$

$$= 4E_c(N - n_g)^2, \tag{1.26}$$

where we have rewritten the charge in terms of number of Cooper pairs, and used E_c as the standard charging energy of the junction capacitance.

We can now write the Hamiltonian as the sum of this kinetic energy and the potential energy derived in Equation 1.11

$$H_{charge}(N, \varphi) = 4E_C \left(N - n_g\right)^2 - E_J \cos \varphi. \tag{1.27}$$

While not developed here, it should be emphasized that in a full quantum-mechanical treatment of this system, the charge (or number of Cooper pairs N) and the phase (or the flux $\Phi = \Phi_0\varphi/2\pi$) are quantum operators and conjugate variables that satisfy the standard commutation and uncertainty

relations. For a thorough formulation, the interested reader is encouraged to follow [21].

Superconducting flux qubits were also developed and demonstrated to have longer coherence times than the Cooper pair box, which suffered from a strong sensitivity to charge noise. Instead of utilizing the charge (number of Cooper pairs) as a quantum variable, these qubits utilize the flux in a superconducting loop. Flux qubit variants are still used today [22], with coherence times near the state-of-the-art in superconducting devices [23].

Another qubit variety, the phase qubit, is based on the phase across a biased junction rather than charge or flux. Early generations were simply current-biased Josephson junctions [24]. Later designs used a flux-biased junction, with a shunt inductor added to form an rf SQUID [25]. In these phase qubits, one of the wells in a double well potential is treated as an anharmonic ladder of energy states. The lowest two energy levels are treated as the qubit basis state. Quantum states can be prepared by driving the circuit at this frequency, and readout is performed by biasing the double-well to a value where higher excited states tunnel into the adjacent energy well, while the ground state remains in the initial well. The Hamiltonian is given by

$$H(Q, \varphi) = \frac{Q^2}{2C} - E_J \cos \varphi + \frac{1}{2L} \left(\frac{\Phi_0}{2\pi} \right)^2 \left(\varphi - \frac{2\pi\Phi_e}{\Phi_0} \right)^2, \qquad (1.28)$$

where L is the shunt inductance of the rf SQUID. In order to bring the frequency of these qubits down to the microwave regime, large shunt capacitors are added. These large capacitors cannot be easily realized with planar devices, and therefore require a lossy dielectric in order to make a parallel-plate capacitor. This loss limits the coherence time of phase qubits to be significantly less than charge or flux qubits, and consequently they have fallen out of fashion, although they can be leveraged as non-qubit devices (see Section 3.2).
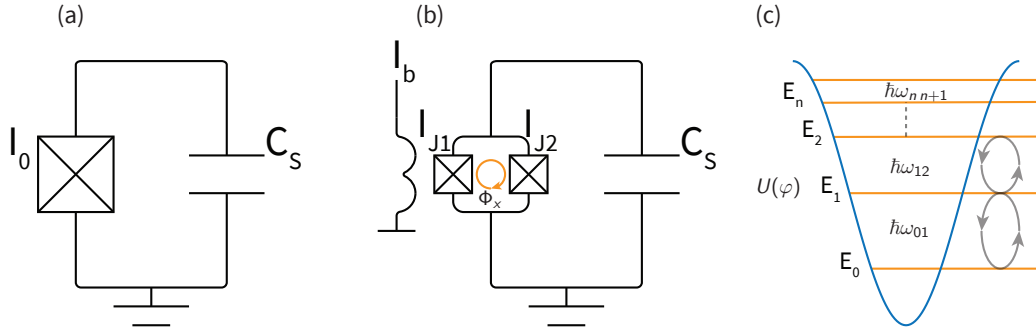
Figure 1.2: Circuit diagram of (a) a fixed-frequency transmon qubit , (b) tunable transmon qubit. (c) Energy potential of a transmon qubit, with anharmonic energy levels shown.

1.2.3   The Transmon

The introduction of the transmon qubit in 2007 [26] allowed for superconducting qubits with coherence times in the 10-100 μs range. By shunting a Cooper pair box with a large capacitance (Figure 1.2), one can make a qubit that is insensitive to charge noise. Over the past 12 years, this qubit design has become the standard-bearer of superconducting qubits.

The frequency of a transmon is that of an anharmonic LC oscillator, where the inductance is provided by the Josephson junctions. It can also be represented in terms of the Josephson energy $E_J = \Phi_0 I_0 / 2\pi$ and charging energy $E_c = e^2 / 2C_\Sigma$, where $C_\Sigma = C_s + C_J$ is the total capacitance of the qubit including the junction capacitance. This frequency is given by

$$\omega_q = 1/\sqrt{L_J C_\Sigma} = \left(\sqrt{8 E_J E_c} - E_c \right) / \hbar. \tag{1.29}$$

It is often useful to be able to adjust the frequency of a transmon, either to perform gates or to compensate for fabrication scatter. By using a pair of junctions, an external flux Φ_e can tune the effective critical current, and therefore the Josephson energy of the qubit. The new Hamiltonian becomes

$$H \quad = \quad 4E_C n^2 - E_{J\Sigma}\sqrt{\cos^2\left(\frac{\pi\Phi_e}{\Phi_0}\right) + d^2\sin^2\left(\frac{\pi\Phi_e}{\Phi_0}\right)}\cos\left(\frac{2\pi\Phi}{\Phi_0}\right) \tag{1.30}$$

$$\quad = \quad 4E_C n^2 - E'_J(\Phi_e)\cos\left(\frac{2\pi\Phi}{\Phi_0}\right), \tag{1.31}$$

where $E_{J\Sigma} = E_{J1} + E_{J2}$ and $d = (\gamma - 1)/(\gamma + 1), \gamma = E_{J2}/E_{J1}$ is the junction ratio. Replacing E_J with

$$E'_J(\Phi_e) = E_{J\Sigma}\sqrt{\cos^2\left(\frac{\pi\Phi_e}{\Phi_0}\right) + d^2\sin^2\left(\frac{\pi\Phi_e}{\Phi_0}\right)} \tag{1.32}$$

in 1.29 gives a tunable frequency

$$\omega_q(\Phi_e) = \left(\sqrt{8E'_J(\Phi_e)E_c} - E_c\right)/\hbar. \tag{1.33}$$

1.2.4 The Rectmon

Many of the previous qubit designs used in our group were floating, without a galvanic connection to ground. For the experiments discussed in later chapters, a new qubit geometry was needed. In particular, the goal was to design a tunable transmon that could be coupled at multiple points to a planar resonator. In order to minimize the potential for slot-line modes and other stray resonances, it was ideal to have a grounded qubit, with an unbroken ground plane surrounding the qubit island. A rectangular geometry was used, to enable capacitive coupling between the qubit island and the center conductor of a coplanar resonator. A rough design geometry was parametrized in ANSYS Q3D, and optimized to generate the target capacitance values. The new geometry, dubbed the rectmon, is shown in Figure 1.3.
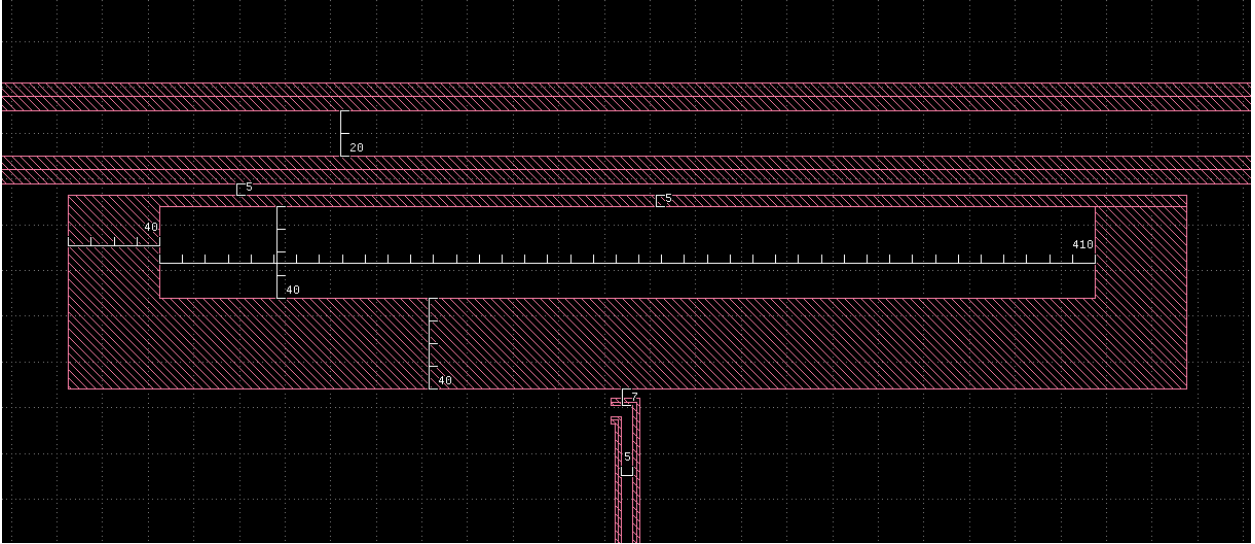
Figure 1.3: Rectmon geometry generated with Q3D. A rectangular island is placed in a rectangular pocket with a capacitance to ground C_S. A flux-bias line tunes a SQUID loop which shorts the island to the ground plane.

To verify the design, this device was fabricated (See Appendix 1) and cooled down in a dilution refrigerator to be measured at 25 mK. Further details into qubit control and readout techniques are discussed in Sections 2.1 and 3.1, respectively.

The coherence of qubits, or the measure of how well a qubit's quantum state persists with time, is characterized by a standard set of lifetimes. In the absence of decoherence, a qubit prepared into any excited state ($|\psi\rangle = \alpha |0\rangle + \beta |1\rangle$, where $\beta \neq 0$), will remain in this state until subsequent manipulation. However, in the presence of dissipation and low-frequency noise, the qubit state will change in time at some rate. The rate that the qubit relaxes to its ground state is described by the coherence time T_1,

$$\Gamma_1 \equiv \frac{1}{T_1}. \tag{1.34}$$

To experimentally measure T_1, the qubit is rotated by π about the X or Y axis, and a measurement of the qubit is performed at some later time t. The probability of finding the qubit in its excited state as a function of t can then be fit to an exponential decay function. An example of a T_1 measurement

of a rectmon qubit is shown in Figure 1.4.
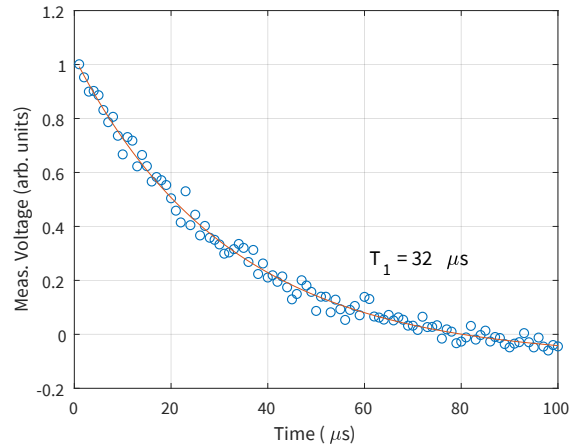
Figure 1.4: Relaxation experiment to measure T_1.

In addition to relaxation into the ground state, the qubit can also dephase. This can be thought of as noise in the qubit's frequency. Together with energy relaxation, dephasing leads to the decoherence of an arbitrary quantum state at a rate Γ_2^* given by

$$\Gamma_2^* \equiv \frac{1}{T_2^*} = \frac{1}{2T_1} + \frac{1}{T_\phi}. \tag{1.35}$$

T_2^* is measured in a Ramsey experiment by preparing the qubit in a perfect superposition state with a rotation of $\pi/2$ about the X or Y axis, with a pulse at a frequency $\omega_q + \delta$. The qubit state will precess at this detuning frequency. Some time later, an identical pulse is applied to the qubit. If the qubit did not dephase, the resulting qubit state will oscillate between $|0\rangle$ and $|1\rangle$ at frequency δ. Dephasing will result in an exponential envelop to this oscillation, eventually resulting in a random mixed state with 50% occupation probability. This exponentially damped sinusoid can then be fitted to extract T_2. An example of a Ramsey experiment is shown in Figure 1.5.

Ramsey experiments are sensitive to low frequency noise between individual experiments. This low frequency noise can be reduced with an echo experiment. A superposition state is prepared with a $\pi/2$ pulse (on resonance this time), with a following identical pulse at time t. However, this time a
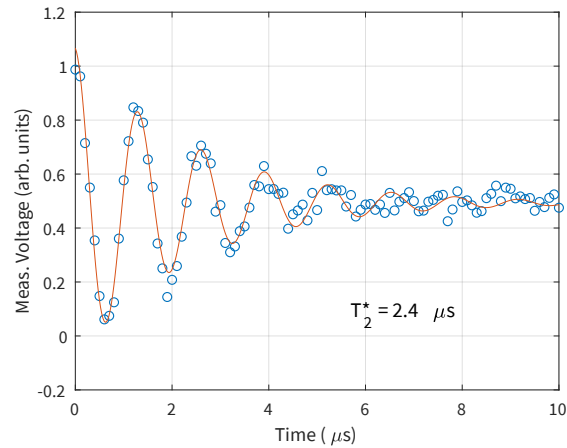
Figure 1.5: Ramsey experiment to measure T_2^*.

π pulse is performed at time $t/2$. An example of an echo experiment is shown in Figure 1.6.
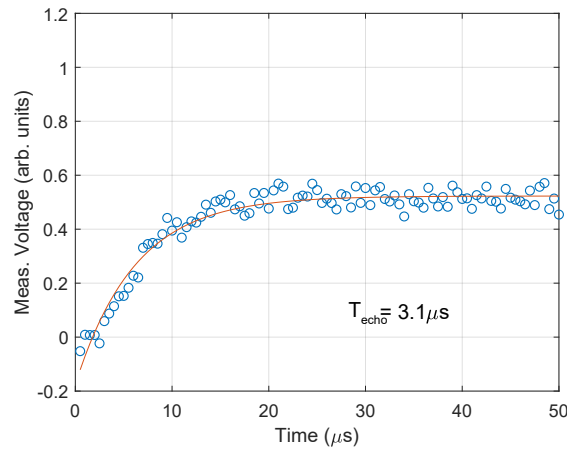
Figure 1.6: Echo experiment to measure T_{Echo}.

1.3   Single-Flux-Quantum Logic

Most of the work presented here utilizes another form of superconducting electronics; the Single-Flux-Quantum (SFQ) digital logic family. Superconducting digital circuits were explored as early as the 1950s, and advanced quickly after the development of the Josephson junction in the mid-1960s. Although a whole family of implementations exist, the common theme is the utilization of the flux quantum ($\Phi_0 = h/2e$) as the physical manifestation of information, analogous to the voltage on
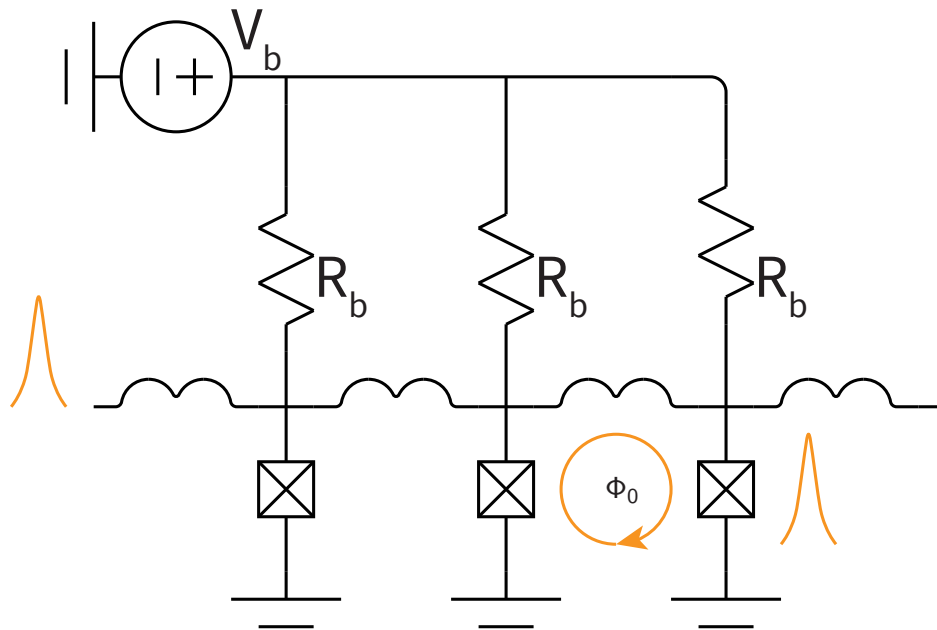
Figure 1.7: Example of an RSFQ circuit, the Josephson Transmission Line (JTL). Each junction in the line is biased by a bias current $I_b = V_b/R_b$ so as to be near its critical current. Incoming flux causes the leftmost junction to switch momentarily into its voltage state, which propogates the pulse forward. The junctions are shunted, so that they reset quickly into their superconducting state. Bias resistors dissipate heat according to V_b^2/R_b.

transistors in conventional CMOS digital logic.

RSFQ (Rapid Single-Flux-Quantum[5]) circuits were developed in the mid 1980s in the Soviet Union, and became the dominant logic family over the next several decades [27]. In RSFQ logic elements, Josephson junctions are critically damped ($\beta_C \approx 1$) with a shunt resistor, so as to switch quickly without hysteresis. This results in a very fast voltage pulse with height $\approx I_c R_n$. Since the time integral of the voltage is quantized by $\int V(t)\,dt = \Phi_0$, this results in pulse lengths on the order of a few picoseconds for traditional high-J_c niobium-based junctions. These short pulse lengths allow the circuit to be clocked at incredibly high speeds, with the highest reported RSFQ circuit operating at $\approx 770\,\text{GHz}$ [28]. It is common to think of these voltage pulses as the physical manifestation of a digital bit rather than the presence of a quantum of flux. Both pictures can be useful for various circuits.

---

[5]any references to SFQ in this work imply RSFQ

The simplest RSFQ element is the Josephson Transmission Line (JTL). The JTL is the most common element used to route SFQ pulses between logic elements. A circuit diagram is shown in Figure 1.7. The JTL consists of two critically damped junctions in a loop, biased near their critical currents $I_b \approx 0.75 I_c$. The inductance between the two junctions is chosen so that $L I_c \approx \Phi_0/2$, preventing a quantum of flux from being stored in the loop without exceeding I_c. The arrival of an SFQ voltage pulse into the input of the JTL adds to the bias current and pushes the first junction past its critical current. This causes the junction to switch into its voltage state, so that the flux (current) is forced to go through J2, exceeding its critical current and causing it to switch. The flux leaves the loop, and the junctions reset into their supercurrent state as the SFQ pulse leaves the circuit.

1.3.1   Removing static power dissipation: eRSFQ

The largest obstacle encountered when combining conventional SFQ logic with superconducting qubits is the problem of dissipation. Dissipation of power generates quasiparticles and locally heats the dissipative element. Both of these mechanisms can potentially lead to qubit decoherence. Additionally, the dilution refrigerators needed to cool qubits can only supply a certain cooling power to the lowest temperature stages. It is therefore crucial to minimize power dissipation at millikelvin temperatures.

The power dissipated by a switching junction in an RSFQ cell is given by

$$P = I_c \Phi_0 f_s, \tag{1.36}$$

where f_s is the frequency at which the junction is switching. Dissipation as a result of circuit operation (dynamic dissipation) is usually significantly smaller than the power dissipated by biasing each of the junctions through bias resistors (static dissipation). This has resulted in several new RSFQ variations that bypass this static power dissipation, either by using an AC biasing scheme that replaces
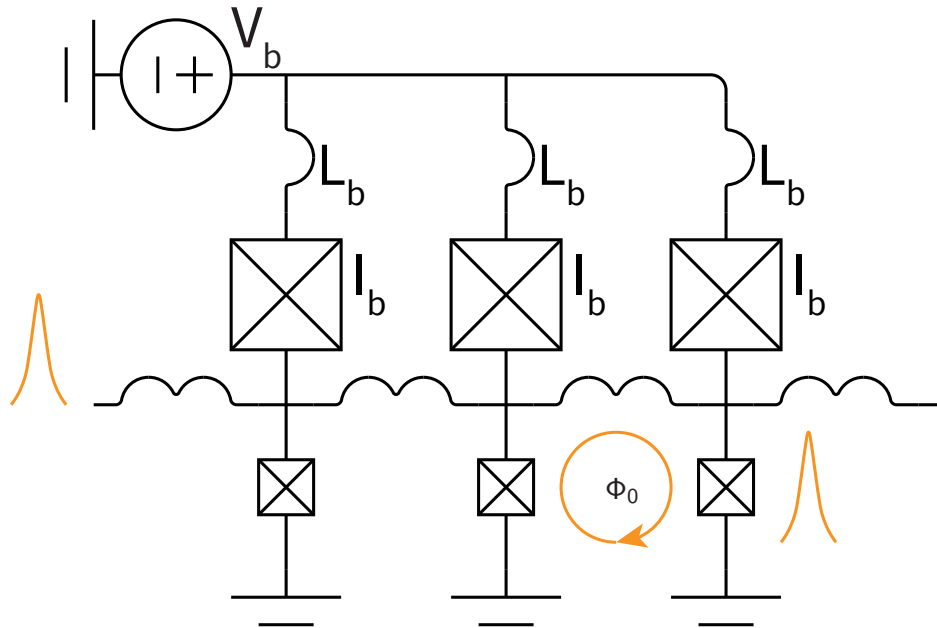
Figure 1.8: An eRSFQ version of a JTL. Here the bias resistors have been replaced with Josephson junctions that limit current to its critical current I_b, and a series inductor L_b that prevents current fluctuations from propagating back to other bias junctions.

bias resistors with transformers [29], or by replacing bias resistors with current-limiting Josephson junctions[30]. All references to SFQ logic in the following work specifically refer to the eRSFQ family of logic circuits [31], which utilizes the latter method. An eRSFQ version of a JTL is shown in Figure 1.8.

The bias junction is biased by a small voltage (much smaller than what would be needed to bias through a resistor). If the JTL junctions are not switching, the bias junction switches at a rate $f_s = V/\Phi_0$. If a flux travels through the circuit and the JTL junction switches, Jb need not switch in order to maintain the constant voltage. This limits the power dissipated by the bias junction to a value set by the operating frequency of the circuit, essentially replacing static power dissipation with the dynamic power dissipation of an additional junction [32].

RSFQ logic is a quite mature technology, with over 30 years of active development. Along with the previously mentioned $770\,\mathrm{GHz}$ circuit, notable results include an 8-bit Asynchronous Arithmetic-Logic-Unit (ALU) [33], 4-bit bit-slice ALU [34], full 8-bit processors [35], and significant results in wide-

band digital receivers [36].

Chapter 2

Control

The third Divencenzo Criteria stated in Section 1.1 is "*A universal set of quantum gates*". A more accurate and explicit version of this criteria would read "*A universal set of high-fidelity single-qubit gates, and a high-fidelity two-qubit entangling gate*". While the *high-fidelity* qualifier may seem obvious, it is the most difficult element to get right. Classical digital gates can be performed on semiconducting integrated circuits at error rates are essentially 0 for the life of the device. Quantum gates on the other hand are subject to a number of channels for infidelity, such as imperfect control signals, leakage out of the ideal computational basis state, and qubit decoherence.

This chapter is arranged as follows. First, I will give an overview of traditional techniques for performing single-qubit gates on superconducting qubits. Special attention will be paid to the fundamental challenges involved with using microwave signals to perform these gates. Then, I will introduce an alternative control method utilizing the superconducting digital logic outlined in Section 1.3. Experimental results are presented, showing high-fidelity gates are possible, and methods of improvement are discussed. More attention is given to unpublished results from an experiment controlling a qubit with a digital pattern generator. As far as the author knows, these are the first demonstrations of qubit control without utilizing a microwave generator. Finally, ongoing and future steps are discussed.

2.1 Qubit Control with Microwaves
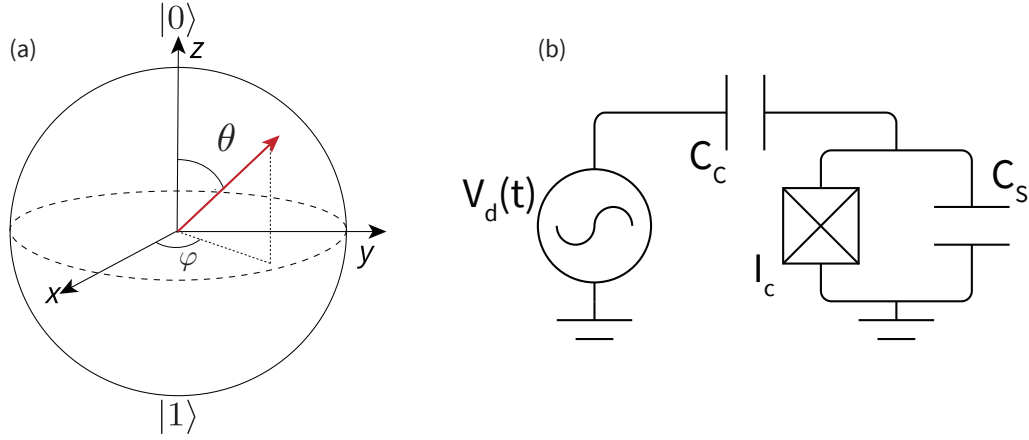
Figure 2.1: (a) The Bloch sphere, representing the state of the qubit as a vector on a unit sphere. (b) Circuit diagram for a qubit driven capacitively via an external drive voltage. These pulses rotate the qubit state about the *x* and *y* axes.

It is helpful to use the Bloch sphere to visualize the state of the qubit, as is shown in Figure 2.1a. Here, the state of the qubit is drawn as a vector within a unit sphere. The state of the qubit can be defined by the angles θ and φ, as well as the length of the vector. Controlling the qubit consists of rotating this vector about any of the 3 axes.

Rotations about the *x* and *y* axis can be achieved by capacitively coupling the qubit to a drive voltage, as shown in Figure 2.1b. The Hamiltonian for this driven circuit is just the Hamiltonian of the qubit $H_0 = \frac{-\hbar\omega_q}{2}\sigma_z$ [1] plus a drive term H_d [37]. The drive term is just the kinetic energy from the coupling capacitor C_c

$$H = H_0 + H_d \tag{2.1}$$

$$= -\frac{\hbar\omega_q}{2}\sigma_z + \Omega V_d(t)\sigma_y. \tag{2.2}$$

[1] The isolated qubit Hamiltonian is $H_0 = \frac{\hbar\omega_q}{2}(\mathbf{1} - \sigma_z)$, but the first term is a constant that can be ignored here.

Here, $\Omega = \hbar(C_c/(C_c + C_s))Q_{zpf}$ is the strength of the coupling, determined by the voltage division of the capacitor network, as well as the zero-point charge fluctuations of the qubit $Q_{zpf} = \sqrt{\hbar/2Z}$, with $Z = \sqrt{L/C_s}$ being the impedance of the circuit [38].

If we move into the qubit's reference frame (a reference frame precessing with frequency ω_q, denoted by $\tilde{H}$), the drive Hamiltonian becomes

$$\tilde{H}_d = \Omega V_d(t)(\cos(\omega_q t)\sigma_y - \sin(\omega_q t)\sigma_x). \tag{2.3}$$

If the drive voltage is a sinusoidal pulse with frequency ω_d and envelope $a(t)$, this can be rewritten as

$$\tilde{H}_d = \Omega a(t)(I\sin(\omega_d t) - Q\cos(\omega_d t))(\cos(\omega_q t)\sigma_y - \sin(\omega_q t)\sigma_x). \tag{2.4}$$

Applying the rotating-wave approximation[2] and assuming the qubit is being driven on resonance $(\omega_d = \omega_q)$,

$$\tilde{H}_d = -\frac{\Omega}{2}a(t)(I\sigma_x + Q\sigma_y). \tag{2.5}$$

We now have two independent knobs for applying rotations about the x and y axes, by adjusting the values I and Q. Here, I and Q are often known as the 'In phase' and 'Quadrature' components of the drive signal.

---

[2] Discarding high frequency terms involving $\omega_q + \omega_d$.

In practice, it is difficult to generate high-fidelity pulses within the typical frequency range of qubits. Instruments capable of directly producing shaped pulses in the several gigahertz range exist, but are prohibitively expensive. It is much more sensible to synthesize this signal by utilizing off-the-shelf microwave components. Digital-to-analog converters (DACs) with $1\,\text{GSa/s}$ sampling rates are relatively affordable and capable of producing the pulse envelope $a(t)$ in Eq. 2.5. This signal can be generated within the 10-100 MHz range, and then up-converted to the qubit frequency.

This up-conversion can be naturally done with an IQ Mixer[3]. An IQ mixer is a 4 port device that can be used as a modulator (frequency up-conversion), or a demodulator (frequency down-conversion). In the case of up-conversion, the mixer takes two intermediate frequency (IF) signals

$$I(t) = i(t)\cos\left(\omega_{IF}t\right) \tag{2.6}$$

$$Q(t) = q(t)\sin\left(\omega_{IF}t\right) \tag{2.7}$$

and a local oscillator (LO, sometimes referred to as the carrier signal)

$$LO(t) = \cos\left(\omega_{LO}t\right) \tag{2.8}$$

as input signals at I, Q, and LO ports. Internally, LO is split using a 90° Hybrid Coupler to produce two signals that are 90° out of phase ($\sin\left(\omega_{LO}t\right)$ and $\cos\left(\omega_{LO}t\right)$). Two traditional mixers multiply the LO with the IF signals, and a combiner adds these signals into an output signal at the RF port. Neglecting linear effects of the splitting, mixing, and combining processes, the RF signal can be

---

[3]`https://www.markimicrowave.com/assets/appnotes/IQ_IR_SSB_Mixer_Primer.pdf`

generally written as

$$a_{rf}(t) = i(t) \cos(\omega_{IF} t) \cos(\omega_{LO} t) + q(t) \sin(\omega_{IF} t) \sin(\omega_{LO} t). \tag{2.9}$$

Assuming that the envelope can be defined by $i(t) = -q(t) = a(t)$ (this selects an X rotation) and making use of some trig identities[4] we can perform the multiplication to get

$$a_{rf}(t) = a(t) \cos[(\omega_{IF} + \omega_{LO})t]. \tag{2.10}$$

Therefore to generate a frequency ω_q, we need to choose our frequencies so that $\omega_q = \omega_{IF} + \omega_{LO}$. This signal is filtered and attenuated by the wiring in the cryostat (mathematically represented by the frequency dependent transfer function $T(\omega)$), resulting in the drive voltage

$$V_d(t) = T(\omega) a_{rf}(t) \tag{2.11}$$

expressed in Eq. 2.3.

The IQ mixers used in traditional superconducting qubit experiments are notoriously difficult to make with the tolerances needed for high-fidelity gates. The IQ mixers primarily used by the qubit community are niche devices with a hefty price tag, and are often subject to very long lead times between fabrication runs.

---

[4]

$$\sin(a) \sin(b) = \frac{1}{2}(\cos(a - b) - \cos(a + b))$$
$$\cos(a) \cos(b) = \frac{1}{2}(\cos(a - b) + \cos(a + b))$$

Outside of financial cost and availability, there are also physical concerns when using IQ mixers. Even state of the art mixers are imperfect devices and require frequent calibrations. The diodes within the mixers have a finite voltage drop across them that may not be equal in both I and Q mixers. This voltage drop is also temperature dependent. Ideally these voltages cancel out, but in reality, these voltages are modulated by the LO to cause an unwanted signal in the RF output. This is known as 'carrier leakage'. In order to correct for this, dc offsets need to be artificially added to both I and Q signals to perfectly cancel out and eliminate the unwanted carrier signal from the output. Additionally, the 90° Hybrid Coupler is an imperfect device, deviating from a 90° offset by a phase skew of a few degrees. More annoyingly, this skew is not consistent for all LO frequencies. If the LOs to each internal mixer are not out of phase by exactly 90°, Eq. 2.9 does not nicely simplify to Eq. 2.10. Instead, higher order terms are generated that may add and produce an unwanted 'negative' sideband with a frequency of $\omega_{LO} - \omega_{IF}$ to go along with the intentional sideband frequency $\omega_{LO} + \omega_{IF}$. To correct this, the phase difference of the I and Q signals must be calibrated so as to minimize this unwanted sideband.

This set of calibration procedures for an IQ mixer must be performed every time the desired RF frequency is changed, and also regularly in time to account for the temperature drift of the ambient environment. These frequent calibrations reduce the useful duty cycle of a quantum processor.

To avoid using IQ modulation entirely, researchers have used Software Defined Radios (SDRs)[39] and Direct-Digital-Synthesis (DDS) of qubit control and readout pulses[40]. While DDS is promising and likely the next step in microwave qubit control, the cost per qubit is still prohibitively expensive. More importantly, the fundamental problem of requiring an rf line from room temperature to millikelvin is not addressed.
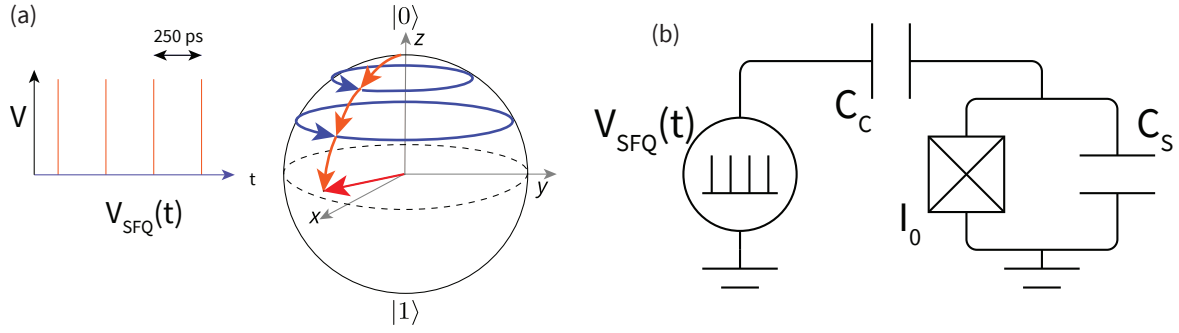
Figure 2.2: (a) SFQ Waveform to drive rotations about the Bloch sphere. Assuming the qubit has a frequency $\omega_q = 2\pi 4\,\text{GHz}$, the SFQ pulses are spaced 250 ns apart, allowing the qubit state to precess one full period about the sphere. (b) Circuit model of an SFQ driver capacitively coupled to a transmon qubit.

2.2 Qubit Control with SFQ pulses

It is attractive to consider SFQ technology as an alternative to microwave signals for qubit control. Here we consider the effect of irradiating a qubit with a train of SFQ voltage pulses in order to perform single-qubit operations [41].

We will keep the same circuit of a control voltage capacitively coupled to a qubit, but with a drive voltage consisting of a pattern of SFQ voltage pulses, rather than a sinusoidal signal. Rewriting the the drive term from Equation 2.3 in terms of the qubit frequency rather than the impedance, we see

$$H_d(t) = \Omega V_d(t)\sigma_y \tag{2.12}$$

$$= C_c V_d(t)\sqrt{\frac{\hbar\omega_q}{2C'}}\sigma_y, \tag{2.13}$$

where $C' = C_s + C_c$. Writing out the full operator,

$$U_d = \exp\left(-\frac{i}{\hbar}\int H_d(t)\,\mathrm{d}t\right) \tag{2.14}$$

$$= \exp\left(-iC_c\sqrt{\frac{\omega_q}{2\hbar C'}}\int V_d(t)\,\mathrm{d}t\,\sigma_y\right) \tag{2.15}$$

$$= \exp\left(-i\,\delta\theta\,\sigma_y/2\right), \tag{2.16}$$

which is just the general rotation operator, rotating the state about the y axis by some angle $\delta\theta$. To calculate this angle we must perform the integral. For a single SFQ voltage pulse, the integral of the voltage is constrained to be a flux quantum, such that

$$\int V(t)\,\mathrm{d}t = \Phi_0. \tag{2.17}$$

This leads to the rotation from a single SFQ pulse to be

$$\delta\theta = C_c\Phi_0\sqrt{\frac{2\omega_0}{\hbar C'}}, \tag{2.18}$$

which is only a function of fixed capacitances and the frequency of the qubit. This is incredibly useful, as there is no longer a channel for drift or noise from room temperature electronics to directly modify the control pulse. If the qubit is a fixed frequency qubit, then all of the terms in Eq. 2.18 should only depend on parameters that are fixed at the time of fabrication and are not sensitive to any drift or noise from room temperature electronics.

Since every SFQ pulse is identical, we cannot calibrate a specific rotation from a single pulse. Rather than adjusting the amplitude and phase of an arbitrary voltage drive, rotations are calibrated by applying multiple pulses and taking advantage of the free precession of the qubit. For example, to perform a π pulse about the y axis, we perform $N = \pi/\delta\theta$ pulses separated by a time $T = n2\pi/\omega_q$

$$V_N(t) = \Phi_0[\delta(t) + \delta(t - T) + \cdots + \delta(t - (N - 1)T)]. \tag{2.19}$$

The energy deposited into the qubit by this pulse is therefore given by

$$E_n = \frac{\omega_0^2 C_c^2 \Phi_0^2}{2C'} \frac{\sin^2(n\omega_0 T/2)}{\sin^2(\omega_0 T/2)}. \tag{2.20}$$

This simple pulse pattern has been named a DANTE pulse (Delays Alternating with Nutations for Tailored Excitation).

2.2.1 Experiment

In collaboration with Robert McDermott's group at the University of Wisconsin-Madison, devices were fabricated in order to perform SFQ based qubit control. To generate SFQ pulses, a DC-SFQ converter (afterwards referred to as the SFQ driver) was fabricated on a qubit device. A DC-SFQ converter is a fundamental SFQ logic element, converting rising edges from an analog input signal into a single SFQ pulse[5]. The converter requires a single dc current bias for operation, and this biasing was performed with traditional resistive biasing.

While the SFQ circuit is relatively simple, fabricating it is quite complicated and required many months of development from the collaborators at UWM. Fabricating high-quality cavities and qubits on the same substrate as an SFQ circuit required many additional fabrication steps. Crucially, the ground plane that the readout resonator and qubit capacitor were fabricated in was protected with SiOx during the SFQ junction fabrication. After the SFQ junction layers are deposited, this protective SiOx area is etched, and the resonator and qubit was patterned and etched into the ground plane. As a last step, the qubit junctions were patterned, oxidized, and lifted off as described in Appendix 1.

---

[5] http://www.physics.sunysb.edu/Physics/RSFQ/Lib/AR/dcsfq.html
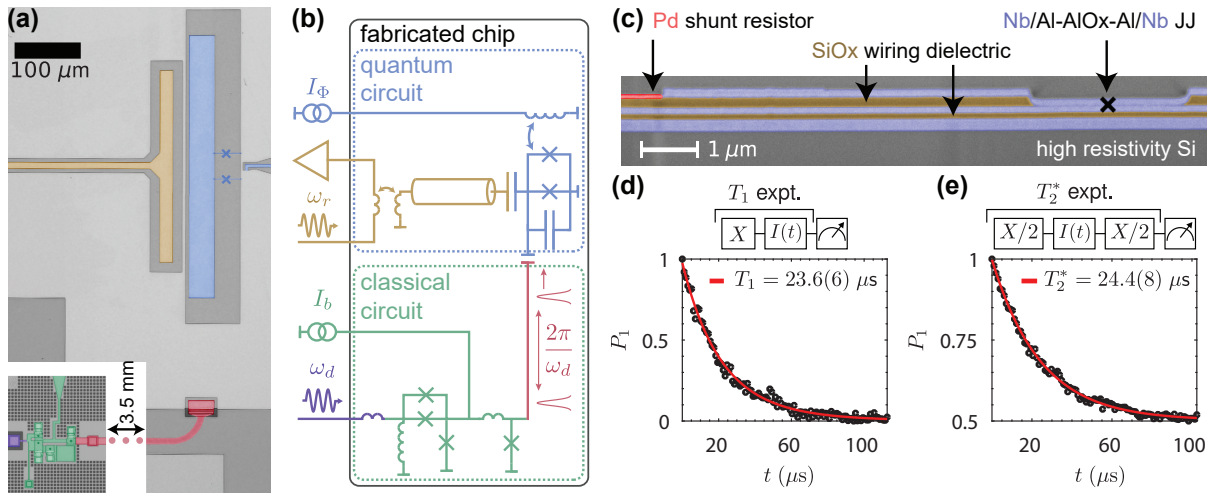
Figure 2.3: (a) False color image of the SFQ Driver and bias line (green), trigger line (purple), coupling capacitor (red), qubit (blue), and readout resonator (yellow). (b) Circuit diagram. (c) Cross section of an SFQ junction, with metal, dielectric, and resistor layers shown. (d) Coherence times of a qubit controlled with SFQ driver. Used with permission from Ref. [42]

In these initial experiments, the SFQ driver was triggered with a microwave pulse constructed as described in Section 2.1. This allowed for arbitrary timing control of the SFQ pulses. Both the power level of the microwave trigger and the dc bias level of the driver was calibrated by performing an IV measurement of the driver bias line while applying a continuous wave microwave signal. When the converter is biased with the appropriate current, and the trigger signal has the appropriate power level, the generated SFQ voltage pulses average to a value given by

$$\langle V \rangle = n\Phi_0 f, \tag{2.21}$$

where f is the frequency of the output pulses, and n is an integer determined by the number of pulses generated per rising edge ($n = 1$ for all experiments discussed here). This voltage step on the IV curve due to an applied rf signal is known as a Shapiro step[43]. This voltage was measured across the bias line itself, by adding a voltage tap using a resistor tee at $3\,\text{K}$.

The device was cooled in a dilution refrigerator to below $10\,\text{mK}$. Traditional microwave techniques
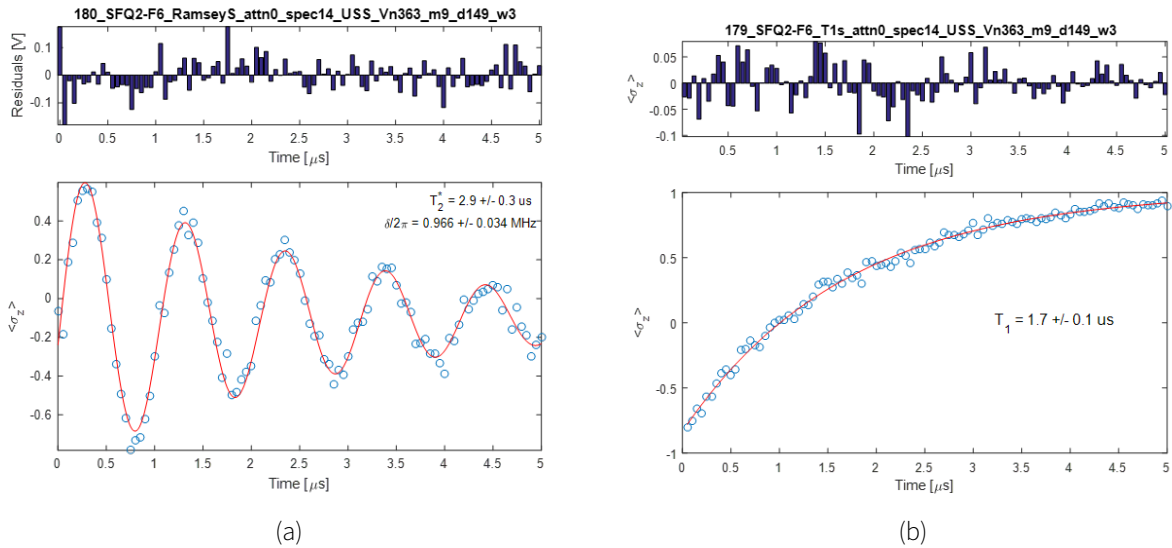
Figure 2.4: (a) Ramsey and (b) T_1 experiment performed with SFQ control instead of microwaves.

were used to characterize the qubit separately from the operation of the SFQ driver. Results from the device with the highest coherence times has been previously reported [10]. Key results are an average single-qubit gate fidelity of 95%, measured with randomized benchmarking [44]. Results from a qubit measured at Syracuse with much lower coherence time is shown in Figure 2.4.

2.2.2   Qubit Control with Bit Pattern Generator

Once the SFQ Driver had been characterized with microwave triggers, alternative triggering methods were considered. Since the DC-SFQ converter should trigger on rising edges of a given current, triggering is not constrained to sinusoidal signals. In an effort to remove microwave signals completely from the qubit control chain, an alternative instrument was needed. The Tektronix PPG-4001 (afterwards referred to as the PPG) was loaned to our group from Tektronix, in order to determine its usefulness for this purpose. The PPG is an instrument primarily used to test Gigabit Ethernet systems and test digital receivers at very high speeds. It can produce rising or falling edges at a rate of 40 Gb/s.

While the PPG worked as advertised, several issues made it very difficult to incorporate into our
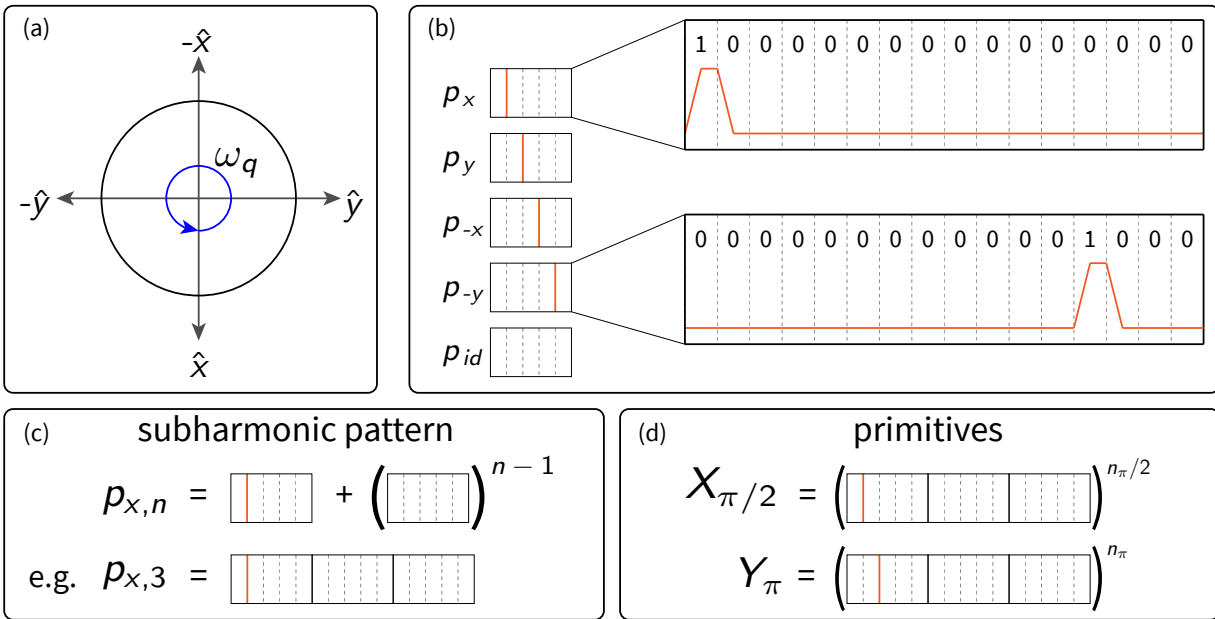
Figure 2.5: (a) XY plane of the Bloch sphere, illustrating the 4 different rotation directions. (b) Digital patterns to rotate the qubit about the 4 axes, and the identity pattern. (c) When driving at a subharmonic, additional identity patterns are added, allowing the qubit to precess another period. (d) Constructing pulse primitives out of patterns. For example, constructing a $X_{\pi/2}$ pulse consists of creating the appropriate p_x subharmonic pattern, and then repeating it $n_\pi/2$ times, where n_π is the number of pulses needed for a π pulse.

measurement system. The first of which is that it is a pattern generator, not a pulse generator. The signal is not encoded as pulses, but rather a bit change from $0 \rightarrow 1$ ($1 \rightarrow 0$) is encoded as a rising (falling) edge. For example, requesting a pattern of '1111' results in a 'high' level being held for 4 clock cycles rather than four rising edges. To produce a train of 4 pulses, 8 bits ('10101010') were needed. This basically divided the useful clock frequency in half. However, even this 8-bit pattern is not useful. For most of our experiments, the qubit frequency was 4 GHz. Naively setting the PPG to 8 GHz essentially produces a square wave, which is spectrally similar to a sinusoidal microwave signal. Instead, a higher multiple of the qubit frequency had to be chosen as a clock rate. For example, at 16 GHz, the sequence '1000100010001000' produced a train of fast, sharp edges at the qubit frequency of 4 GHz.

This is further complicated when phase control is taken into account. When driving the qubit with microwaves, standard IQ modulation allows the control signal to have an arbitrary phase. With the
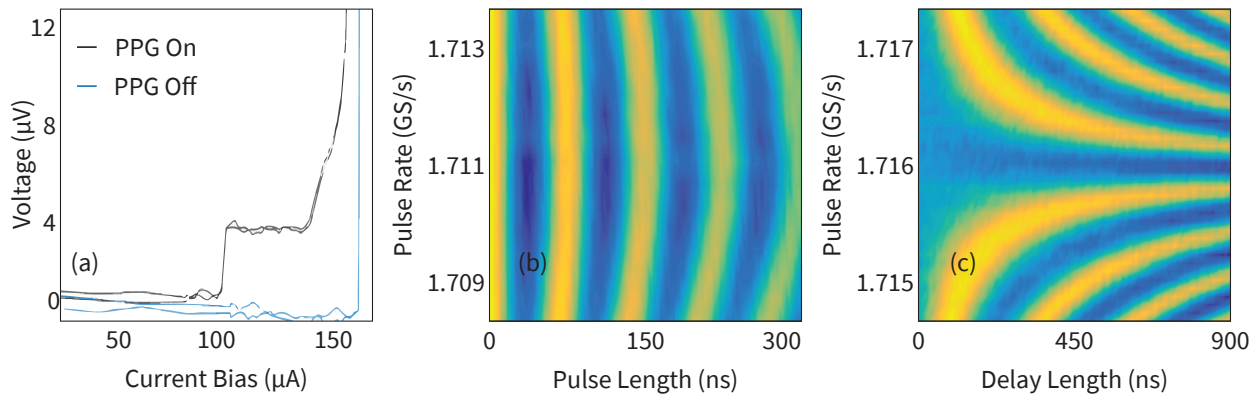
Figure 2.6: Qubit Control with PPG Pattern Generator. (a) Shapiro steps, showing optimal biasing of SFQ driver. (b) Rabi Oscillations. (c) Ramsey Experiment. Frequency offset is due to qubit decay dephasing during drive. Pulses applied at third subharmonic $f_q/3$, PPG sampling rate $5f_q/3$.

PPG, only discrete phases can be achieved by shifting the pattern by a single bit at a time. In order to have 4 directions of rotation ($\pm X, \pm Y$), the clock rate must be some multiple of 4 times the qubit frequency. This is illustrated in Figure 2.5.

The optimal DC bias point for the DC-SFQ converter was found by measuring a Shapiro step in the same way as was previously done with microwaves. This is shown in Fig. 2.6. Once the converter was properly biased, all of the standard qubit measurements could be performed. Rabi and Ramsey measurements are shown in Figure 2.6.

An effort was also made to test gate fidelity with the PPG by using Randomized Benchmarking [45], however the low coherence times of the qubit combined with the long pulse lengths needed made this very difficult. Instead, a very rudimentary test of applying each of the Clifford gates and their inverses was performed in order to check for a bound on gate fidelity and compare various Clifford gates. Results are shown in Figure 2.7. While SPAM errors are not accounted for, a clear dependence on pulse length can be seen, with longer pulses having considerably lower 'fidelity'.

Unfortunately, we were only able to play with the PPG for 2-3 weeks. Further experiments with qubits with longer coherence times would be very interesting. The device was clearly not developed with quantum computing in mind, however it helped demonstrate that the SFQ control scheme is
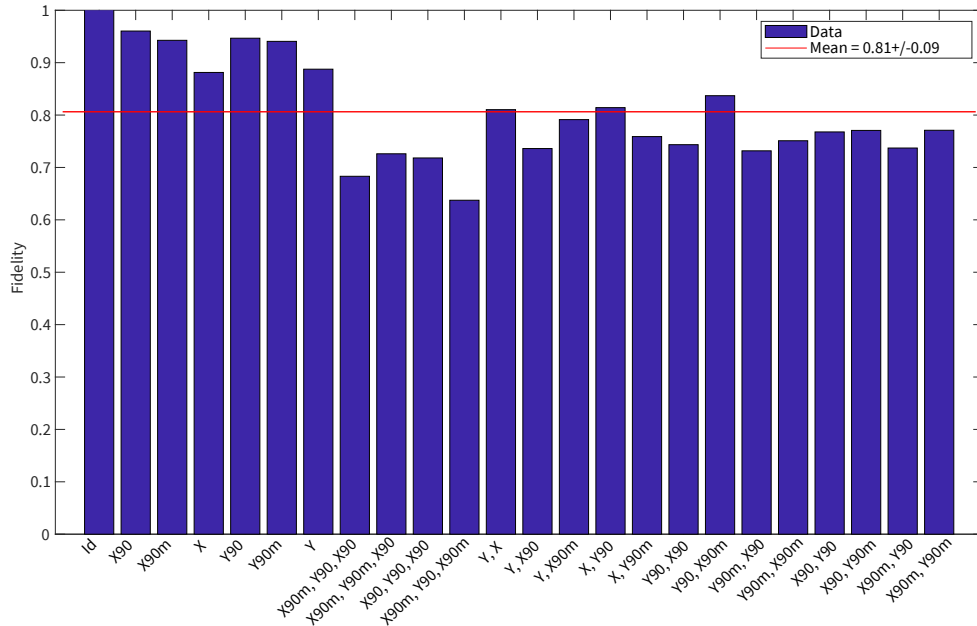
Figure 2.7: CC^{-1} for each Clifford gate, triggered with the PPG. Longer gates have lower fidelities, pointing to decoherence as a limiting factor.

fundamentally a digital process, and does not require microwave signal processing.

2.3   Multi-chip Module

The results mentioned in Section 2.2.1 were limited by quasiparticle poisining generated by the operation of the SFQ driver [10]. In an effort to both mitigate quasiparticle poisoning due to the SFQ circuitry, and to avoid the complexities of fabricated SFQ circuits and high-coherence qubits on the same device, a multi-chip module (MCM) approach has been developed. An MCM device is an IC consisting of multiple chips that have been physically and/or electrically bonded in some way. MCMs are frequently leveraged in traditional digital electronics. A popular method involves using a soft metal such as indium to form bumps of solder in an array on one of the chips. The chips are then aligned face to face, and brought into contact with an appropriate heat and pressure so as to reflow the solder and bond the two devices together. Since indium is supercondcting, bump bonding with indium bumps is a natural method for developing a superconducting MCM, and has become an active path of development in the field. An overview of various 3D packaging techniques
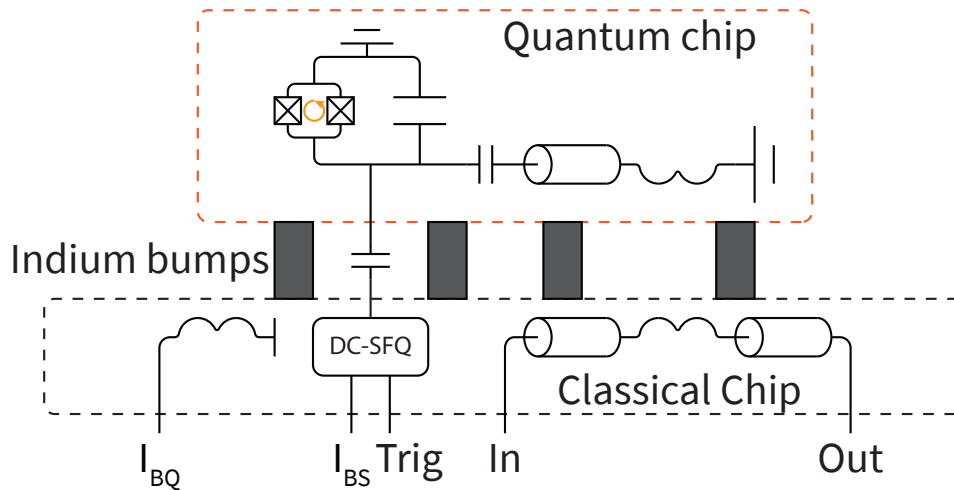
Figure 2.8: Diagram of MCM device. A top chip contains the qubit and readout resonator. The bottom chip contains the SFQ circuitry, as well as current bias lines for the qubit and a feedline to couple to the resonator. Superconducting indium bumps connect the ground planes of the two chips.

for quantum devices can be found here [46].

In collaboration with SeeQC, an MCM carrier chip was fabricated, to be bonded to qubit chips fabricated at Syracuse. A simple circuit schematic is shown in Figure 2.8. A tunable qubit and its readout resonator are fabricated on a top chip. A DC-SFQ converter, microwave feedline, and qubit flux-bias line are fabricated on the bottom chip. Initial results with these devices are promising, although
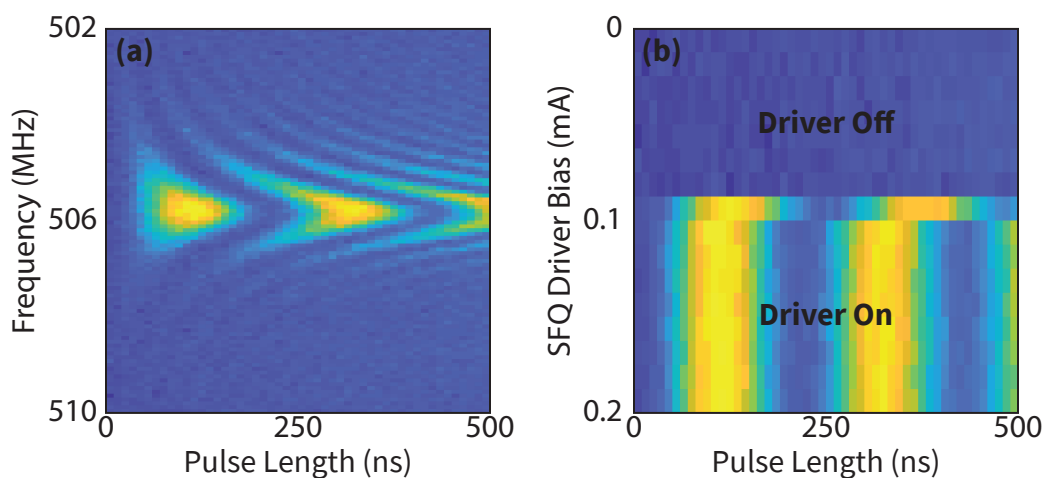
Figure 2.9: Results with an MCM device. (a) Rabi oscillations at $f_q/8$. (b) Rabi Oscillations versus SFQ driver bias. The point where the driver starts emitting pulses is very clear.

coherence times have been very short in preliminary devices. It is unclear as of yet whether this low coherence time is a result of poor qubit fabrication, the carrier chip, or somehow a result of the MCM environment itself. However, basic qubit measurements can still be performed. Rabi oscillations, and Rabi oscillations versus driver bias are shown in Figure 2.4.

2.4   Future work

The future of digital qubit control is very promising, with problems to be solved in both theoretical and experimental areas. The obvious omission from this chapter has been the discussion of two-qubit gates. As of this writing, there has not been a theoretical model proposed for performing entangling gates similar to the single-qubit gates used in this chapter. Naively, one can imagine taking any number of the standard entangling gates and adapting them for use with SFQ circuits.

Another interesting idea involves triggering SFQ pulses at a clock rate significantly higher than the frequency of the qubit, and using highly non-intuitive patterns that are calibrated to maximize fidelity by minimizing leakage into higher energy states. Initial theoretical investigations are very promising, suggesting that 1×10^{-3} error rates are achievable in under $10\,\mathrm{ns}$ by calibrating optimal pulses clocked at frequencies around 10 times that of the qubit [47]. Cryogenic control also encourages the use of a cryogenic memory in order to store pulse patterns within the cryostat, and fully eliminate the need to supply control signals from room temperature in real-time. Simulations have also been performed to find pattern primitives that can be recycled and used for multiple qubits at different frequencies in an effort to minimize the needed memory [48]. Both of these ideas encourage the notion that optimal digital control may look very different from optimal analog control, and that the highest fidelity solution may not end up being an intuitive, pre-determined solution.

Chapter 3

Measurement

Fast and accurate measurement of qubits is one of the criteria for having a functional quantum computer. High-fidelity gates and long-lived qubits are not useful in a quantum algorithm if the final state cannot be measured accurately. Critically, for error-correcting codes to be useful, qubits and their errors must be measured at a timescale that is short compared to the coherence time of the qubits.

In this chapter, I will describe the standard microwave techniques used to measure superconducting transmon qubits, and discuss the challenges involved with scaling this technique. Then I will describe an alternative method for readout, utilizing a device known as a Josephson Photomultiplier, or JPM. Experimental results from JPM-based qubit measurements are shown.

3.1   Qubit Readout with Microwaves

For well over a decade, standard microwave techniques have been used for qubit readout. When a qubit is coupled to a readout resonator in a typical cQED scheme, the system can be described by the Jaynes-Cummings Hamiltonian [49]. The Jaynes-Cummings model is standard in quantum optics, describing a system consisting of a two-level atom in an optical cavity [50]. The Hamiltonian (in the absence of decay channels) is split simply into a harmonic oscillator term for the resonator,

a term for the qubit, and an interaction term.

$$H = H_r + H_q + H_{int}$$

$$H = \hbar\omega_r \left(a^\dagger a + \frac{1}{2} \right) + \frac{\hbar\omega_q}{2}\sigma_z + \hbar g(\sigma_+ a + \sigma_- a^\dagger). \tag{3.1}$$

Here, H_r is the standard harmonic oscillator Hamiltonian containing lowering and raising operators a and $a^\dagger$. In the context of an electrical resonator with inductance L_r, capacitance C_r, these operators have the following form

$$a^\dagger = \frac{(L_r C_r)^{1/4}}{\sqrt{2\hbar}} \left(\frac{\phi}{\sqrt{L_r}} + i\frac{q}{\sqrt{C_r}} \right) \tag{3.2}$$

$$a = \frac{(L_r C_r)^{1/4}}{\sqrt{2\hbar}} \left(\frac{\phi}{\sqrt{L_r}} - i\frac{q}{\sqrt{C_r}} \right), \tag{3.3}$$

where ϕ and q are flux and charge operators [21], and σ_+ and σ_- are the Pauli raising and lowering operators for the two-level qubit system

$$\sigma_+ = \sigma_x + i\sigma_y \tag{3.4}$$

$$\sigma_- = \sigma_x - i\sigma_y. \tag{3.5}$$

The relationship between the coupling strength g, and the detuning between the resonator and qubit frequencies $\Delta = \omega_q - \omega_r$ defines two regimes. When $|g/\Delta| \gg 1$, the system is in a resonant strong coupling regime. Here, the system behaves as a hybrid system, with excitations coherently swapped between the two resonant systems. When $|g/\Delta| \ll 1$, the system is in the dispersive

regime, where the effect of the interaction term is to shift the resonances ω_r and ω_q by an amount dependent on the number of excitations. This can be seen by treating g as a perturbation and expanding to second order. The terms can be grouped in two ways that illustrate this shift. Defining $\chi = g^2/\Delta$,

$$
\begin{aligned}
H/\hbar &\approx (\omega_r + \chi\sigma_z)\left(a^\dagger a + \frac{1}{2}\right) + \frac{\omega_q}{2}\sigma_z \\
&\approx \omega_r\left(a^\dagger a + \frac{1}{2}\right) + \frac{1}{2}\left(\omega_q + \chi + 2\chi a^\dagger a\right)\sigma_z.
\end{aligned}
\tag{3.6}
$$

The first equation illustrates the dispersive shift of the resonator frequency based on the state of the qubit. The second equation illustrates the Lamb shift[1], and the Stark shift of the qubit frequency, which is linearly dependent on the number of photons in the resonator.

Equation 3.6 assumes the qubit is a perfect two-level system. Unfortunately, superconducting qubits, and especially transmons, have higher levels that play an active role in the resonator-qubit dynamics. The anharmonicity $\alpha = \omega_{12} - \omega_{01}$ (which is negative for a transmon), modifies Equation 3.6 by an adjustment to χ

$$
\chi \rightarrow \chi_{01} - \frac{1}{2}\chi_{12} = \frac{\chi}{1 - \Delta/\alpha}.
\tag{3.7}
$$

Example parameters for a typical transmon cQED device are $g/2\pi \approx 50 - 100\,\mathrm{MHz}$, $\Delta/2\pi \approx 1 - 2\,\mathrm{GHz}$, and $\alpha/2\pi = 200 - 300\,\mathrm{MHz}$.

---

[1] the χ term in the coefficient. This is due to the ever-present half-photon of vacuum fluctuations in the cavity.

3.1.1   Heterodyne Detection

The dispersive regime reveals a method for indirectly measuring a qubit state by measuring the χ-shift imparted on the resonator. Measuring this state-dependent cavity shift is typically performed with a heterodyne detection scheme. Heterodyne detection leverages IQ-modulation in a similar fashion to that used to generate qubit control pulses (Section 2.1). A readout pulse can be constructed from two IF signals and a local oscillator according to Equation 2.10. Here we determine a LO frequency so that $\omega_{RO} = \omega_{IF} + \omega_{LO}$.

High-frequency digital-to-analog converters (DACs) produce an intermediate-frequency (IF) signal with an envelope $a(t)$, which is typically a constant rectangular envelope with a rise and fall time within the IF bandwidth of the mixer. Neglecting attenuation, the measurement input signal $a_{in}(t)$ and the measurement output signal $a_{out}(t)$ can be represented as

$$a_{in}(t) = a(t)\cos(\omega_{RO}t) \qquad \text{(input)} \qquad (3.8)$$

$$a_{out}(t) = a'(t)\cos(\omega_{RO}t + \theta'). \qquad \text{(output)} \qquad (3.9)$$

Performing a measurement consists of measuring changes to the values a' and θ' as the qubit is manipulated. The signal that leaves the cryostat is demodulated with either another IQ mixer or a standard double-balanced mixer. A stable local oscillator (LO) can be split and fed into both modulating and demodulating mixers. Assuming a standard mixer is used to demodulate, the downconverted signal is

$$s'_{IF}(t) = \frac{a'(t)}{2}\left\{\cos\left[(\omega_{RF} - \omega_{LO})t + \theta'\right] + \cos\left[(\omega_{RF} + \omega_{LO})t + \theta'\right]\right\}. \qquad (3.10)$$

After low-pass filtering to remove the high frequency term, we are left with a single term at the same frequency as the original IF probe signal. This signal is acquired by a high speed digitizer, which digitizes the analog signal

$$s'[t] = \frac{a'(t)}{2} \cos\left(\omega_{IF} t + \theta'\right).$$

(3.11)

This signal is then multiplied in software[2] by a complex demodulation signal $\exp\left(i\omega_{IF} t\right)$. This digitally demodulated signal is filtered again to bring the signal down to a dc level. Performing the multiplication and filtering out high frequency terms,

$$
\begin{aligned}
d'_{DEMOD}[t] &= \frac{a'(t)}{2} \cos\left(\omega_{IF} t + \theta'\right) \times \exp\left(i\omega_{IF} t\right) \\
&= \frac{a'(t)}{2} \cos\left(\omega_{IF} t\right) \cos\left(\omega_{IF} t + \theta'\right) + i \sin\left(\omega_{IF} t\right) \cos\left(\omega_{IF} t + \theta'\right)) \\
&= \frac{a'(t)}{4} \left(\cos\theta' + i \sin\theta'\right).
\end{aligned}
$$

(3.12)

This complex dc signal is then integrated over some portion delimited by $[j, k]$, so as to only average the steady-state amplitude of the signal and ignore any transients. Ignoring constant scaling factors that result from the demodulation process, the real and complex values are represented by

---

[2]or within the FPGA onboard the digitizer, to reduce latency [51]

$$I = \sum_{i=j}^{k} a'(t) \cos \theta' \tag{3.13}$$

$$Q = \sum_{i=j}^{k} a'(t) \sin \theta'. \tag{3.14}$$

This results in the values plotted in complex space in Figure 3.1b.

In practice there are many physical elements between the room temperature mixers and the read-out resonator. On the input side, the room temperature signal must be attenuated down by many orders of magnitude in order to bring the absolute power level down to an appropriate level, and also to bring down the effective temperature of the signal. The Johnson noise power from the resistance of an attenuator with value A at a temperature T_{att} stage is proportional to an effective temperature T_{out} [3] given by

$$T_{out} = T_{att} + T_{in} 10^{-A/10}. \tag{3.15}$$

For example, the 300 K noise from the room temperature circuitry is reduced to 200 K by a 3 dB attenuator at 50 K. Additional attenuation at 10 dB at 4 K, 6 dB at 1 K, and 30 dB at 10 mK brings the 300 K noise down to 17 mK, a temperature similar to that of the qubit itself. Since the purpose of these attenuators is to dump a portion of the incoming signal to ground, they are also a source of heat deposited in the cryostat.

Additionally, many levels of filtering are needed to filter out high frequency noise. While qubits and readout resonators are typically within the 4-8 GHz range, the coaxial lines and connectors typically have bandwidth many times higher than that. This allows for black-body radiation from higher

---

[3]It should be noted that this is purely a classical analysis. For an assessment including quantum effects, see [52].
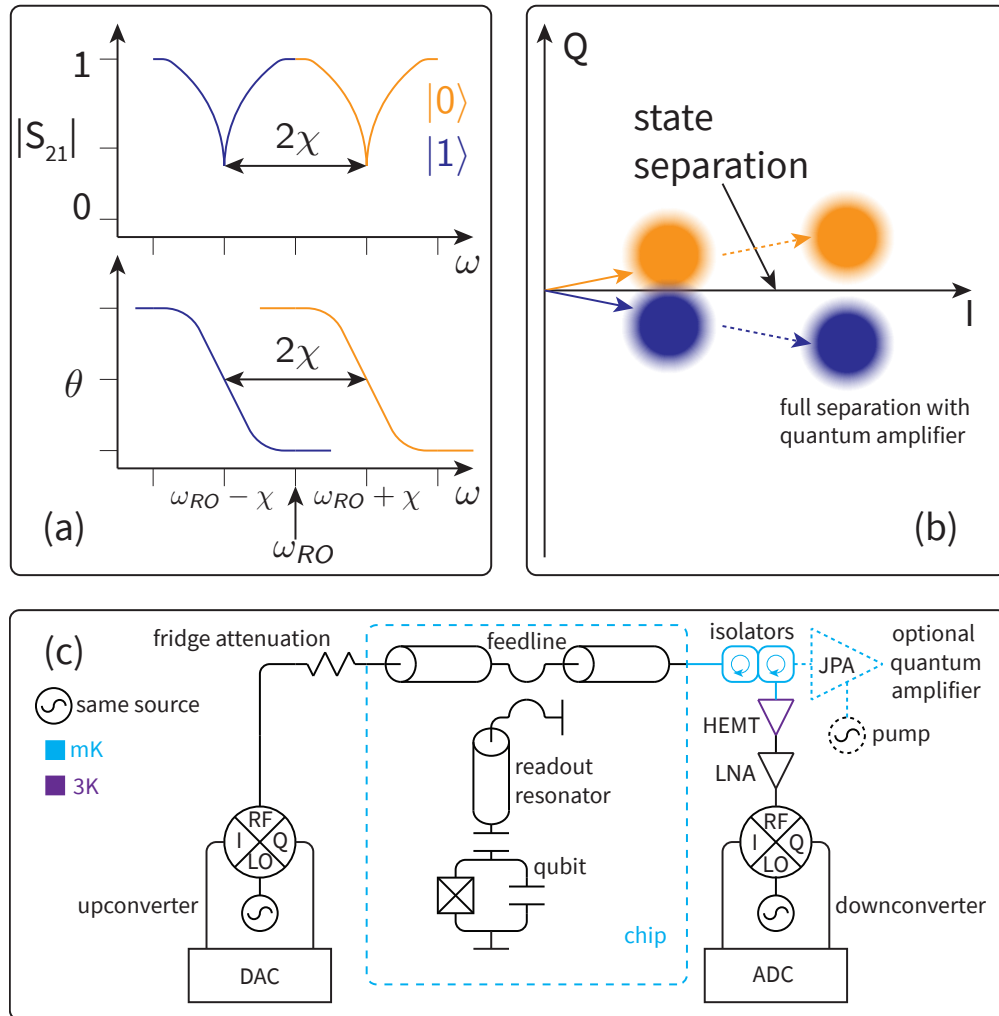
Figure 3.1: Overview of heterodyne detection. (a) Transmission of the two state-dependent resonance dips of the readout resonator. Driving between the two peaks gives the greatest contrast in phase. (b) Demodulated signal plotted in complex plane. A line can be formed to separate the two clusters of points corresponding to the two qubit states. With only a High Electron Mobility Transistor amplifier (HEMT), these clusters have some overlap, leading to measurement infidelity and requiring averaging to reduce the noise of the signal (radius of the cluster). With a quantum-limited amplifier, full separation can be achieved, allowing for single-shot measurement. (c) Example wiring diagram for heterodyne detection. A readout pulse is generated in a DAC and mixed up to the readout frequency. The heavily attenuated signal passes through a feedline coupled to the readout resonator. Circulators are used on the output line to mitigate backaction from the subsequent amplification stages. Optionally, a quantum-limited amplifier is used to pre-amplify the signal at the base temperature. This amplifier usually requires at least one microwave pump tone and additional circulators. A HEMT amplifier at $3\,\mathrm{K}$ provides enough gain for the signal to reach room temperature, where it is downconverted, usually with a split signal from the same LO that provided the upconversion. A high-speed digitizer acquires the downconverted signal, and the IQ data is calculated in software.

temperature stages to broadcast infrared noise into the quantum device. Since the superconducting gap of both niobium and aluminum fall in this frequency range ($737\,\text{GHz}$ for Nb and $82\,\text{GHz}$ for Al), this radiation can break Cooper pairs and generate quasiparticles within the superconducting film. These quasiparticles are a loss mechanism, and can dominate the loss in qubit systems. For a linear resonator, a quasiparticle density n_{qp} results in a quality factor of

$$\frac{1}{Q_{qp}} = \sqrt{\frac{2\Delta(T)}{hf_r}} \frac{\alpha n_{qp}}{\pi D(E_F)\Delta(T)} \tag{3.16}$$

in a resonator of frequency f_r, where α is the kinetic inductance fraction[4], Δ is the superconducting gap, and $D(E_F)$ is the two-spin density of states [53, 54]. Light-tight sample spaces, black coating of shielding cans, and low-pass filtering of all lines to the sample are all needed to beat down this infrared radiation so that it is no longer the leading loss channel.

After the readout signal leaves the sample, a significant amount of amplification is needed to bring the signal to room temperature. A High Electron Mobility Transistor amplifier (HEMT) is used as the main cryogenic amplifier, and is usually positioned at the $3\text{-}4\,\text{K}$ temperature stage. These are the only commercially available low-noise amplifiers with an acceptable gain and noise figure. However, even the noise from these amplifiers is detrimental to quantum circuits if several isolators or circulators are not placed between the sample and the amplifier. These non-reciprocal elements are based on magnetic materials to provide directionality that prevents transmission from the amplifiers back towards the qubit sample. Conventional microwave circulators are large and difficult to thermalize. Due to their magnetism they must also be shielded and physically separated from qubits within the cryostat.

Single-shot readout fidelity in the dispersive regime is not achievable with only a HEMT amplifier. Higher power measurement techniques exist that can result in single-shot fidelities of around 85-

---

[4]Fraction of the kinetic inductance to the total inductance, or $\alpha = L_k/(L_k + L_m)$ where L_m is the magnetic inductance

90 % [55], however these 'bright state' measurements are much more disruptive and are generally not QND. If higher single-shot readout fidelity is desired, an additional quantum-limited amplifier is needed before the HEMT. As the name implies, these amplifiers ideally only add noise at the quantum limit (a half photon), while providing modest gain (usually 10-15 dB). A wide variety of these quantum-limited amplifiers exist, notably the Josephson Parametric Amplifier (JPA) [56] and its many offspring, including the Josephson Parametric Converter (JPC) [57]. However, the limited bandwidth and saturation amplitude make it difficult to perform simultaneous readout of multiple resonators through frequency multiplexing, as is often desired.

For a multiplexed circuit, where multiple resonators are coupled to a single feedline, wider bandwidth is needed. The Traveling Wave Amplifier (TWPA) [58] and its variants utilizing kinetic inductance [59] introduce a bandwidth large enough to measure on order 10 resonators at a time [60]. Most of these amplifiers leverage Josephson junctions as a nonlinear element, and all of them require a strong pump tone of some sort, which results in the need for additional isolators.

As an example, the recent 'Quantum Supremacy' breakthrough by Google [6] utilized an IMpedance-transformed Parametric Amplifier (IMPA) [61]. Readout resonators were coupled to common feedlines (9 feedlines coupled to 6 resonators each), with each feedline requiring a separate amplification chain. Each amplification chain utilized 5 cryogenic microwave circulators, resulting in 45 total circulators needed for a 54 qubit device. This dependence on non-reciprocal elements makes it infeasible to imagine this particular measurement circuit scaling up even a single order of magnitude, as the thermal mass of hundreds of circulators alone would be impractical to cool on even the most powerful dilution refrigerators available.

It is therefore highly attractive to consider readout techniques that do not require the non-reciprocal elements needed by standard amplification techniques. It is also useful to have access to the measurement result at the millikelvin temperature stage, as error-correcting codes that require fast feedback can leverage the reduced latency. Both of these problems are solved by utilizing a Josephson Photomultiplier.

3.2   Qubit Measurement with a Josephson Photomultiplier
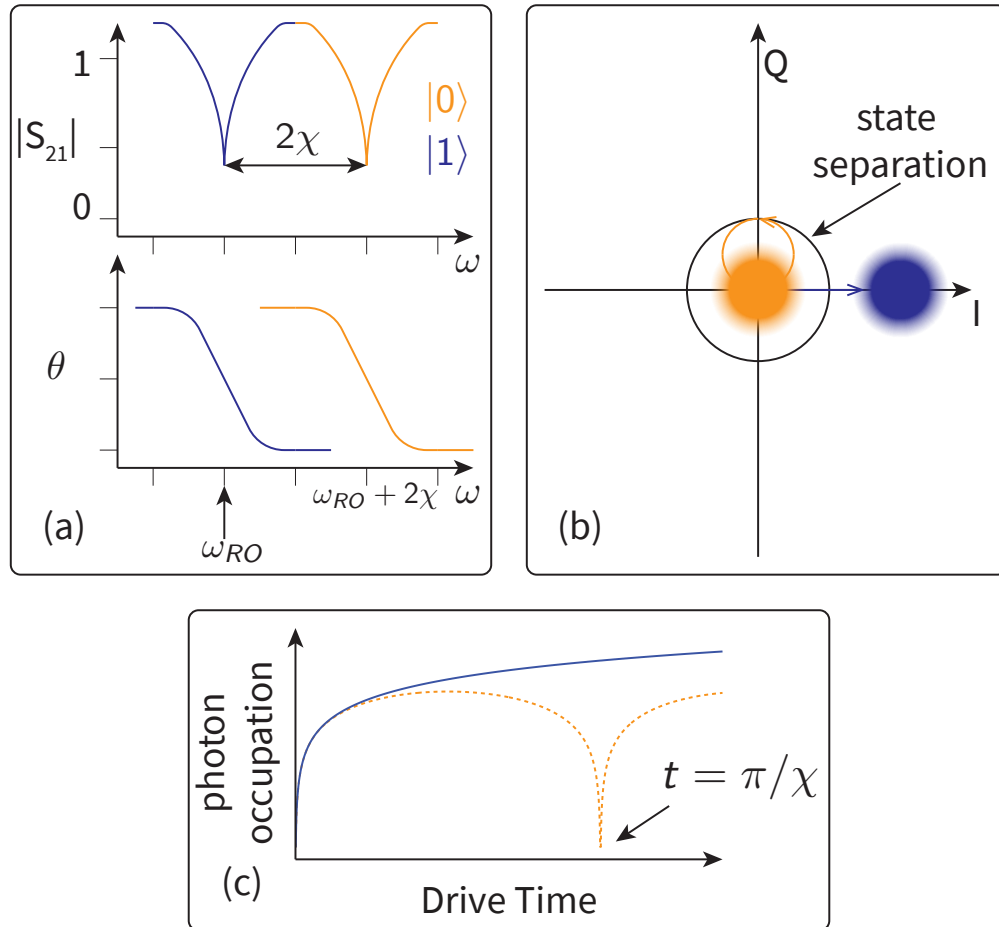
Figure 3.2: Pointer State Preparation.(a) One of the χ shifted peaks is driven rather than driving between the two possible resonances. For example, the $|1\rangle$ peak is driven here. (b) and (c) If the qubit is in the $|1\rangle$ state, photon occupation increases in the cavity. If the qubit is in the $|0\rangle$ state, photon occupation oscillates at a frequency π/χ. At a time π/χ, a resonator with a qubit in the $|0\rangle$ state will have ideally returned to vacuum, while the $|1\rangle$ state would have been driven out to some large photon number. The qubit state can then be measured by discriminating these two cavity photon states [62].

While the previous measurement scheme relied on measuring the amplitude and phase of reflected or transmitted microwave signals, a fundamentally different scheme can be realized by measuring the number of photons in the qubit's readout cavity [62]. Two critical steps are needed to do this. Firstly, the qubit's state must be accurately (and therefore quickly) mapped onto the photon occupation of its readout resonator. Naively, this can be done by simply driving the cavity at one of the

two expected χ-shifted peaks. If the qubit is in one state, the cavity is being driven on resonance, and photons build in the cavity. If the qubit is in the other state, the cavity is being driven off resonance, and the photon number in the cavity oscillates with a period determined by the detuning 2χ. By selecting a drive time corresponding to π/χ, the two possible photon numbers are maximally separated. This process is referred to as 'Pointer state preparation', and is depicted in Figure 3.2

In practice however, a few adjustments are necessary. For example, photons leave the cavity into any available port P_i at some rate determined by the coupling κ_i. Additionally, the cavity drive tone will have some spectral width, and will excite the unintended frequency at some rate. Conditioning of this signal with exponential envelopes or windowing functions will prove necessary in order to prepare these pointer states with high fidelity.

The next crucial step is the discrimination between the two possible photon occupations of the cavity. This is accomplished with a novel circuit element, known as a Josephson Photomultiplier (JPM).

3.2.1   The JPM

The JPM is essentially a phase qubit, operating as a threshold photon detector [63]. A circuit diagram is shown in Figure 3.3. Initial JPM designs consisted of a simple current-biased Josephson junction, shown in Figure 3.3a. Incident photons excited the JPM, and a current bias was calibrated so that excited states would tunnel and skip down the washboard, while the ground state would remained trapped in a potential well. The skipping particle leads to a measurable voltage of $2\Delta/e$. While qubits were successfully measured with this simple JPM, readout fidelity was limited to $\approx 65\%$ due to a number of issues, and backaction of the JPM due to the junction being in the voltage state was significant[5].

---

[5]See [64] for a full description of this work.
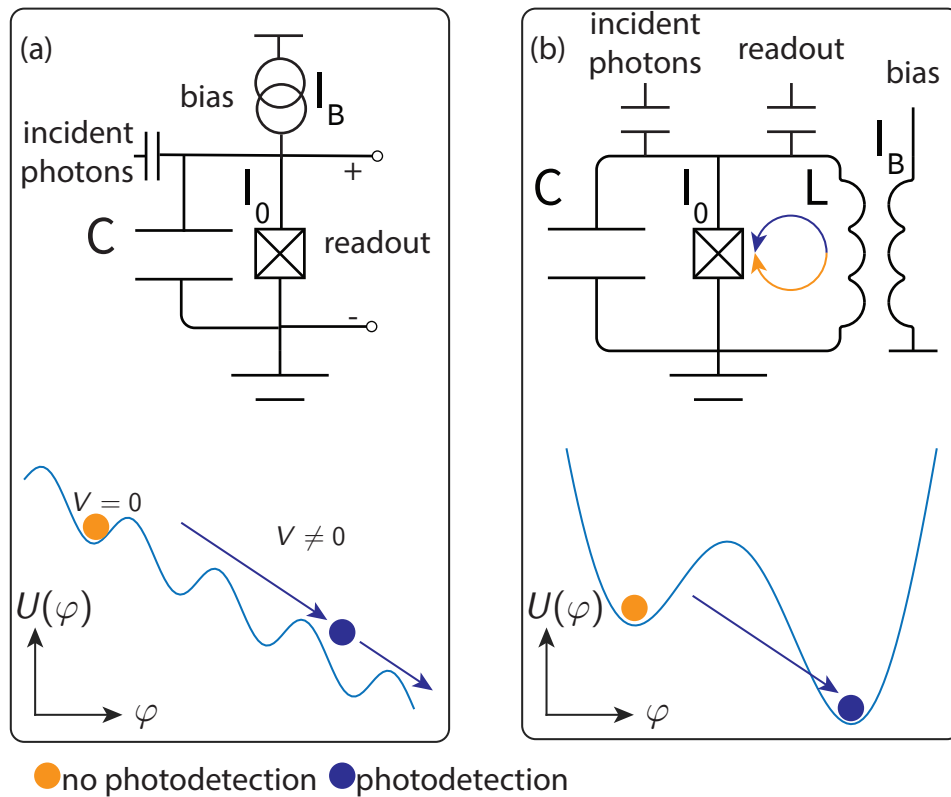
Figure 3.3: JPM Circuit Diagram. (a) Generation 1 JPM. A simple current-biased Josephson junction, modelled on early phase qubit designs. The junction was directly current biased, and readout was performed by measuring the voltage across the junction. Photodetection resulted in tunneling out of the metastable well and the phase particle running down the tilted washboard, corresponding to a voltage of $2\Delta/e$. A shunt capacitance brings the resonance of the circuit down to that of the photons to be measured. (b) Generation 2 JPM. Shunt inductor added so that a detection event only produces a single phase-slip. Readout is done with microwave reflectometry, and the JPM potential is tuned with an inductive current bias line.

One of the main factors limiting fidelity in this initial generation was photons reflecting off of the JPM and simply traveling back towards the readout resonator, rather than being absorbed and promoting excitations. To mitigate this, an auxiliary 'capture cavity' was introduced. This cavity is capacitively coupled to the JPM at some coupling rate g_{CJ} ,which allows the frequency of the cavity to be tuned by roughly this range by tuning the JPM frequency. Rather than directly detect photons in the qubit's readout resonator, the capture cavity is tuned on resonance with the readout resonator in order to transfer some of the photons. After some time, the capture cavity is detuned from the readout resonator, so as to 'capture' the photons inside and prevent them from traveling back to-

wards the readout resonator. The JPM is tuned on resonance with this cavity, and the detection performed.

In order to keep the JPM from switching fully into its voltage state during a switching event, an inductive shunt was added. This adds a quadratic term to the potential that can be tuned by selecting a β_L to have at most two metastable energy wells in the potential energy. Switching events consist of a single tunneling event, from an initial well into an adjacent well. This produces a single 'phase-slip', and the final state of the JPM can be measured by distinguishing which well the phase particle is in. The phase at the minima of these two potential wells correspond to opposing circulating currents in the junction-inductor SQUID loop. This solution was also used to develop flux-biased phase qubits, for similar reasons [65]. A large shunt capacitor brings the frequency of the system down to a range that spans the frequencies of photons to be detected.

The Hamiltonian for the new (unloaded) system is given by the sum of capacitive and inductive energies, identical to that of a phase qubit given in Section 1.2.2. Assuming a shunt capacitor and inductor C_s and L_s,

$$H(Q, \varphi) = \frac{Q^2}{2C_s} - E_j \cos\varphi + \frac{1}{2L_s}\left(\frac{\Phi_0}{2\pi}\right)^2\left(\varphi - \frac{2\pi\Phi_{ext}}{\Phi_0}\right)^2, \qquad (3.17)$$

where φ is the phase across the junction. The potential energy of the JPM can be written as

$$U(\varphi)/E_j = -\cos\varphi + \frac{1}{2\beta_L}\left(\varphi - \frac{2\pi\Phi_{ext}}{\Phi_0}\right)^2. \qquad (3.18)$$

The shape of this potential is is defined by the dimensionless parameter $\beta_L = L_s/L_J$ and tuned by an external flux Φ_{ext}. β_L is simply a ratio of inductances that determine whether the potential is mostly a parabola (from the linear shunt inductor) or a cosine (from the nonlinear Josephson junction). Since the JPM is intended to be a single-bit detection circuit (0 or 1), β_L is selected so that at most, only two wells are allowed in the potential. At the end of a qubit measurement, the JPM

will be in one of two potential wells, representing the binary measurement output.

3.2.2   Experiment
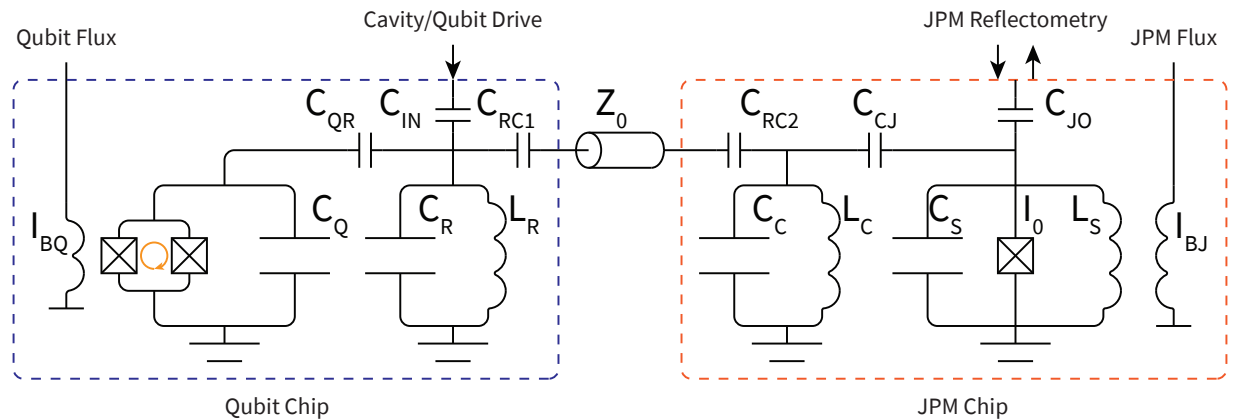
Figure 3.4: Circuit schematic for qubit measurement with JPM. On the qubit chip, a tunable qubit is coupled to a half-wave readout resonator. The output of this resonator is coupled via a coaxial cable to the input of a capture cavity on the JPM chip. This cavity is capacitively coupled to the JPM, and the JPM has a flux bias line and capacitively coupled port for microwave reflectometry.

In order to perform this experiment, two devices were fabricated. The qubit device consisted of two tunable rectmons coupled to a half-wave readout resonator. The second device consisted of the JPM and capture cavity which was also a half-wave resonator . The JPM was also capacitively coupled to a readout port in order to measure spectroscopy of the JPM using microwave reflectometry. A full circuit diagram is shown in Figure 3.4, and images of the devices are shown in Figure 3.5.

The protocol for performing qubit measurement with the JPM is shown in Figure 3.6. The JPM is initially tuned to its maximum frequency, so as to decouple the JPM from the other components, and to reset the phase particle into a single deep well. The JPM is then tuned to a frequency on resonance with the capture cavity. This depletes any photons left over in the cavity from the last experiment by coupling the photons to the lossy dielectric in the JPM shunt capacitor. Next, the qubit is manipulated to perform whichever experiment is being conducted. When it is time to measure the qubit, the JPM is tuned so as to shift the capture cavity on resonance with the readout

Figure 3.5: Image of qubit and JPM devices. (a) Qubit device, consisting of a two tunable qubits coupled to a half-wave readout resonator. Only one of these qubits was used in the experiment. (b) JPM device, consisting of the JPM (I_0, C_S, and L_S in parallel), bias line, and capacitors for coupling to the capture cavity, and coupling to a readout reflectometry port.
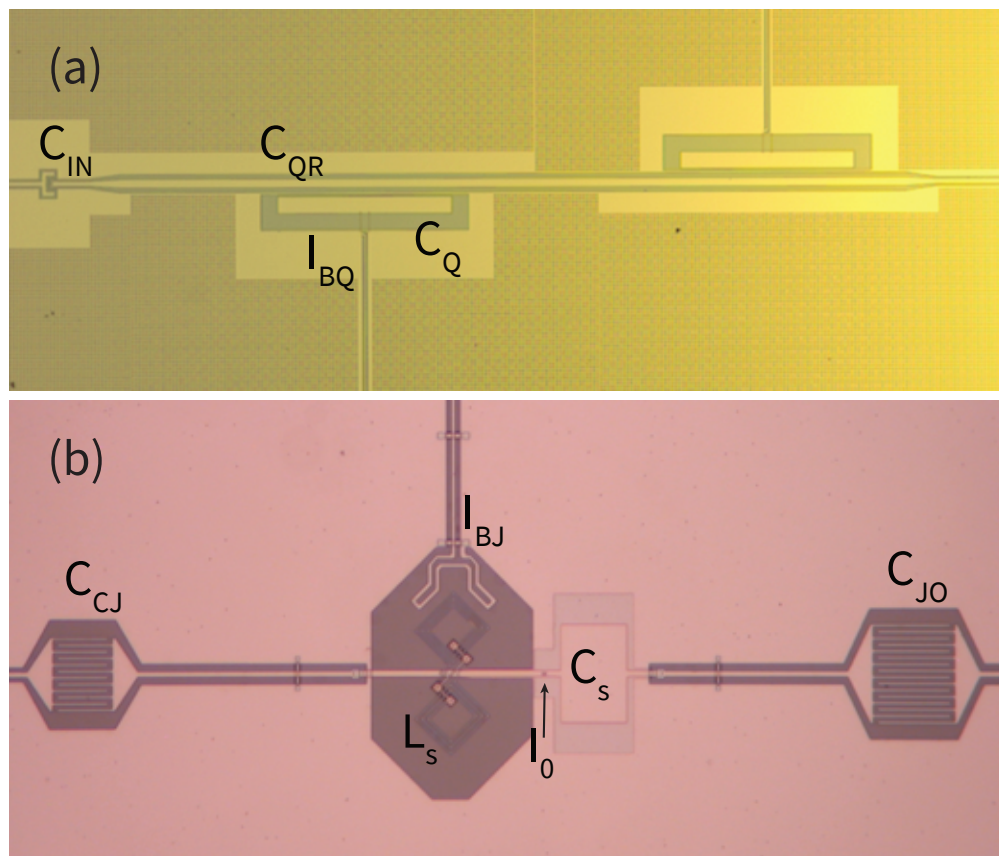
resonator. The readout resonator is driven to prepare the pointer states shown in Figure 3.2. The timing of this drive and length of the resonant coupling is optimized to maximize photon number separation of the two qubit states. Next, the JPM is tuned on resonance with the capture cavity, and photons in the cavity are absorbed by the JPM, promoting excitations to higher energy levels. With a large enough number of bound states in this potential well, the levels can be approximated as a harmonic ladder, so that a single frequency of photons can excite up to many energy levels higher. This step must be quick, as the T_1 of the JPM is on order of a few nanoseconds, and the higher states are decaying while they are being excited. Finally, the JPM is tipped to a bias point with a shallow metastable well so that excited states tunnel into the adjacent potential well, but the ground state remains in the initial well. At the end of the measurement, the JPM is measured in reflection, utilizing the same heterodyne circuit described in Section 3.1. The next experiment can then be performed, as the JPM is reset into its initial well again. Each of the bias levels and times for these steps were fed into an optimizer that maximized the difference in switching probability. With the JPM protocol optimized, the same readout procedure can be performed at the end of any qubit experiment.

The qubit chip was measured and verified in a dilution refrigerator at Syracuse, and then sent to collaborators at the University of Wisconsin-Madison for measurement with the JPM device. Example qubit experiments performed with the JPM are shown in Figure 3.7. Full results have been published [11] and an overview of the results are discussed here. The raw single-shot measurement fidelity using the JPM was 92% . The main source of this infidelity was qubit relaxation during the measurement, followed by dark counts due to imperfect pointer state preparation.

The depletion step was not one that was anticipated before this experiment. While measuring the backaction of the experiment, it was noticed that JPM switching events Stark-shifted the qubit by some amount. This implied that some number of photons were being added to the readout resonator by the voltage pulse produced by the switching event. Utilizing the dielectric loss of the JPM to dissipate these residual photons was a key innovation, and proved critical for demonstrating
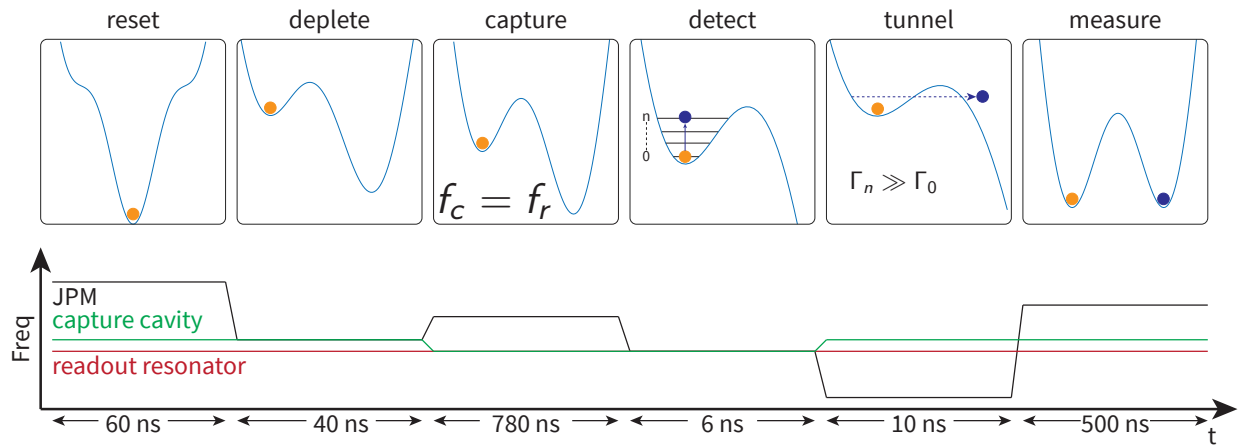
Figure 3.6: JPM Measurement Protocol. From left to right. JPM is reset into a single deep well, maximally detuned from the rest of the system. JPM is tuned on resonance with the capture cavity to deplete any photons left over from last detection. Capture cavity is tuned on resonance with the readout resonator, as the pointer-states are prepared (see Fig. 3.2). JPM is tuned on resonance with the capture cavity, and photons in the cavity induce excitations to higher states in the initial well. JPM is then tuned to a shallow bias point, so that higher energy states tunnel into the adjacent well. Finally, the JPM is brought to a point where the two wells are maximally separated, allowing for microwave reflections to distinguish the two states. (Based on Fig. 3 of Opremcak, et al. [11])
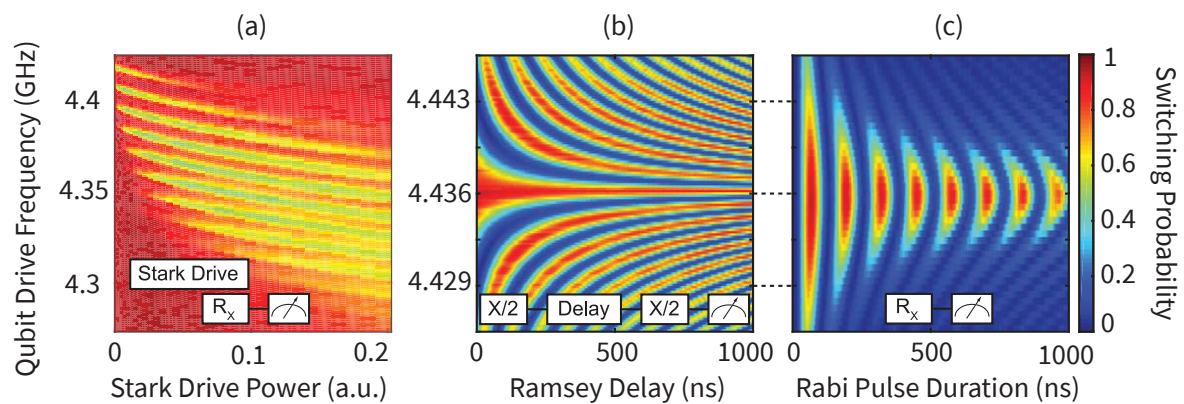
Figure 3.7: Qubit characterization experiments performed with JPM measurement. (a) Stark shift measurement [66]. (b) Ramsey Fringes. (c) Rabi Oscillations. (Based on Fig. 3 of Opremcak, et al. [11])

QND readout[6].

These results are very promising. Critically, there were no isolators used between the JPM and the qubit device. This is the first demonstration of high-fidelity readout of a superconducting qubit that did not require microwave isolators protecting the qubit from amplifier noise. This satisfies one of the stated goals of this method, as outlined at the end of Section 3.1. There are also many avenues for improvement. Since these experiments, the group at UWM has measured single-chip devices without a capture cavity with even higher fidelity. Coupling the JPM directly to the readout resonator saves space on a chip and simplifies the measurement protocol, both of which make the device even more scalable.

While our collaborators at UWM worked on optimizing the readout fidelity of the JPM, my attention turned towards coupling the JPM to a digital readout circuit. Reading the JPM in reflection with a HEMT means that a significant amount of overhead is still required, and in some way defeats the purpose of using the JPM over a quantum-limited amplifier. Keeping with the theme of interfacing the qubit with SFQ logic, several approaches were considered for encoding the final state of the JPM to SFQ logic. Two of these approaches, one utilizing ballistic fluxons and another utilizing flux comparators, are presented in the following chapters.

---

[6]Quantum-Non-Demolition. A QND measurement does not impact the subsequent dynamics of the system being measured. See Figure 4 of [11] for more details

Chapter 4

JPM-SFQ Detection with ballistic fluxons

The use of propagating fluxons as a direct probe of the state of a qubit was first investigated theoretically in [67]. Here, a ballistic JTL is coupled directly to a superconducting flux qubit, whose states correspond to different circulating currents [68]. The flux from the qubit induced a small current in the ballistic JTL, effectively forward or reverse biasing the fluxon as it travelled through the line. This maps the state of the qubit onto the time-delay of the fluxon. In order to minimize backaction from the JTL on the qubit and thus maintain QND readout, an exceedingly weak coupling strength between the JTL and qubit was required. This prevents the qubit measurement from being performed in a single shot. A full circuit for this approach was developed in [69] and improved in [70], including additional components to detect the induced delay. Recently, this method for measuring flux qubits has been developed further and studied with numerical simulations in [71–74]. In addition to these theoretical studies of JTL-based flux qubit readout, an experimental implementation of flux qubit readout using traveling fluxons in an annular Josephson junction was demonstrated in [75].

In contrast to these schemes for direct qubit readout with propagating fluxons in a JTL, the detection of circulating current states from JPM-based qubit measurement has clear advantages. The circulating current being detected in the JPM is one or two orders of magnitude larger than that in a flux qubit. Furthermore, the JPM acts as a buffer between the SFQ circuitry and qubit since, out-
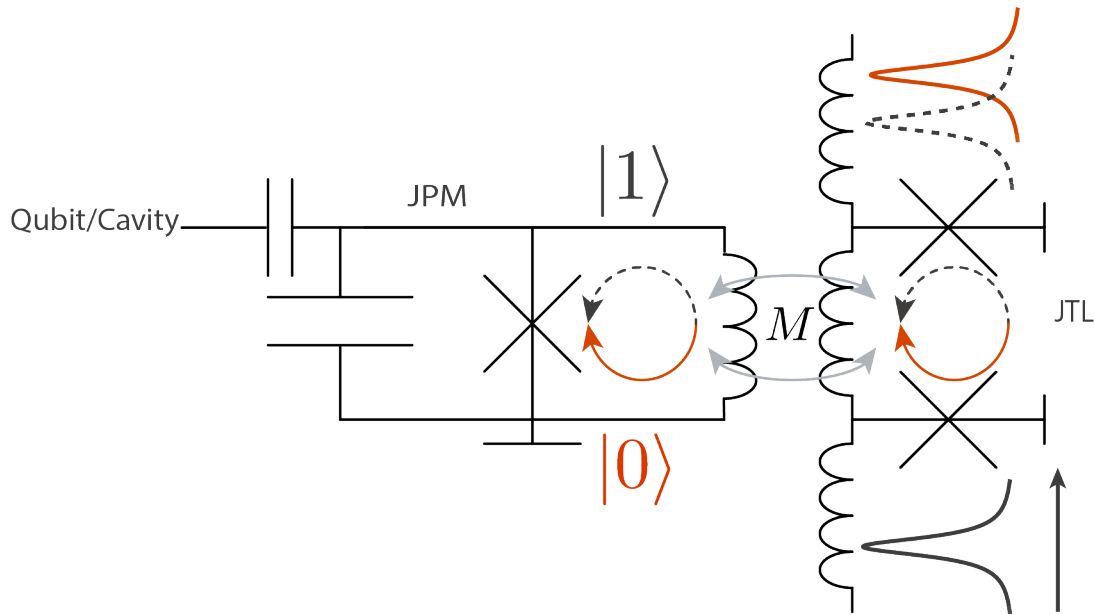
Figure 4.1: JPM coupled to ballistic JTL. The opposing arrows in the rf-squid loop represent the two circulating current states of the JPM. The ballistic JTL is shown on the right-hand side, and one cell is coupled to the JPM inductor through a mutual M. Fluxons traveling through the JTL are forward or reverse-biased and pick up a conditional time delay based on the state of the JPM.

side of the brief moment when the JPM is on resonance with the qubit cavity, the JPM is otherwise far detuned. Thus, dissipation or noise in the JTL that is coupled to the JPM will not be directly coupled back to the qubit being measured. Finally, because the circulating current states in the JPM following the nearly QND measurement of the qubit are completely classical, the detection of the JPM state with propagating fluxons does not need to be QND. This allows for a stronger coupling to be used between the JPM and the JTL.

4.1 Design

Our circuit for converting the state of the JPM to an SFQ signal is related to the earlier work from [67] and [70], for SFQ-based readout of a flux qubit, where the time delay of a propagating fluxon in a coupled ballistic JTL is compared to a reference ballistic JTL. Upon discrimination of the delay, the SFQ output of the measurement result can then be optionally converted to a dc pulse for room-temperature detection. Conventional RSFQ logic cells operating at $4\,\mathrm{K}$ typically utilize Josephson
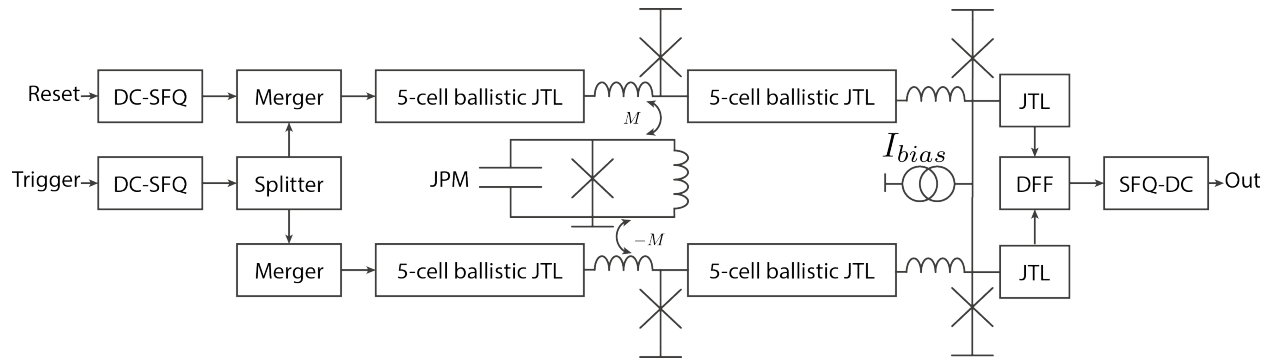
Figure 4.2: Circuit diagram of the JPM-SFQ interface and delay-detection circuitry.

junctions with critical currents on the order of $100\,\mu A$. Because the JPM will need to operate at the same low-temperature stage of a dilution refrigerator along with the qubit, utilizing millikelvin SFQ technology will be critical [76]. In addition, because the JPM junction, with $I_c = 1\ \mu A$, must be fabricated with the same critical current density as the SFQ circuitry, critical currents for the SFQ elements will be in the $1 - 10\ \mu A$ range. The combination of low-I_c junctions with inductive biasing results in zero static and minimal dynamic power dissipation, thus allowing the circuit to operate at qubit temperatures ($< 50\ mK$) with a minimal heat load on the cryostat, as analyzed in [77].

4.1.1   Coupled ballistic lines

Figure 4.2 shows the schematic of our circuit for implementing the detection of the state of a JPM following qubit measurement using SFQ circuitry. The design incorporates two ballistic JTLs – one along the top of the schematic and the other along the bottom – with equal and opposite coupling between the central cell of each JTL and the JPM inductor. This arrangement causes the net flux in one of the central JTL cells to increase, thus slowing down the fluxon propagation, while the net flux decreases in the central cell of the other JTL, which speeds up the fluxon propagation there. Thus, this scheme enhances the relative delay between fluxons propagating in the two JTLs. In addition, this results in the flux induced back into the JPM from one passing fluxon to be canceled out by the flux induced by the second fluxon, thus minimizing the flux coupled to the JPM from the JTLs during the measurement. The ballistic lines consist of 12 JTL cells, with parameters $L_{JTL} = 41$ pH
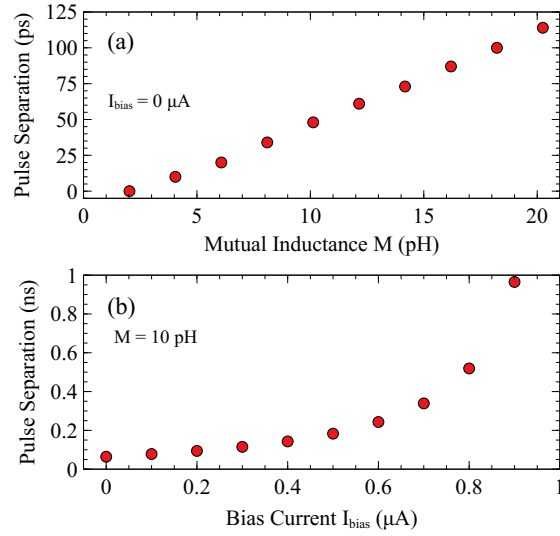
Figure 4.3: Dependence of induced fluxon delay on (a) bias and (b) mutual inductance.

and $I_c = 2$ μA. This results in a normalized Josephson length $\tilde{\lambda}_J = \sqrt{\hbar/2eI_c L_1} = 2$ cells.

A significant enhancement of the relative fluxon delay can be achieved by adding a separate, negative current bias to the final cell of each of the ballistic JTLs. Biasing of only this last cell adds to the delay of the delayed fluxon as it travels through the ballistic JTL, but minimally perturbs the other fluxon. This bias current can be used to enhance the fluxon delay by over an order of magnitude with a small mutual inductance (Fig. 4.3). A 10 pH mutual is targeted to minimize backaction while allowing for a sufficient delay (> 15 ps) to ensure appropriate margins of the delay detection circuit.

4.1.2   Triggering

A standard DC-SFQ converter and splitter are used to launch the fluxons into the ballistic JTLs at the same initial starting time. Combiners are added to both lines so that a reset pulse can be added for the delay detection circuitry. Adding combiners to both lines ensures that the total time delay of both ballistic paths are identical in the absence of a JPM circulating current. In future designs, additional components can be added to reset the delay detection circuitry automatically, making

a secondary trigger unnecessary.

4.1.3   Delay Detection

The delay detection circuit is modeled after delay demodulation circuitry used in superconducting analog-to-digital converters [78]. Since there are only two possible states of the JPM, the detection circuit only needs a single bit of resolution to distinguish the pulse arrival times. A single D Flip-Flop (DFF) can be used to determine the order of the arriving pulses. If the data pulse arrives first, the following clock pulse produces a logical 1. If the clock pulse arrives first, the following data pulse produces a logical 0 at the output. Sending a reset pulse following this detection resets the DFF, with the resulting output ignored.

4.2   Backaction

Although the backaction requirements are much less severe for detecting the state of a JPM rather than the original schemes for the direct readout of a flux qubit, it is nonetheless important to consider the effects of the ballistic JTLs coupled to the JPM. One concern is that the coupling of the JTLs to the JPM will perturb the tunneling rates of the biased JPM, thus impacting the qubit measurement fidelity of the JPM. Additionally, for sufficiently strong mutual inductances between the JTLs and JPM, fluxons traveling through the ballistic JTLs could couple enough flux back into the JPM to induce a switching event, thus perturbing the JPM state and coupling noise back into the qubit-cavity through the subsequent ringdown oscillations of the JPM. However, if the coupling mutual is low enough so as not to induce a tunneling event, yet large enough to result in a resolvable fluxon delay, the fluxon-based readout should be considered a non-destructive readout (NDRO) method, with no impact on the state of the JPM or any coupled qubit systems. We can analyze the coupling of the JPM to the ballistic JTL by modeling the JPM coupled to a single cell of an unbiased, unshunted JTL. The resulting model is essentially two coupled rf SQUIDs with quite different $\beta_L \equiv 2\pi I_c L / \Phi_0$

parameters: 4.8 for the JPM and 0.01 for the JTL, and effective masses, as determined by the $3\,\text{pF}$ shunt capacitor of the JPM and the much smaller, $80\,\text{fF}$ self capacitance of the JTL junction. The inductive contribution of the coupled system to the potential energy is given by

$$U_L(\Phi_1, \Phi_2) = -\frac{1}{\beta_M} \left(\frac{\tilde{\Phi}_1^2}{L_1} + \frac{\tilde{\Phi}_2^2}{L_2} - \frac{2M}{L_1 L_2} \tilde{\Phi}_1 \tilde{\Phi}_2 \right) \tag{4.1}$$

where L_1 is the JPM inductance, L_2 is the JTL inductance, $\beta_M = \left(1 - M^2/L_1 L_2\right)$, and $\tilde{\Phi}_i = \Phi_i - \Phi_{i,x}$. The offset term $\Phi_{i,x}$ is the externally applied flux and Φ_1 and Φ_2 are the total flux in JPM and JTL loops, respectively. The flux added to the coupled JTL cell comes from any residual current bias and can be considered to be 0 for this analysis. For a realistic set of parameters ($L_1 = 1\,\text{nH}$, $L_2 = 40\,\text{pH}$, $M = 10\,\text{pH}$), the prefactor of the inductive potential term ($1/\beta_M$) is quite nearly unity (0.995), resulting in a negligible change to β_L for the JPM. Additionally, the prefactor of the coupling term in (4.1) is ~ 0.0025, and is thus dominated by the diagonal terms in the potential with a negligible contribution to the tunneling behavior of the JPM. The small capacitance of the JTL junction contributes to the kinetic term of the coupled Hamiltonian. However, since the plasma frequency of this junction is on the order of $100\,\text{GHz}$, compared to $\sim 5\,\text{GHz}$ for the JPM, and with parasitic capacitance between the JPM and JTL negligible, we can neglect any effect of the JTL junction capacitance on the Hamiltonian for the coupled system. If the coupled JTL cell contributes negligibly to the behavior of the JPM, we can also neglect the contributions of the other segments of each ballistic JTL beyond the central unit cell of each one. By keeping the mutual inductance and parasitic capacitance between the JPM and JTL low, we can treat the elements as independent systems.
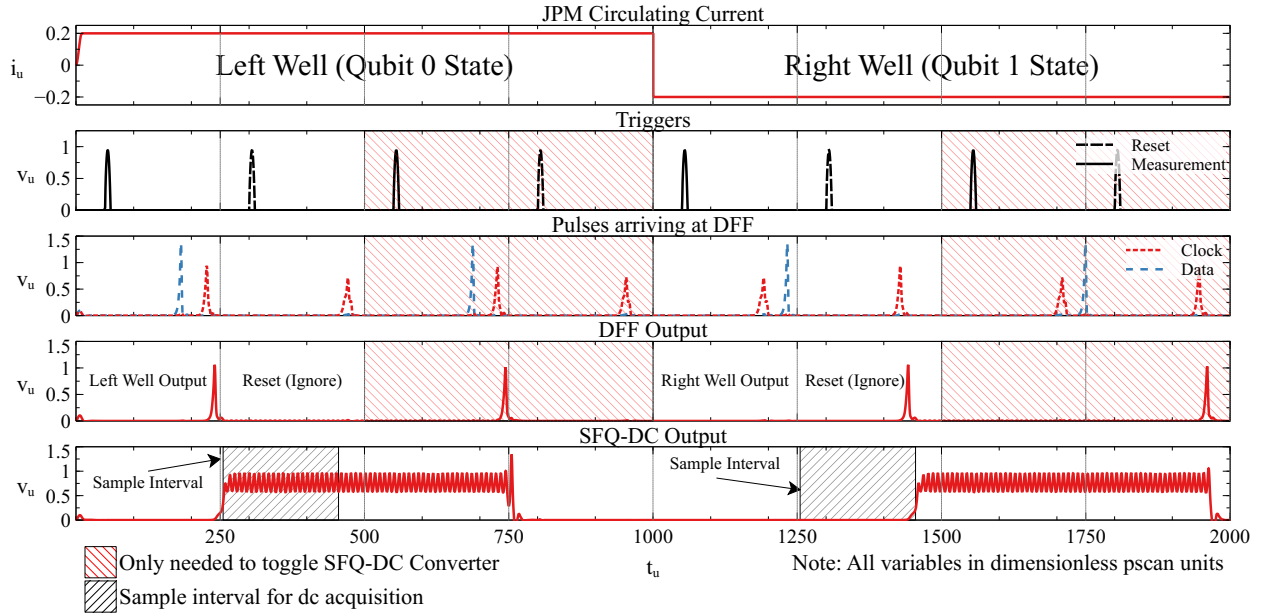
Figure 4.4: Simulation results of the JPM-SFQ interface utilizing ballistic fluxon detection.

4.3   Simulation results

The circuit shown in Fig. 4.2 was simulated in WRspice [79] and PSCAN2 [80]. Results of the PSCAN2 simulation of the full circuit are shown in Fig. 4.4. When the JPM is in the left well (qubit 0 state), the data pulse arrives at the DFF first, resulting in a logical 1 as an output. A subsequent reset pulse results in a logical 0, which is ignored. When the JPM is tilted into the right well (qubit 1 state), the clock pulse arrives at the DFF first, resulting in a logical 0 as an output. The reset pulse then results in logical 1, which is ignored. If an SFQ-DC converter is used to convert the measurement to a dc signal to be detected at room temperature, the entire sequence is repeated in order to toggle the SFQ-DC converter back into the off state. Using PSCAN2 [80], a margin analysis can be performed to optimize parameter values. Optimized margins for junction area, inductance values, bias currents, and mutual inductances are shown in Table 4.1. Margins greater than 25% are considered acceptable for the SeeQC fabrication process [81].

While the ballistic readout approach seemed viable given the successful simulation results, layout of the device proved very difficult. The topology of using two ballistic lines resulted in a closed

junction area	40%
inductances	32%
bias currents	36%
mutual inductances	38%

Table 4.1: Optimized parameter margins

loop formed around the JPM. Initial efforts to design the device were also heavily constrained by the mutual couplings needed. During the layout stage of this design, an alternative method was suggested by Dr. Tom Ohki, who had performed similar experiments on phase qubits during his time as a postdoc. This alternative method is discussed below.

Chapter 5

JPM-SFQ Detection with flux comparator

The use of an SFQ comparator to measure phase and flux qubits was introduced in the early 2000s [82], and developed further over the next 5 years [83–86]. However, this effort was abandoned shortly after, due to two elements: the development of the transmon qubit and its high coherence made phase and flux qubits less attractive, and the discovery that dielectric loss was responsible for short coherence times of qubits made it very unattractive to continue fabricating qubits using the same fabrication methods as SFQ circuits.

The development of the JPM makes this work relevant again, as the JPM is very similar to the phase qubits used in these experiments. In this section, an SFQ comparator is investigated as a readout device for a JPM, and a device is fabricated and measurement results discussed.

5.1   SFQ Comparator

The comparator is a standard SFQ circuit element used mainly in SFQ analog-to-digital converters [87–89]. It consists of two identical junctions that operate as a decision making pair. Both junctions are biased close to their critical currents, and the signal to be compared is injected between them. This current biases one of the junctions closer to its critical current than the other, and this junction switches when a pulse is applied across the comparator. If the top junction switches, the output
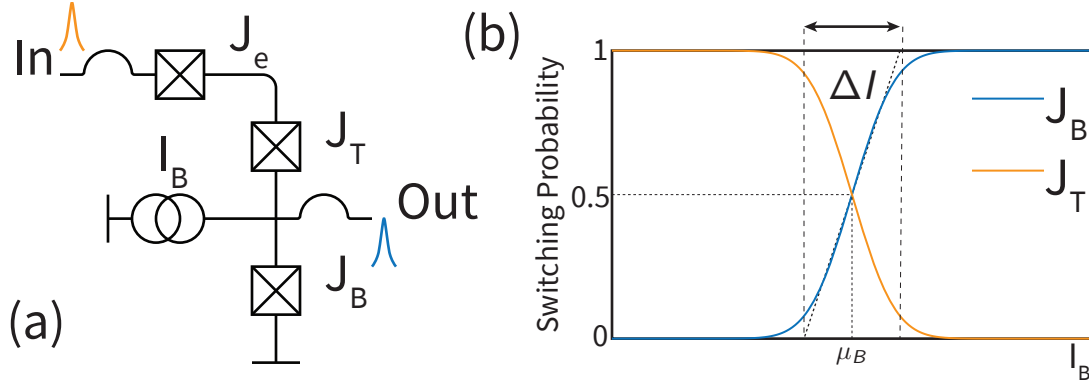
Figure 5.1: SFQ Comparator. (a) The comparator consists of two junctions of equal value, J_T and J_B in series. The current being compared I_B is injected in between the two junctions. When an SFQ pulse arrives at J_T, the sign of I_B determines which of the two junctions is closer to its critical current. If J_B switches, an SFQ pulse is sent out of the comparator. If J_T switches, the output is held low, and the escape junction J_e switches in tandem to cancel out the voltage and prevent a pulse from being emitted back into the previous circuitry. (b) Switching probabilities for both comparator junctions as a function of I_b. The switching curves can be treated as error functions with width ΔI the measure of sensitivity of the comparator.

is shorted to ground through the bottom junction. If the bottom junction switches, this pulse is propagated out of the circuit.

In a perfect comparator, the switching probability of the bottom (top) junction as a function of applied signal would be a flat function with a perfect step from 0 to 100% (100 to 0%) switching probability at an applied current of μ_B. However, due to both thermal and quantum effects, this step is rounded. This function and its derivative are shown in Figure 5.1.

We will refer to J_B switching as the comparator itself switching, since this is what produces an output pulse. The switching probability of J_B is given by

$$p = \frac{1}{2} + \frac{1}{2} \operatorname{erf}\left(\sqrt{\pi} \frac{I_b - \mu_b}{\Delta I}\right), \tag{5.1}$$

where μ_b is the value of I_b corresponding to a 50% switching probability, and ΔI is the gray zone of the comparator [90]. The dependence of the gray zone on thermal and quantum effects is discussed below.

5.1.1 Thermal Dynamics

At high temperatures, the electrons in the comparator junction shunt resistors have thermal fluctuations that can kick the phase particle over the barrier, causing the junction to switch. This results in an effective current due to thermal fluctuations of

$$\Delta I \approx \alpha \sqrt{2\pi I_T I_c},\tag{5.2}$$

where α is a dimensionless parameter determined by the bias current flowing through both junctions, I_c is the critical current of each of the junctions (assumed to be the same), and I_T is a current given by

$$I_T = \frac{2e}{\hbar} kT,\tag{5.3}$$

where T is the electron temperature [86]. This temperature is given by [91]

$$T_e = \left(P/\Sigma\Gamma + T_p^5\right)^{1/5},\tag{5.4}$$

where $P = I_c \Phi_0 f$ is the power dissipated (for a junction with critical current I_c at switching frequency f), Σ is a material constant[1], Γ is the volume of the resistor, and T_p is the phonon temperature (temperature of the substrate).

The $100\,\mu\text{A}$ comparator junctions need a shunt resistance of $1.29\,\Omega$ to be critically damped. We can approximate a power due to a switching rate of the comparator junction. Assuming a sampling

---

[1] $2 \times 10^9\,\text{W}/(\text{K}^5\text{m}^3)$ for Pd-Au resistors [91]

rate of $1\,\text{MHz}$, and a substrate temperature of $100\,\text{mK}$, the electron temperature is $\sim 250\,\text{mK}$. Therefore the thermal effects of electrons in the shunt resistors limit the gray zone $\Delta I \sim 10\,\text{nA}$.

At temperatures below $100\,\text{mK}$, thermal switching is unlikely, and escape is dominated by quantum tunneling. The crossover temperature between the two regimes is given by [82]

$$T^* = \frac{\hbar \omega_p}{2\pi k_B} \left[\left(1 + \frac{1}{4\beta_c} \right)^{1/2} - \frac{1}{2} \left(\frac{1}{\beta_c} \right)^{1/2} \right], \tag{5.5}$$

which is $\sim 1.3\,\text{K}$ for the parameters we have used.

5.1.2   Quantum Regime

Below T^*, there is still some finite probability that the phase particle of the junction will tunnel through the barrier an cause an unintended switching event. This is represented as a current width that depends on the plasma frequency of junction,

$$\Delta I_Q = \frac{2e}{\hbar} \hbar \omega_p, \tag{5.6}$$

where the energy $\hbar \omega_p$ has taken the place of $k_B T$. The junction plasma frequency is determined by the critical current density and specific capacitance of the junction fabrication process, and is independent of area of the junctions (Eq. 1.18). For the SeeQC $100\,\text{A}/\text{cm}^2$ process, the plasma frequency is $\omega_p/2\pi \sim 45\,\text{GHz}$. This leads to $\Delta I_Q \sim 87\,\text{nA}$.
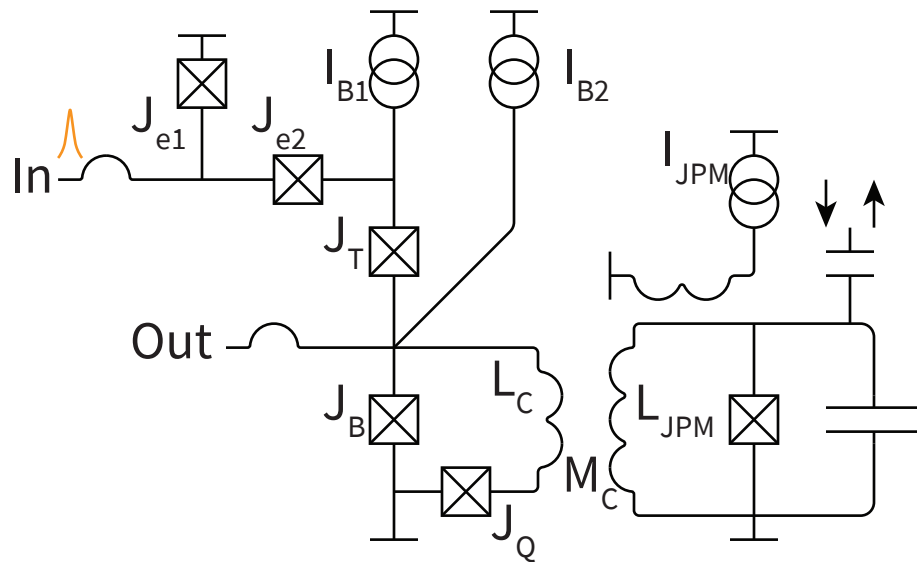
Figure 5.2: JPM-SFQ Comparator Circuit. A loop is made from the bottom comparator junction in order to convert a flux to a current. This loop is coupled to the JPM inductor with a mutual M_c. Another small junction J_Q is added to the loop in order to clear out any residual flux left in the loop as a result of switching. Two biases I_{B1} and I_{B2} are used to tune the phases of the two comparator junctions.

5.1.3 Comparator Simulation

The circuit used to demonstrate comparator readout is shown in Figure 5.2, and is heavily influenced by the circuits introduced to measure phase and flux qubits previously [83, 84]. A pickup loop is added in parallel with the bottom comparator junction, allowing for the comparator to sense a flux rather than a direct current. A secondary junction J_Q is also added, turning the loop into a Quasi-One-junction-SQUID (QOS), an element typically used in the comparators in high speed SFQ analog-to-digital converters [89]. Additional junctions J_{e1} and J_{e2} are also added before the comparator to act as a buffer stage and also to provide a path for a pulse to escape if J_T switches, rather than propagating back towards the input circuitry.

The required sensitivity of the comparator is dependent on the signal we expect to measure. The signal to be detected is a flux picked up from the JPM's inductor. At the end of a JPM measurement, the JPM is tuned to the symmetric bias point where both potential wells have the same depth (see

the last panel of Figure 3.6). The minima of these two wells correspond to circulating currents with equal and opposite direction I_L and I_R. The difference in flux that I_L and I_R couple into the comparator loop through the mutual inductance M_c is

$$\Delta\Phi_{CMP} = M_C\Delta I_{JPM} = L_{CMP}\Delta I_{CMP} \approx 10\,\text{m}\Phi_0. \tag{5.7}$$

Given the same JPM parameters from the device in Section 3.2, and a mutual inductance of $M_C = 15\,\text{pH}$, this results in a current signal induced in the comparator of $\Delta I_{CMP} \approx 1\,\mu\text{A}^2$. Assuming the quantum-limited gray zone calculated in the previous section, this device would yield a signal-to-noise ratio (SNR) of

$$SNR = \frac{\Delta I_{CMP}}{\Delta I} \sim \frac{1\,\mu\text{A}}{100\,\text{nA}} \sim 10, \tag{5.8}$$

which should be large enough for single-shot readout of the JPM.

Just as with the ballistic readout circuit, the comparator circuit in Figure 5.2 was simulated in WR-spice and PSCAN2 to determine optimal parameters. Values were targeted assuming that the critical currents of the comparator junctions were $\sim 100\,\mu\text{A}$. This is a relatively high critical current compared to the JPM critical current, and definitely higher than it needs to be. However, the standard cells available for DC-SFQ converters, JTLs, and SFQ-DC converters were centered around a JTL junction critical current of $100\,\mu\text{A}$, constraining the comparator in order to appropriately mate with these JTLs. In principle, lower I_c comparator junctions can be made, and this will be done in future generations. Simulation results from PSCAN2 are shown in Figure 5.3.

A margin optimization was performed to find which values of comparator parameters were most

---

[2]This assumes the comparator junctions are biased well below their critical current so that they can be modelled as linear inductors.
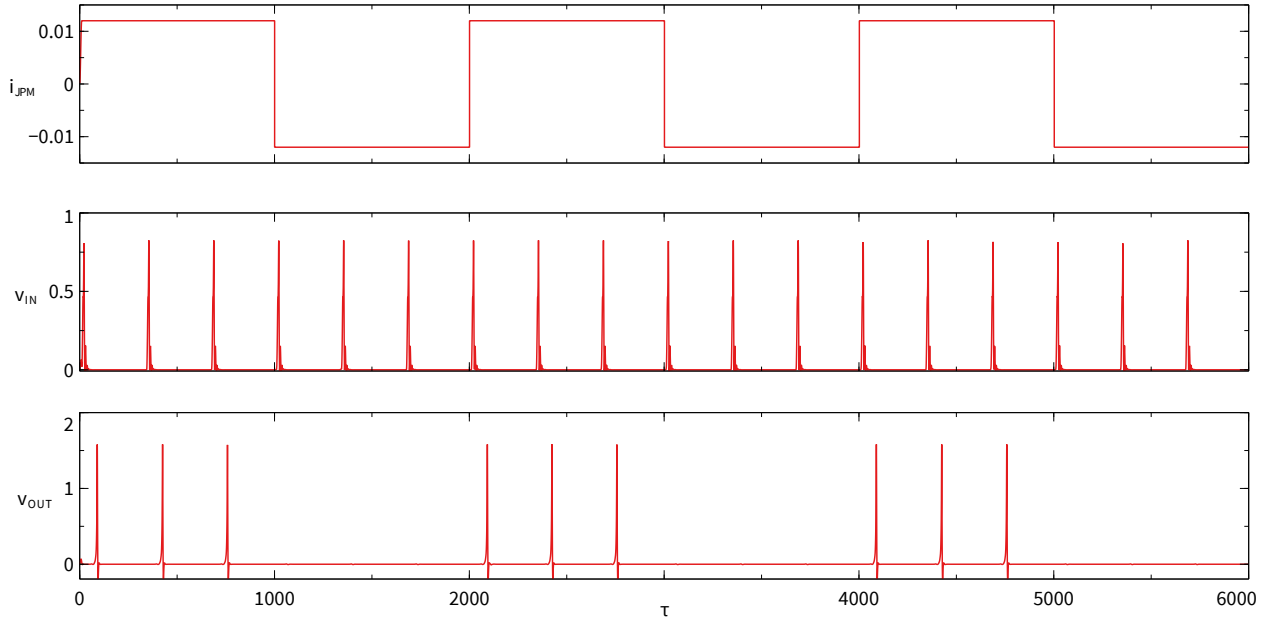
Figure 5.3: Comparator Simulation Results. (Top) Current in the JPM, modeled as a current source. Here, the JPM current is jumping back and forth from I_R to I_L, modeling the JPM alternating between the two potential wells. (Middle) Input pulses to the comparator. (Bottom) Output of the comparator. As expected, pulses are allowed to propagate through the circuit with the JPM in one state, but pulses are blocked in the other state.

Parameter	Symbol	Value
Comparator critical current	$J_{T,B,e1,e2}$	70 μA
Quantizing critical current	J_q	15 μA
Pickup Inductance	L_c	25 μA
Coupling Mutual	M_C	15 pH

Table 5.1: SFQ Comparator Target Parameters.

resilient to deviation due to fabrication errors. These values are given in Table 5.1.

5.2 Design

After the target circuit parameters were determined from simulation, a physical layout was generated to satisfy these parameters. First, I will describe the layout of the circuitry needed for JPM-based qubit readout, consisting of the JPM and its flux bias line and readout port, and the qubit's readout resonator. Then I will describe the layout of the comparator circuitry, consisting of the SFQ

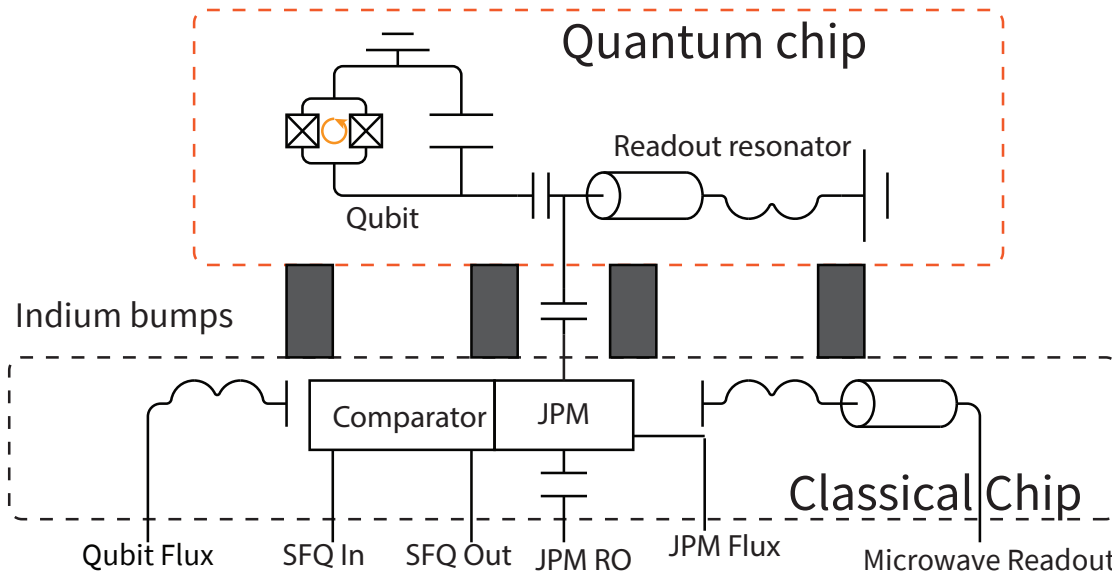Figure 5.4: Diagram for JPM-SFQ Comparator MCM. A qubit and readout resonator are fabricated on a top quantum chip. A JPM and reflectometry port are fabricated on the bottom chip. The JPM is coupled to an SFQ Comparator, with a digital trigger in and digital result out. All flux lines for JPM and qubit are on the classical chip. A readout port is also added to measure the readout resonator with microwaves.

cells and comparator pickup loop. The device was fabricated in collaboration with SeeQC, and fabricated according to their design rules (see Appendix 2 for more details).

The JPM was designed to have similar parameters to that used in [11], but for completeness the design methodology is explained again here. In order to achieve the double-well potential, a β_L of $2 - 5$ is needed. Target parameters of $L_{JPM} = 1\,\text{nH}$ and $I_c = 1\,\text{μA}$, result in $\beta_L = 3$. The readout resonator is designed to resonate at $5\,\text{GHz}$. Accordingly, a JPM shunt capacitance of $C_s = 3\,\text{pF}$ gives the JPM a maximum frequency of $\sim 6\,\text{GHz}$. This leaves the JPM detuned when biased to its single-well idle state, but still near enough to the readout frequency that it can be tuned on resonance by a fast bias pulse. In a departure from previous experiments, no capture cavity was utilized in this device. As mentioned in Section 3.2.2, preliminary measurements from collaborators at UWM demonstrated that high-fidelity readout could still be achieved with the JPM directly coupled to the qubit's readout resonator.

For the same reasons as those explained in Section 2.2, it is advantageous to utilize an MCM architecture. This allows for the SFQ circuitry to be fabricated in a standard foundry process on one substrate, and the qubit device to be fabricated in a process optimized for coherence. The JPM was fabricated on the SFQ chip for several reasons. Firstly, the coherence time of the JPM is not crucial for photodetection, so the lossy elements associated with SFQ fabrication should not impact the fidelity of the JPM readout. Secondly, the JPM junction and shunt capacitor can be easily fabricated in a standard SFQ process. Additionally, coupling from the JPM to a comparator is much easier if both devices are on the same chip. This is shown in Figure 5.4

The readout resonator is coupled to the JPM through the gap between the two chips (5 μm of vacuum). In this case, a coupling capacitance formed between the resonator and JPM in order to allow for the photons in the resonator to efficiently excite the JPM. The T_1 of the JPM can be assumed to be the RC time constant determined by the dielectric used for the shunt capacitor [92]. The standard SeeQC process uses SiOx as the insulation between metal layers, with a quality factor given by $Q_{SiOx} \sim 300$. Assuming a JPM frequency of 6 GHz, this results in an estimated T_1 of a few nanoseconds. A swap time of 5 ns was chosen as a target rate.

For two capacitively coupled oscillators denoted i and j, the coupling rate is given by [37]

$$2g_{ij} = \frac{C_{ij}}{\sqrt{C_i C_j}}\sqrt{\omega_i \omega_j}.$$
(5.9)

The coupling needed for a 5 ns swap time is given by $\pi/2g_{RJ} = 5$ ns, or $g/2\pi = 50$ MHz. Since the photon swap happens on resonance, $\omega_R = \omega_J$, the required coupling capacitance is $C_{RJ} = 35$ fF. The capacitance must be formed between the two chips, a parallel-plate capacitance must be formed with vacuum as the dielectric. For a 5 μm gap between the two chips, the area required for this coupling strength is 140 μm × 140 μm. The size of this capacitor pad would result in a significant capacitance to ground for the JPM. It was decided to utilize the same capacitor pad to couple to the resonator and to form the shunt capacitance utilizing the dielectric layer I2. This results in a
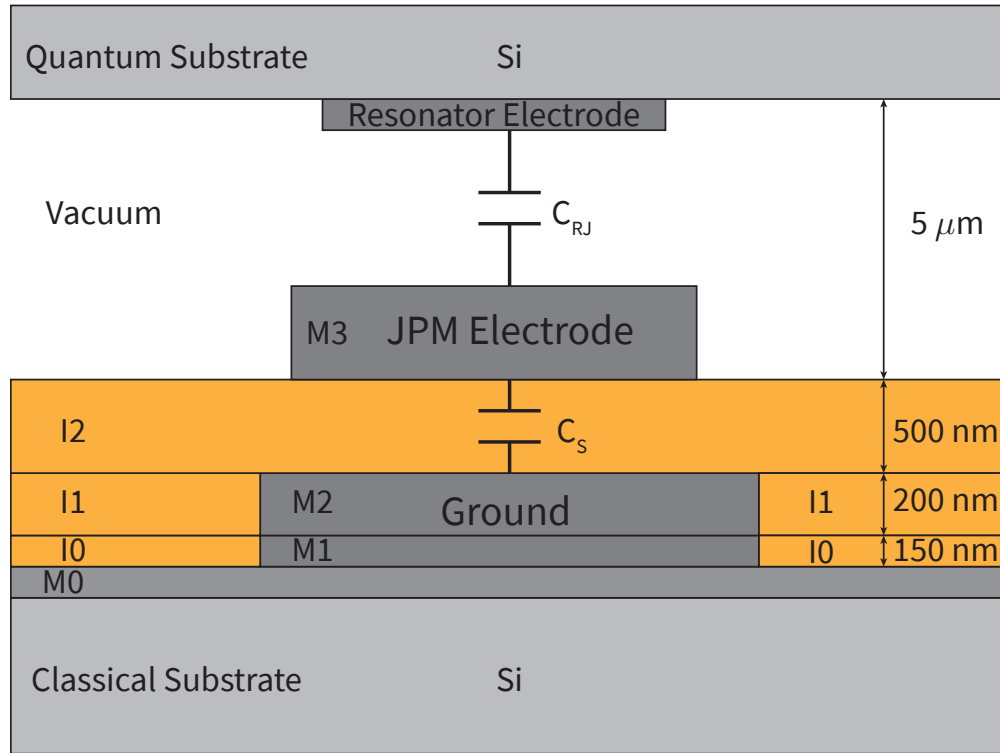
Figure 5.5: JPM MCM Capacitance Stack. The shunt capacitance for the JPM is formed using I2 as a dielectric. The coupling capacitance between the readout resonator and JPM is formed from this same electrode through the vacuum gap to the electrode on the resonator on the top chip.

$180\,\mu\mathrm{m} \times 180\,\mu\mathrm{m}$ capacitor pad in the M3 layer that couples with $35\,\mathrm{fF}$ to the $140\,\mu\mathrm{m} \times 140\,\mu\mathrm{m}$ capacitor pad on the readout resonator of the top chip, and couples with $3\,\mathrm{pF}$ to the ground plane M0. This coupling stack is illustrated in Figure 5.5.

The coupling of the reflection port that allows for microwave spectroscopy is given by $1/Q_c = 2R_0 Z_0 \omega_0^2 C_{RO}^2$, where R_0 is the impedance of the JPM circuit and Z_0 is the impedance of the coupled port, which is taken to be $50\,\mathrm{Ohm}$ [38]. A critical coupling is targeted, such that $Q_i = Q_c$. This results in a $55\,\mathrm{fF}$ capacitor to couple to the reflectometry port. The entire capacitor network was simulated in ANSYS Q3D to verify the capacitances.

A gradiometer inductor is used for the JPM shunt inductor. Although flux noise is not expected to be a significant issue, a gradiometer is still natural as the two coils allow for two separate mutual couplings, one for the bias line and one for the comparator, with minimal cross talk. The inductor
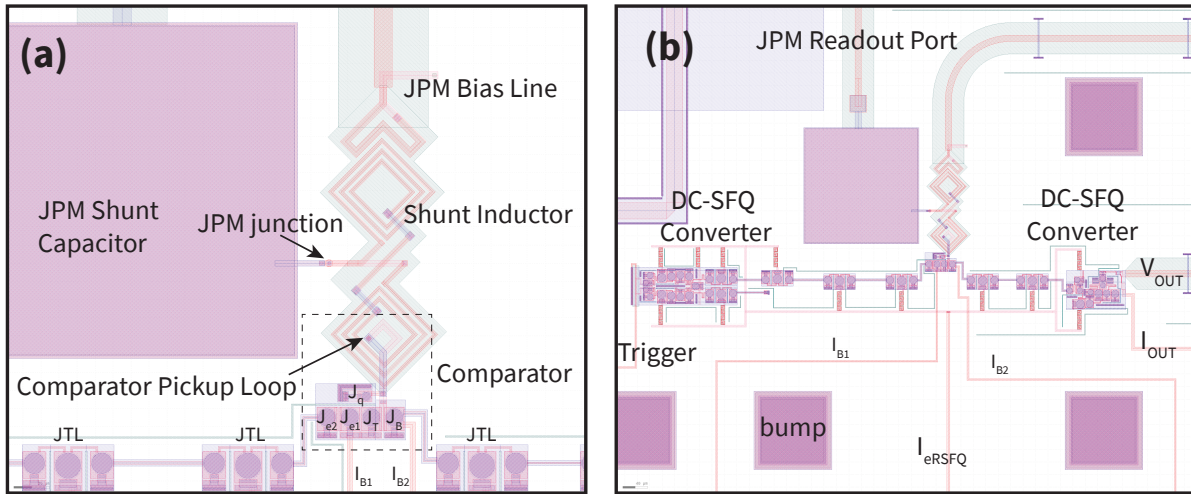
Figure 5.6: (a) Close up of the JPM and comparator. (b) Full-circuit view of the SFQ circuitry. From left to right: DC-SFQ Converter, JTL, Comparator, 2 JTLs, SFQ-DC Converter.

and mutual inductances were simulated and optimized in InductEx to achieve the correct values.

The design parameters of the JPM are listed in Table 5.2.

Parameter	Symbol	Value	Method of Determination
Shunt Capacitance	C_s	3 pF	Q3D
Shunt Inductance	L_s	1 nH	Inductex
Junction Critical Current	I_0	1 μA	Design Rules
Inductance Parameter	β_L	3	L_S/L_J
JPM-Cavity Swap Time	τ_{swap}	5 ns	
Cavity-JPM Coupling	$g_{RJ}/2\pi$	50 MHz	Eq. 5.9
Cavity-JPM Capacitance	C_{RJ}	35 fF	Q3D
Max Frequency	$\omega_0/2\pi$	6 GHz	$\omega_0 = 1/\sqrt{L_{S||J}C_S}$
Quality Factor	Q_{JPM}	300	SiOx loss given by SeeQC
Bias Mutual Inductance	M_B	15 pH	Inductex
Reflection Capacitance	C_{RO}	55 fF	Q3D

Table 5.2: Target design parameters for an MCM-based JPM device.

The device was fabricated at SeeQC, and many test chips were sent to Syracuse for testing.

5.3 Experiment

The results in the rest of this chapter are from experiments with only the classical carrier chip. The quantum flip chip was designed but never fabricated, and was not necessary in order to characterize the JPM or comparator.

A sample device, denoted S17, was wired into an Adiabatic-Demagnetization Refrigerator (ADR) at Syracuse for testing at millikelvin temperatures. A full wiring diagram is shown in Figure 5.7.
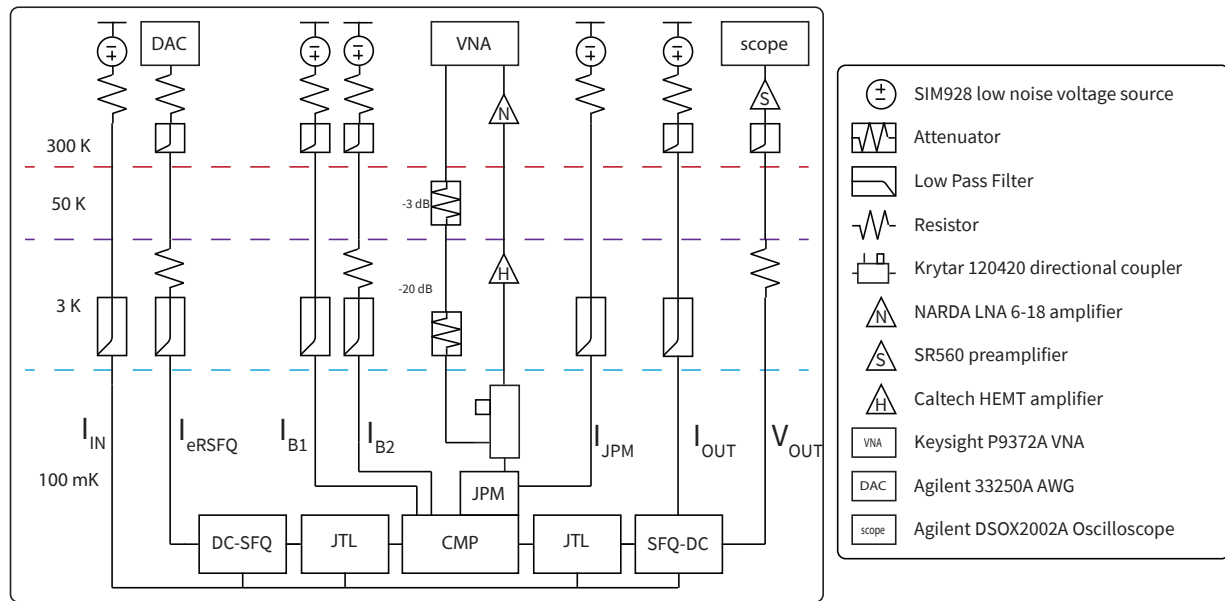
Figure 5.7: Wiring Diagram for testing of JPM-SFQ device.

There are 4 current bias lines for the SFQ circuitry. I_{eRSFQ} is the eRSFQ bias line which biases the input and output converters, as well as each of the JTLs used to connect cells. The SFQ-DC converter requires a bias denoted I_{OUT}. Lastly are the two comparator biases I_{C1} and I_{C2}. Each of these current biases was generated by connecting an SRS SIM928 battery powered low-noise voltage source through a large series resistance, typically between 5-100 k Ω, depending on the current resolution needed. These lines are additionally low-pass filtered with 80 MHz filters at 3 K. Several of the lines also had RC low-pass filters at room temperature, with cut-off frequencies of 10 Hz.

The current used to trigger the DC-SFQ converter was supplied by connecting an Agilent 33250 AWG through a series resistor. The voltage output of the SFQ-DC converter was amplified by an SRS SR560 low-noise preamplifier at room temperature before being acquired by an Agilent DSOX-2002A oscilloscope.

The JPM was biased using an identical setup as those described for the SFQ components. A Keysight P9372A VNA was used to perform reflectometry of the JPM. Port 1 was coupled to the $-20\,\mathrm{dB}$ coupled port of a directional coupler. The input port was coupled to the JPM, and the output was connected to a Caltech HEMT amplifier at $3\,\mathrm{K}$ and amplified further by a NARDA low-noise amplifier at room temperature before connecting to Port 2 of the VNA.

The JPM was calibrated separately from the comparator with the bias line and reflectometry port. Performing spectroscopy while sweeping the flux bias forward and backwards allowed for a full parameter extraction of the JPM circuit (see Figure 5.8).

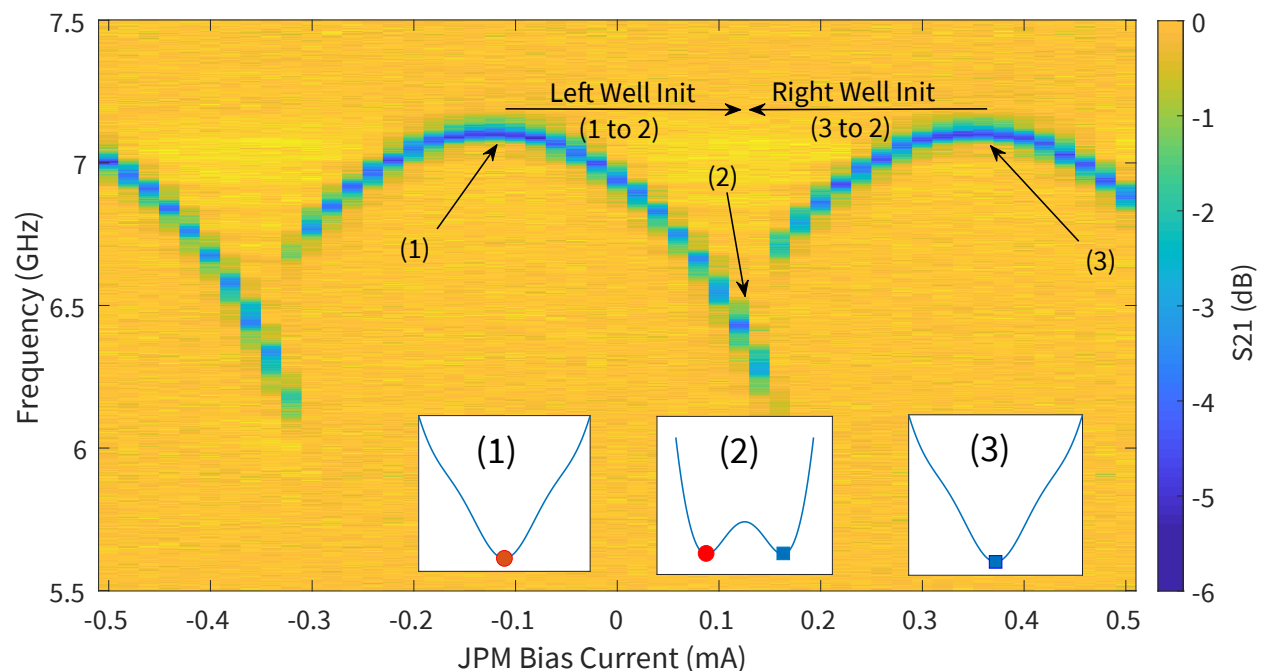Figure 5.8: JPM State Preparation. The normalized S11 of the JPM as bias current is swept in the positive direction. Critical bias points are highlighted. The JPM is prepared into its 'left well' by initializing into a single deep well at point (1) and then biasing to point (2). The 'right well' is prepared by initializing into point (3) and then sweeping in the negative direction to point (2).

Parameter	Measured Value	Method of Determination
I_c	1.15 μA	Extrapolated from wafer test junctions
β_L	4.2	Fitting JPM Flux scan
L_s	1.2 nH	$L_S = \beta_L L_J$
C_s	2 pF	$\omega_0 = 1/\sqrt{L_{S||J}C_S}$ at maximum frequency.
Q_i, Q_c	300, 300	Fits to S_{21} at maximum frequency

Table 5.3: Extracted JPM Parameters on device S17.

SeeQC reported that the critical current density of the junction fabrication process was $\sim$ 15% higher than designed (variation of this magnitude is to be expected). This implies a JPM critical current of 1.15 μA. We can solve for β_L by using the potential energy in Equation 3.18 along with the maximum frequency of the JPM and the frequency where the forward and reverse flux scans cross (forward flux scan shown in Figure 5.8). Fitting this curve results in a β_L of 4.2, and therefore the shunt inductance is 1.2 nH. The shunt capacitance can then be found by solving for the plasma frequency at the maximum JPM frequency. This leads to an estimated shunt capacitance of 2.2 pF.

The discrepancies between measured and designed values for the shunt capacitor (2.2 pF rather than 3 pF) and inductor (1.2 nH rather than 1 nH) could be due to many reasons. For the capacitor, the dielectric constant or thickness could be off from the values in the design rules. Also, the simulations assumed the presence of the top chip of the MCM and coupling to the readout resonator, both of which would increase the shunt capacitance to ground. The inductor was also simulated expecting the ground plane of a top chip, and this would bring down the self inductance of the gradiometer loop. These measured values are given Table 5.3. Despite these discrepancies, the JPM is still usable for these experiments. With the JPM fully characterized, the appropriate flux biasing could be performed to prepare the JPM in a single deep potential well, or either left or right potential wells (see the caption of Fig. 5.8).

The SFQ circuitry could be measured independently from the JPM. The measurement was performed as follows: first, the current biases were all set to zero in order to reset the circuit, and then set to their appropriate values. The JPM was also prepared into its desired state at this step. The

DAC was programmed with the appropriate trigger pulse, and the pulse was repeated a number of times, typically 50. The output of the DAC triggered acquisition by the scope, which acquired the amplified voltage output of the SFQ-DC converter. Rising or falling edges were counted, and divided by the number of applied triggers to calculate a switching probability. This sequence was then repeated so that 100 total triggers were applied in order to have resolution at the level of 1%.

The operating margins of the comparator circuit, which is the range over which a parameter can be deviated without breaking the functionality of the circuit, were measured in liquid He at SeeQC, and on an ADR at Syracuse at both $3\,\mathrm{K}$ and $100\,\mathrm{mK}$. The measurements at SeeQC were performed with an OCTOPUX, an instrument specifically developed to measure superconducting digital circuits [93]. Average results of 12 devices measured at SeeQC are given in Table 5.4. These margins are reasonable, though probably not optimal, as the comparator biases were arbitrarily selected from a working range.

Parameter	Center	S17 Margins	Avg. Device
I_{IN} (mA)	0.6	10%	23 %
I_{ERSFQ} (mA)	2	15%	11.8 %
I_{OUT} (µA)	52	25%	30 %

Table 5.4: Margins of Comparator S17 at $100\,\mathrm{mK}$.

With the SFQ circuitry calibrated, the behavior of the comparator could be observed. Switching curves were produced by sweeping I_{B1} and I_{B2} and fitting the switching probabilities to the error function given in Equation 5.1. These experiments were performed with the JPM in both left and right potential wells. These results are shown in Figure 5.9. An example slice of this data along a constant I_{B2} is shown in Figure 5.10.
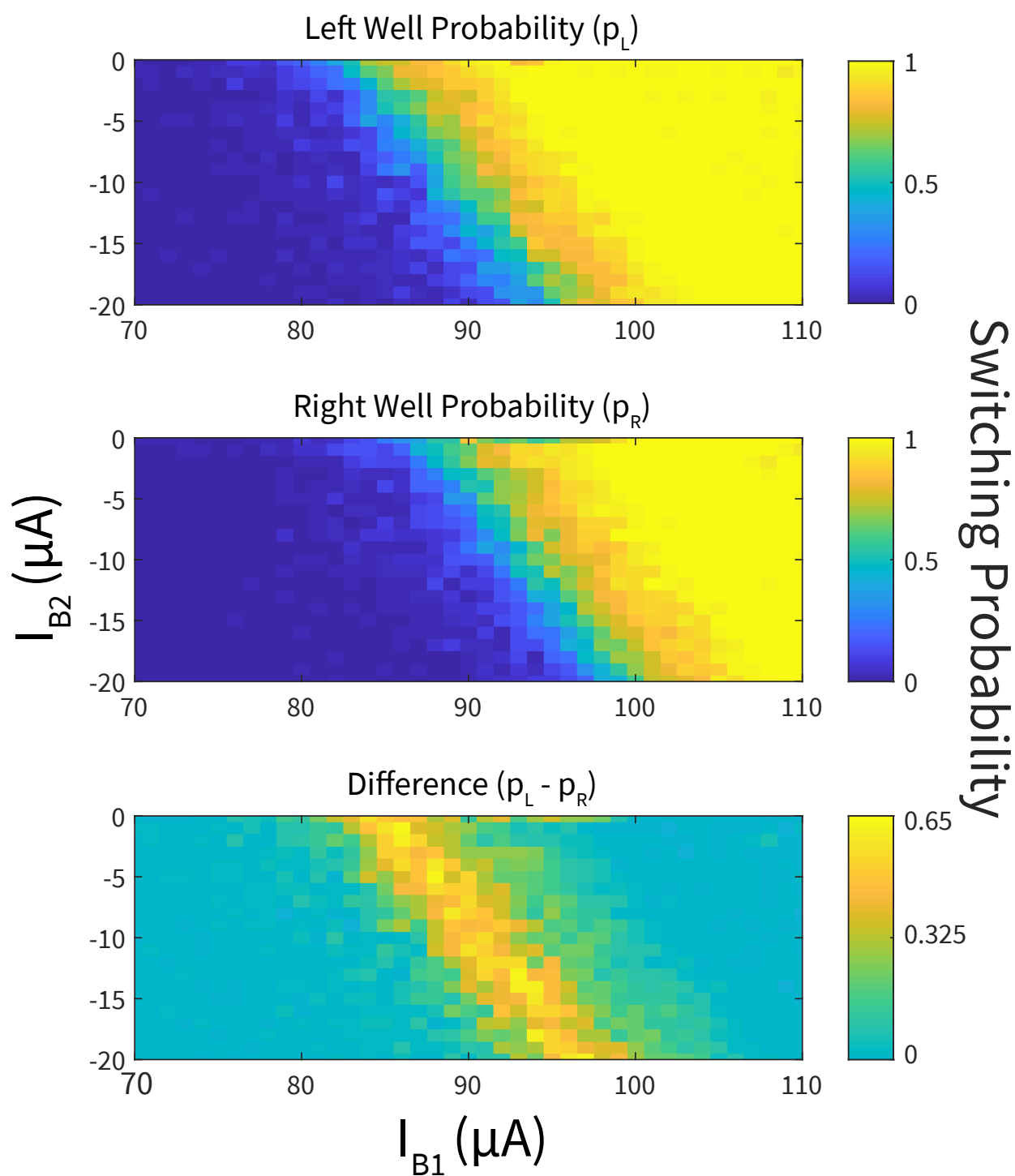
Figure 5.9: Switching probabilities for both JPM states. (Top) JPM prepared in left well. (Middle) JPM prepared in right Well. (Bottom) Difference between two switching probabilities.
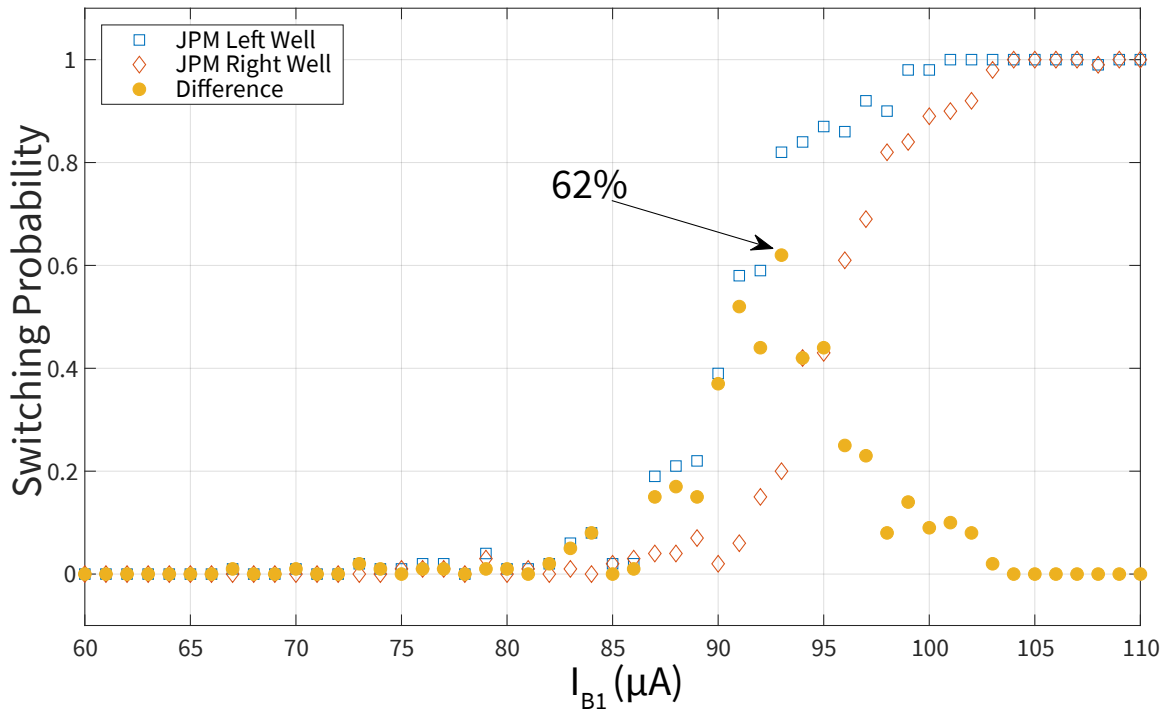
Figure 5.10: Switching curves for both JPM states. The maximum difference between the two switching probabilities is 62%.

5.3.1   Discussion

The switching curve along either a constant I_{B1} or constant I_{B2} is remarkably stable over a wide range of values, which was unexpected given the theory that the gray zone width is dependent on the initial phase of the comparator junctions set by I_{B1} [86]. Additionally, the gray zone width is roughly $100\times$ larger than expected. It is unclear what is responsible for this, but there are a few possibilities. First, SFQ circuits are notoriously sensitive to magnetic fields. Typical measurement setups utilize multiple layers of magnetic shielding cans with high aspect ratios. For the experiments that took place in an ADR at SU, the magnetic shielding can was very sub-optimal, and this was also noticed on unrelated qubit experiments. Thermal cycling of the device above the T_c of niobium and back down to millikelvin could sometimes have a drastic effect on the device performance. This implies that the random distribution of flux trapped in the film as it went superconducting was coupling into the device. Seeing as the comparator is intentionally a flux sensitive device, it is

reasonable that poor magnetic shielding would negatively impact its performance.

Additionally, the device was very sensitive to electrical noise picked up from room temperature instruments. Typical SFQ devices are measured with a device such as the previously mentioned OCTOPUX [93], where the return path of all currents are clearly defined and electrically isolated. These experiments also take place in liquid helium dewars in closed Faraday-shielded rooms, ensuring maximum isolation. The devices measured at SU could not be electrically isolated from the cryostat, as the samples were grounded to their sample boxes which were electrically connected to the cold finger of the ADR in order to cool the device. Connecting all of the instruments shown in Figure 5.7 to a common wall outlet, and tying the cryostat to the building ground were both necessary in order to see repeatable device performance. Placing very low cutoff frequency low-pass filters on the current and voltage lines of the SFQ-DC converter was also necessary.

Despite these issues, the JPM state was still distinguishable with a fidelity of 62%. Since the comparator can be interrogated at a high speed, it should be possible to apply many triggers and average the results at room temperature within a single measurement cycle, which would increase fidelity considerably. The following improvements are suggested for following experiments. First, the device should be designed so as to attempt to mitigate the effects of stray flux. Second, increasing the critical current of the JPM while keeping the coupling constant would couple even more flux into the comparator. Most critically, the cryogenic environment should be tailored to more closely resemble traditional SFQ experiments, including improved magnetic shielding and electrical isolation.

Chapter 6

Future work: The Quantum-Classical Interface

The preceding chapters have demonstrated the experimental feasibility of digital control and digital readout of superconducting qubits. When combined, these elements allow for a nearly fully digital interaction with a superconducting qubit. Here I will discuss an overall architecture envisioned for future development of these technologies. Reference [77] is used heavily in this chapter, and provides an excellent foundation for many of these ideas.
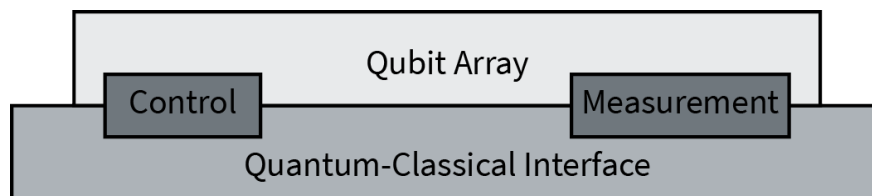

Figure 6.1: Quantum-Classical Interface - Device Level. A classical chip containing interface devices such as the SFQ drivers and JPM-comparator circuits described in previous chapters. This chip is bump bonded to a qubit chip in an MCM device.

A full interface consists of both control and measurement interfaces between the quantum device and further classical processing. This classical processing could consist of superconducting logic such as Reciprocal-Quantum-Logic (RQL) [29], Adiabatic Quantum-Flux-Parametrons, (AQFP) [94], or the SFQ technology discussed in this work. Cryogenic CMOS (cryoCMOS) could also be utilized [95], and has already been demonstrated in controlling superconducting qubits [96]. Here, it is assumed that this classical co-processor will utilize the same SFQ technology as used in the interface layer.
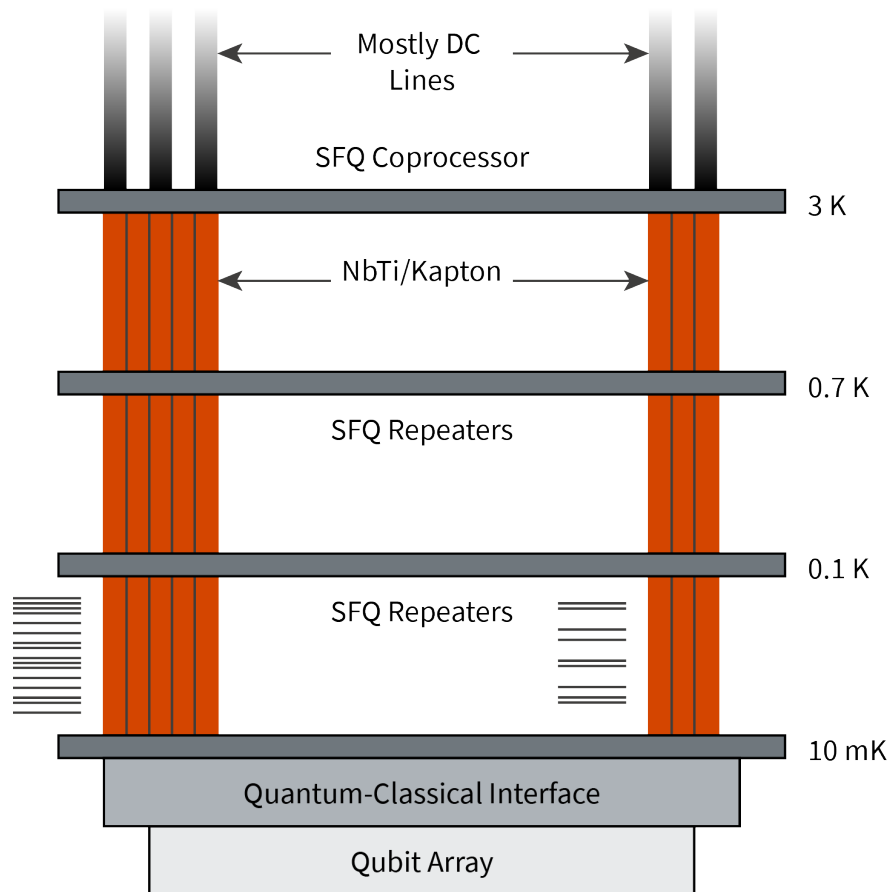
Figure 6.2: Quantum-Classical Interface - Fridge level. Signals from room temperature consist of mostly dc signals. An SFQ based co-processor at $3\,\mathrm{K}$ distributes qubit control signals consisting of digital patterns. These patterns are transmitted to millikelvin over NbTi-on-Kapton flex cables, with SFQ repeaters at intermediate temperature stages. At base temperature, the classical interface chip routes the control signals and performs measurements. These measurement results are transmitted back up to the co-processor, closing the feedback loop. (Adapted from [77].)

A fridge-level overview of this architecture is shown in Figure 6.2. Rather than large numbers of coaxial rf lines running from room temperature, through the various cryostat stages to the device, mostly dc lines are connected from room temperature to a classical co-processor positioned at $3\,\mathrm{K}$. It is advantageous to have as much of the classical circuitry at $3\,\mathrm{K}$ as possible. It is unnecessary for decision making elements, clocks, and memory elements to be at millikelvin, and most of these elements have already been designed and fabricated in other applications for operation at liquid helium temperatures.

To transmit control signals and measurement results from the classical co-processor to the inter-
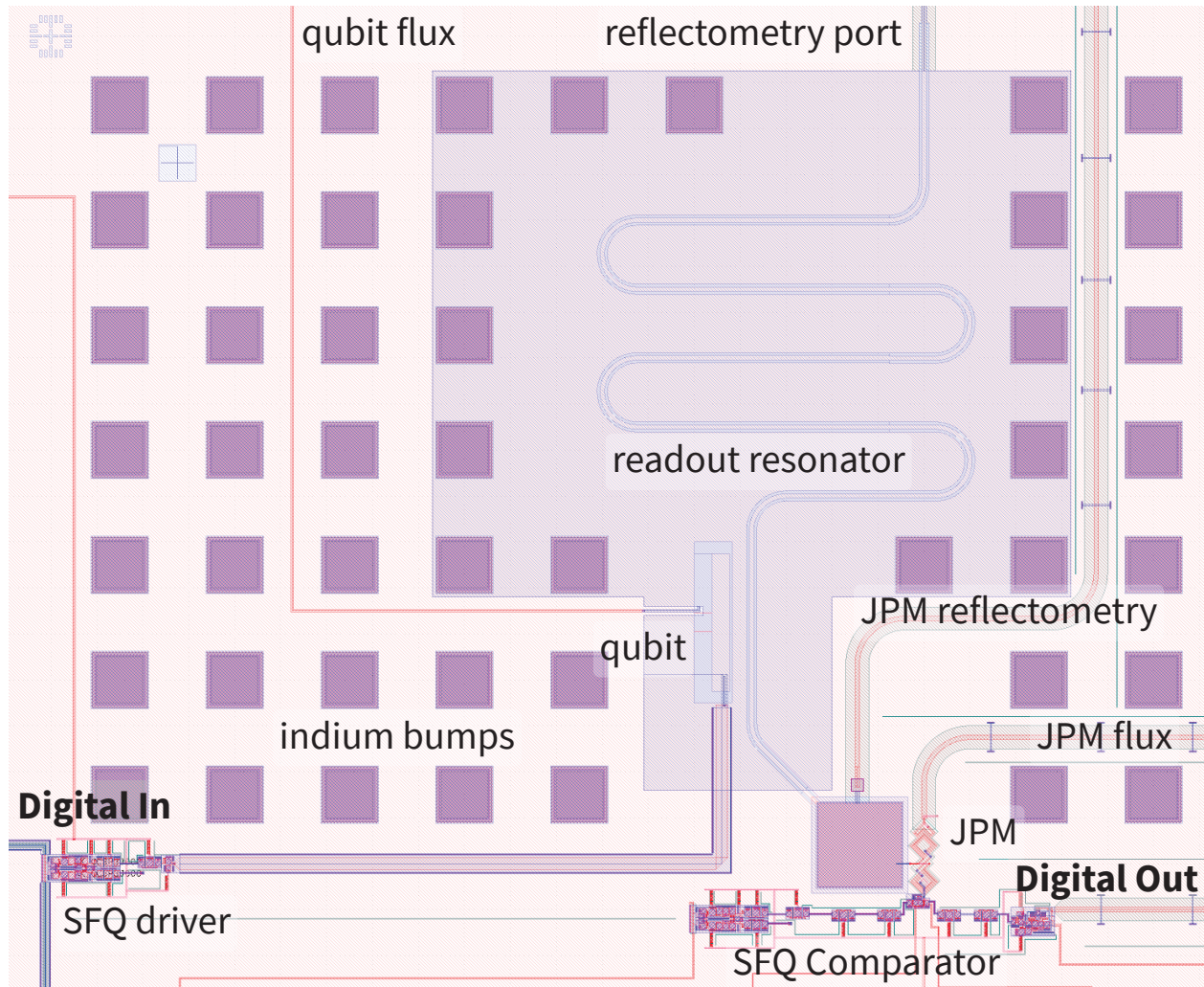
Figure 6.3: Device designed with full quantum-classical interface. The qubit and readout resonator are fabricated on the top chip. SFQ driver, JPM-SFQ comparator, and all relevant bias lines and ports for reflectometry measurements are fabricated on the bottom chip. Large indium bumps bond the two chips together at a nominal $5\,\mu\text{m}$ spacing.

face layer, novel transmission lines need to be developed. For qubit counts in the millions, it is natural to anticipate needing a similar order of magnitude in lines for control and measurement. This many traditional coaxial cables are simply impractical at this number. The physical size of the cables and their connectors become a limiting factor, but most importantly, the thermal conductivity of the cables would result in essentially a thermal short between the millikelvin and $3\,\text{K}$ temperature stages.

Rather than coaxial lines, NbTi microstrip lines on Kapton tape could allow for communication be-

tween the two temperature stages with minimal thermal conductivity. NbTi has very low thermal conductivity, and with 50 μm wide microstrip lines, the estimated thermal load is on order 40 μW. The heat load of the needed Kapton is higher, at 220 μW for 0.5 mil thick tape, 1 m long, and wide enough for the lines with a 50 μm spacing. This heat-load is still roughly an order of magnitude larger than the cooling power of commercially available dilution refrigerators at the moment, but it is reasonable to assume that future generations utilizing multiple dilution units could sufficiently manage this load. These flexible cables have been demonstrated at microwave frequencies [97], although they have not been tested to deliver SFQ pulses. Developing these cables along with the necessary intermediate repeaters would likely require a significant research effort, but would allow for an enormous increase in wiring density within a cryostat.

The device measured in Chapter 5 was designed with a full interface in mind. It is capable of bonding to a quantum chip, and has the relevant control and readout circuitry. Qubit chips fabricated in the future can be bonded to these chips, so that the digital control and readout can be performed in a single experiment. This full layout is shown in Figure 6.3.

6.1   Conclusions

Throughout this work I have discussed significant progress towards interfacing superconducting qubits with SFQ digital logic. In Chapter 1 I designed a qubit geometry for use in the following experiments. This rectmon qubit was frequency tunable and had coherence times that were acceptably long for the various experiments performed.

In Chapter 2, results were presented demonstrating control of one of these qubits with SFQ pulses, with an average gate fidelity of 95%. This was a significant proof-of-principle demonstration of digital qubit control.

In Chapter 3, I presented results of qubit measurement with a Josephson Photomultiplier, a novel element that avoids the need for cryogenic circulators or quantum-limited amplifiers. Single-shot

measurement fidelities of 92% were achieved, and improved devices are already in development.

In Chapter 4, a method was proposed for encoding the result of a JPM measurement into an SFQ pulse by coupling the JPM to a pair of ballistic JTLs. The delay induced by the circulating current states of the JPM allow for a delay detection circuit to discriminate the JPM states.

Chapter 5 outlined an alternative method, consisting of directly probing the JPM circulating current with an SFQ flux comparator. A device was designed, fabricated, and experimentally verified with single-shot readout fidelities of $\sim 65\%$.

Finally, in this chapter I suggested future steps for this architecture. These results are extremely encouraging, and the future looks very bright. I look forward to continuing this work in the future.

Appendices

Appendix 1

Qubit Fabrication Recipes

For the device in Section 3 and Ref. [11], a very simple qubit fabrication method was used.

The transmon qubit and readout cavity are fabricated on a high-resistivity Si substrate.

1. **Ground Plane Deposition**

   A $90\,\text{nm}$ Nb film is deposited using at Syracuse University using a magnetron sputter system.

   ☐ Load substrate in load-lock and pump with turbo pump

   ☐ Close gate valve and open load-lock valve.

   ☐ Use loading arm to load substrate into holder.

   ☐ Close load-lock valve

   ☐ Open gate valve and pump to $< 1 \times 10^{-7}\,\text{Torr}$.

   ☐ Adjust stage to position substrate within of the closest distance to the target

   ☐ Open valve to flow 60 sccms of Argon into the chamber. Throttle the chamber pressure $6.5 \times 10^{-3}\,\text{Torr}$ by adjusting the gate valve

   ☐ Turn on the power supply for the sputtering gun, and ensure the power is set to $250\,\text{W}$.

☐ Pre-sputter the target with the shutter closed for 2-5 minutes.

☐ Open the shutter to allow deposition onto the substrate. 70 seconds on the instrument clock corresponds to roughly 110 nm of Nb.

☐ Turn off the power supply

☐ Raise the substrate back to the loading arm position

☐ Retrieve the substrate with the loading arm

☐ Close load-lock valve

☐ Vent load-lock with N_2 and retrieve sample

☐ Return load-lock to vacuum

2. **Ground Plane Patterning**

A single photolithography step at CNF defines all features, except for the Josephson junctions.

☐ Spin **DS-K101**[1] at 5000 rpm for 60 s. Ramp at 10 000 rpm/s

☐ Bake at 185 °C for 90 s

☐ Spin **UV-210-0.6**[2] at 3000 rpm for 60 seconds. Ramp at 8000 rpm/s

☐ Bake at 135 °C for 60 s

☐ Expose on ASML 300C DUV Stepper

 – **Energy** 25 mJ/cm^2

 – **Focus Offset** -0.2 μm

 – **Numerical Aperture** 0.63

---

[1] `https://www.nanotech.ucsb.edu/wiki/images/a/af/DS-K101-304-Anti-Reflective-Coating.pdf`

[2] `https://kayakuam.com/wp-content/uploads/2019/10/UV210GS.pdf`

- **Sigma - outer** 0.75

☐ Bake at 135 °C for 90 s

☐ Develop for 90 s in MIF-726 in Hamatech HMx900.

3. **Ground Plane Etch**

The ground plane is etched with a Chlorine based etch in a PlasmaTherm 720/740 RIE Etcher.

(a) **Chamber Conditioning** Run the below recipe for 20 min

(b) **Gas stabilization** $BCL_3/Ar/Cl_2$ at 20/20/10 SCCM for 30 s at 30 mTorr

(c) **Light Etch** 300 W DC for 30 s at 30 mTorr

(d) **Main Etch** 300 W DC for 7.5 min at 20 mTorr

4. **Ground Plane Clean**

Strip off all resist and prepare the wafer for e-beam writing

(a) Run wafer through hot strip bath for 10 min

(b) Transfer into second hot strip bath for 10 min

(c) Rinse with DI water for 5 min

(d) Spin dry

(e) Strip remaining resist residue with an RIE Oxygen plasma etch in the Glen 1000

5. **Qubit Junction Patterning**

Junction electrodes and air-bridges are defined in a bilayer on the JEOL JBX 9500FS direct write ebeam lithography system.

(a) Spin MMA (methyl methacrylate) in 11% ethyl lactate [3] at **2300 rpm**. Ramp at **1000 rpm/s**. Results in a **600 nm** film.

(b) Bake at **170 °C** for **10 minutes**.

(c) Spin PMMA (polymethyl methacrylate) in 2% anisole [3] at **2500 rpm**. Ramp at **1000 rpm/s**. Results in **70 nm** film.

6. **Qubit Junction Deposition**

Qubit junctions are deposited in an Aluminum Evaporator in the Plourde Research Lab at Syracuse University.

(a) **Develop**

After writing on the JEOL, the wafer is kept undeveloped until chips are ready for oxidation. Depositing junctions as soon as possible after development is ideal for having a clean substrate-junction interface.

☐ Prepare **20 mL** of 3:1 IPA:MIBK

☐ Immerse and agitate sample in solution for **70 s**

☐ Rinse with IPA for **10 s**

☐ Blow dry with N_2

☐ Inspect patterns with microscope, checking for presence of air-bridge

(b) **Load and pump**

☐ Load into evaporator with junctions perpendicular to the axis of rotation.

☐ Pump load lock with turbo for 20 minutes.

---

[3]`https://kayakuam.com/wp-content/uploads/2019/09/PMMA_Data_Sheet.pdf`

☐ Close off turbo pump, and open gate valve to cryopump.

☐ Pump to to $< 1 \times 10^{-7}$ Torr

(c) **Ion Mill**

Ion milling helps to remove any residue that could be present on the exposed substrate

☐ Close Oxygen ballast to prevent Argon from entering

☐ Open Ar valve until pressure sensor IG2 reads 2.8×10^{-4} Torr

☐ Turn on Ion Mill source, and then discharge

☐ Rotate substrate to face mill for $13\,\text{s}$

☐ Rotate susbtrate to face away from mill

☐ Turn off Ion Mill discharge, and then source

☐ Close Ar valve

(d) **Deposit Bottom Electrode**

☐ Turn on cooling water for electron beam gun

☐ Turn on gun source

☐ Increase beam current manually to 5% and use view window to align beam to center of Al crucible

☐ Close view window

☐ Increase beam current to 20% for $1\,\text{min}$

☐ Increase beam current to 40% for $1\,\text{min}$

☐ Increase beam current until deposition rate is

☐ Rotate substrate stage to $-11°$

☐ Pre-evaporate at least **100 nm** of Al

☐ Open shutter and zero deposition meter

☐ Close shutter when desired thickness has been deposited (Normally **40 nm**)

☐ Turn beam current to 0%.

(e) **Oxidation**

☐ Close gate valve

☐ Open $Ar - O_2$ needle valve to prime ballast with oxygen. Pressure in closed ballast will be roughly 13x lower when opened to top chamber

☐ Close $Ar - O_2$ needle valve

☐ Open ballast and start timer for desired oxidation time

☐ Increase pressure if needed by adjusting needle valve

☐ Evacuate chamber with turbo pump once oxidation time has expired

☐ Close turbo once it reaches top speed

☐ Open gate valve

(f) **Deposit Top Electrode**

☐ Ramp beam current back to target deposition rate

☐ Rotate substrate stage to 12°

☐ Open shutter and zero deposition meter

☐ Close shutter when desired thickness has been deposited (Normally **60 nm**)

☐ Turn beam current to 0%.

(g) **Unload**

☐ Turn off gun source

☐ Turn off cooling water for electron beam gun

☐ Close gate valve

☐ Vent upper chamber with N_2

☐ Once at atmospheric pressure, close N_2 and remove sample

☐ Immediately pump upper chamber with turbo for **20 min**

☐ Open gate valve to cryopump

7. **Lift-off**

After aluminum evaporation, the Al film is removed in a lift-off process, leaving junctions only where they were defined with e-beam lithography

☐ Heat a small beaker of DCM (Dichloromethane) to **50 °C**.

☐ Place samples in beaker and cover with aluminum foil to help prevent evaporation. If the DCM is left to evaporate, the residue left on a chip can be impossible to remove.

☐ After 10 minutes or so, agitate the sample to encourage the aluminum film to start to detach from the chip. Do not peel the aluminum off.

☐ After 30 total minutes in DCM, the resist should have dissolved and the film should be removed from the chip.

☐ Transfer the device into a clean beaker of DCM (keeping the surface wet).

☐ Sonicate the beaker on low by just dipping the beaker into the water for a moment.

  Repeat 3-4 times.

 ☐ Transfer into acetone and rinse.

 ☐ Transfer into IPA and rinse.

 ☐ Rinse with DI water.

 ☐ Blow dry with N_2.

The junctions integrated into qubits cannot and should not be directly probed. However, each device in this work was fabricated with several 'witness' or 'test' junctions fabricated on the periphery of the chip. These junctions are used to debug the fabrication process and to anticipate whether a device will work as expected. Typically, three-wire resistance measurements are performed with a lock-in amplifier and $100\,\mathrm{nm}$ of source current in order to extract a mean resistance for a given junction area, which can then be correlated with a critical current by Eq. 1.17. Electrostatic discharge (ESD) is important to monitor when probing junctions with small critical currents, as even small static 'shocks' are enough to send a fatal amount of curren through a junction.

Appendix 2

SFQ Recipes

The SFQ chips for both the SFQ control experiment and JPM-SFQ readout experiment were fabricated by HYPRES (now SeeQC) in Elmsford, NY. The fabrication stack (taken from the design rules[1]) is given in 2.1.

---

[1] `https://seeqc.com`

#	Layer Name	Description	Thickness (nm)
1	M0	Nb deposition M0 patterning (holes in Nb ground plane)	100
2	I0	SiO2 deposition Via between M1 and M0	150
3	J1	Nb/Al/AlOx/Nb trilayer patterning Counter-electrode (junction area)	50
4	A1	Base electrode anodization Anodization layer patterning	40
5	M1	Trilayer base electrode patterning	135
6	R2	SiO2 deposition Ti/PdAu/Ti deposition Resistive layer patterning	100 100
7	I1	SiO2 deposition Via between M2 and (J1, R2, or M1)	100
8	M2	Nb Deposition M2 layer patterning	300
9	I2	SiO2 deposition Via between M2 and M3	500
10	M3	Nb deposition M3 layer patterning	600
11	R3	Pd/Au contact metallization deposition Contact pad patterning	350
12	BMP	Cu/NbN/In layer for MCM	5000

Table 2.1: SeeQC layer stackup

Material	Relevant Parameter	Value
Niobium	Penetration Depth	90 nm
Ti/PdAu/Ti	Sheet Resistance	2 $\Omega/\square$
SiOx	Loss Tangent (Q)	3e-3 (300)
	Dielectric Constant	4.5

Table 2.2: SeeQC Film Parameters

Appendix 3

Lab Control Software

When trying to maximize experimental throughput, it becomes very useful to be able to monitor and control the various cryostats in the lab remotely. To this end, a modern web app was developed to allow for this remote control and monitoring. Creatively named 'Lab Control', it has been the primary interface for the cryostats in the Plourde Research Lab for the past several years. Although I recommend its immediate replacement with something more modern and supported (i.e. Logger [1]), I'm including some notes on the software for the reference of those in the lab who will need to debut it in the future.

The software can generally be thought of as a finite state machine. At any given point in time, each fridge has a defined state. That state is stored in a document in a database. Every time step (5 seconds for most fridges), the state is updated and a new document is appended to the database. A separate 'control' document exists in the database as well. The clients interfacing with the web app can control the fridges by writing commands to this document. The driver running on the fridge computers check this document at each time step, and perform whatever steps are relevant. Using the database to mediate interaction precludes the need for a direct connection from clients on the internet to the fridge computers. It also means that the fridge computer can stop and resume easily, as it resumes at it last known state.

[1] `http://logger.labber.org/`

3.1   Fridge Drivers

Each fridge computer runs a python driver. This driver simply polls all of the given instruments at each time step, creates a document with each of the parameters, and sends it to the remote database. Instruments and the commands to query them are stored in a 'settings.json' JSON file. This file is human readable and can be easily edited to account for changes of instruments or changing instrument addresses without needed to directly edit code.

For the ADRs, the driver also controls the magnet power supply and the heat switch. These two controls are needed to perform a full magnet cycle and cool the fridge to base temperature. The control commands are Magup, Magdown, and None.

When the Magup command is active, the magnet power supply is incremented at each time step by some step value, until the magnet voltage reaches some maximum value. These values are given in the 'settings.json' file. At the end of the Magup cycle, the heat switch is opened and closed to relieve stress on the salt pill supports.

When the 'Magdown' command is active, the magnet power supply opens the heat switch if it is closed, and then decrements the magnet voltage until it reaches 0. Critically, the voltages written to the magnet power supply are determined by querying the power supply's current voltage and adding or subtracting a small value. This prevents the code from accidentally taking a large step that causes the magnet to quench, or damages the power supply.

3.2   Server

The server is a simple Node.js[2] application, running an Express[3] back-end. The application is written in Javascript and is only a couple hundred lines long. The bulk of the server is just routing the client

---

[2]`https://nodejs.org/en/about/`
[3]`http://expressjs.com/`

to the relevant HTML files. The server also connects to the database, and pulls data to give to the client's web browser. Upon loading a fridge view, the last 10 minutes of data is queried and returned for display. While the view is active, the data is updated every 5 seconds for real time monitoring.

For the ADRs, the server also receives commands given by the client. Clicking the 'Magup' or 'Mag-down' buttons for the ADRs tells the server to write the relevant commands to the control document in the database.

For security reasons, the web app is insulated behind the Syracuse University firewall and is only accessible from SU IP addresses.

3.3   Front End

The front end (what is shown in your browser when navigating to the web page) is written in Angular.JS [4]. Angular is great for creating dynamic views within web applications without needing to write tons of HTML.

3.4   MongoDB Database

The hub for the entire Lab Control app is the database. MongoDB [5] was chosen for its simplicity, and the fact that it easily interfaces with the Express back-end, as well as the python fridge drivers. The document model is intuitive for storing the various states of the fridges. These documents map easily to Python dicts for the Fridge Drivers, and JSON-documents for the server. It is also free to use and widely adopted, making support easy to find online.

---

[4]`https://angularjs.org/`
[5]`https://www.mongodb.com/`

Altogether, the Lab Control is a simple an easily extendable app for managing the fridges in our lab. The main issues have been with keeping the code compatible with underlying python packages, since these packages are updated regularly on the fridge control computers. However, I still recommend migrating to a more modern and polished application, like Logger by Labber[6]. While it may not allow for fridges to be controlled from your phone while in bed on a Saturday morning, it should be much more robust and user-friendly.

---

[6]`http://labber.org/`

References

[1] Gordon E. Moore. *Cramming more components onto integrated circuits*. Tech. rep. 1. 1998, pp. 82–85. DOI: `10.1109/JPROC.1998.658762`. URL: `https://www.funkschau.de/uploads/media_uploads/documents/1429521922-13-gordonmoore1965article.pdf`.

[2] A. G. Fowler, Adam C. Whiteside, and Lloyd C L Hollenberg. "Towards practical classical processing for the surface code: Timing analysis". In: *Physical Review A - Atomic, Molecular, and Optical Physics* 86.4 (Oct. 2012). DOI: `10.1103/PhysRevA.86.042313`. URL: `http://arxiv.org/abs/1202.5602%20http://www.arxiv.org/pdf/1202.5602.pdf`.

[3] Peter W. Shor. *Polynomial-time algorithms for prime factorization and discrete logarithms on a quantum computer*. Tech. rep. 5. 1997, pp. 1484–1509. DOI: `10.1137/S0097539795293172`.

[4] Daniel J Bernstein, Nadia Heninger, Paul Lou, and Luke Valenta. *Post-quantum RSA*. Tech. rep. URL: `https://www.ams.org/profession/leaders/`.

[5] Iulia Buluta and Franco Nori. *Quantum simulators*. Tech. rep. 5949. 2009, pp. 108–111. DOI: `10.1126/science.1177838`. URL: `www.sciencemag.org`.

[6] Frank Arute, Kunal Arya, Ryan Babbush, Dave Bacon, Joseph C Bardin, Rami Barends, Rupak Biswas, Sergio Boixo, Fernando G S L Brandao, David A Buell, Brian Burkett, Yu Chen, Zijun Chen, Ben Chiaro, Roberto Collins, William Courtney, Andrew Dunsworth, Edward Farhi, Brooks Foxen, Austin Fowler, Craig Gidney, Marissa Giustina, Rob Graff, Keith Guerin, Steve Habegger, Matthew P Harrigan, Michael J Hartmann, Alan Ho, Markus Hoffmann, Trent Huang, Travis S Humble, Sergei V Isakov, Evan Jeffrey, Zhang Jiang, Dvir Kafri, Kostyantyn Kechedzhi,

Julian Kelly, Paul V Klimov, Sergey Knysh, Alexander Korotkov, Fedor Kostritsa, David Landhuis, Mike Lindmark, Erik Lucero, Dmitry Lyakh, Salvatore Mandrà, Jarrod R Mcclean, Matthew Mcewen, Anthony Megrant, Xiao Mi, Kristel Michielsen, Masoud Mohseni, Josh Mutus, Ofer Naaman, Matthew Neeley, Charles Neill, Murphy Yuezhen Niu, Eric Ostby, Andre Petukhov, John C Platt, Chris Quintana, Eleanor G Rieffel, Pedram Roushan, Nicholas C Rubin, Daniel Sank, Kevin J Satzinger, Vadim Smelyanskiy, Kevin J Sung, Matthew D Trevithick, Amit Vainsencher, Benjamin Villalonga, Theodore White, Z Jamie Yao, Ping Yeh, Adam Zalcman, Hartmut Neven, and John M Martinis. "Quantum supremacy using a programmable superconducting processor". In: *Nature* 574 (2019), p. 505. DOI: `10.1038/s41586-019-1666-5`. URL: `https://doi.org/10.1038/s41586-019-1666-5`.

[7]   IBM. *IBM Opens Quantum Computation Center in New York; Brings World's Largest Fleet of Quantum Computing Systems Online, Unveils New 53-Qubit Quantum System for Broad Use.* 2019.

[8]   Edwin Pednault, John A. Gunnels, Giacomo Nannicini, Lior Horesh, and Robert Wisnieff. *Leveraging Secondary Storage to Simulate Deep 54-qubit Sycamore Circuits.* Tech. rep. 2019. URL: `http://arxiv.org/abs/1910.09534`.

[9]   David P. DiVincenzo. "The physical implementation of quantum computation". In: *Fortschritte der Physik* 48.9-11 (Sept. 2000), pp. 771–783. DOI: `10.1002/1521-3978(200009)48:9/11<771::AID-PROP771>3.0.CO;2-E`. URL: `http://doi.wiley.com/10.1002/1521-3978%282000009%2948%3A9%2F11%3C771%3A%3AAID-PROP771%3E3.0.CO%3B2-E`.

[10]   E. Leonard, M. A. Beck, J. Nelson, B.G. Christensen, T. Thorbeck, C. Howington, A. Opremcak, I.V. Pechenezhskiy, K. Dodge, N.P. Dupuis, M.D. Hutchings, J. Ku, F. Schlenker, J. Suttle, C. Wilen, S. Zhu, M.G. G. Vavilov, B. L. T. Plourde, and R. McDermott. "Digital Coherent Control of a Superconducting Qubit". In: *Physical Review Applied* 11.1 (Jan. 2019), p. 014009. DOI: `10.1103/PhysRevApplied.11.014009`. URL: `https://link.aps.org/doi/10.1103/PhysRevApplied.11.014009`.

[11]   A. Opremcak, I.V. V. Pechenezhskiy, C. Howington, B.G. G. Christensen, M.A. A. Beck, E. Leonard,

J. Suttle, C. Wilen, K.N. N. Nesterov, G.J. J. Ribeill, T. Thorbeck, F. Schlenker, M.G. G. Vavilov, B. L. T. Plourde, and R. McDermott. "Measurement of a Superconducting Qubit with a Microwave Photon Counter". In: *Science* 361.6408 (2018), pp. 1239–1242. DOI: `10.1126/science.aat4625`. URL: `http://arxiv.org/abs/1803.01014%0Ahttp://dx.doi.org/10.1126/science.aat4625`.

[12] C. Howington, Alex Opremcak, Robert McDermott, Alex Kirichenko, Oleg A. Mukhanov, and B. L. T. Plourde. "Interfacing Superconducting Qubits with Cryogenic Logic: Readout". In: *IEEE Transactions on Applied Superconductivity* 29.5 (2019). DOI: `10.1109/TASC.2019.2908884`.

[13] H. K. Onnes. "Disappearance of the electrical resistance of mercury at helium temperatures". In: *Proceedings Koninklijke Akademie van Wetenschappen te Amsterdam* 14 (1911), pp. 113–115. DOI: `10.3138/B352-5468-3472-3172`.

[14] M K Wu, J R Ashburn, C J Torng, P H Hor, R L Meng, L Gao, Z J Huang, Y Q Wang, and C W Chu '. "Superconductivity at 93 K in a New Mixed-Phase Y-Ba-Cu-0 Compound System at Ambient Pressure". In: 58.9 (1987).

[15] D. A. Buck. "The Cryotron—A Superconductive Computer Component". In: *Proceedings of the IRE* 44.4 (1956), pp. 482–493. DOI: `10.1109/JRPROC.1956.274927`.

[16] R Gross, A Marx, and F Deppe. "Applied superconductivity: Josephson effect and superconducting electronics". In: (2016).

[17] Michael Tinkham. *Introduction to Superconductivity*. Dover Publications, 1996.

[18] B. D. Josephson. *Possible new effects in superconductive tunnelling*. Tech. rep. 7. 1962, pp. 251–253. DOI: `10.1016/0031-9163(62)91369-0`.

[19] Vinay Ambegaokar and Alexis Baratoff. "Tunneling Between Superconductors". In: *Physical Review Letters* 10.11 (1963). URL: `https://journals.aps.org/prl/pdf/10.1103/PhysRevLett.10.486`.

[20] Y. Nakamura, Yu A. Pashkin, and J. S. Tsai. "Coherent control of macroscopic quantum states in a single-Cooper-pair box". In: *Nature* 398.6730 (1999), pp. 786–788. DOI: `10.1038/19718`.

[21] Michel H. Devoret and Les Houches. "Quantize electrical circuits". In: *Quantum Informatics*

6Th September (2011), pp. 1–10.

[22]   Fei Yan, Simon Gustavsson, Archana Kamal, Jeffrey Birenbaum, Adam P. Sears, David Hover, Ted J. Gudmundsen, Danna Rosenberg, Gabriel Samach, S. Weber, Jonilyn L. Yoder, Terry P. Orlando, John Clarke, Andrew J. Kerman, and William D. Oliver. "The flux qubit revisited to enhance coherence and reproducibility". In: *Nature Communications* 7 (2016), pp. 1–9. DOI: `10.1038/ncomms12964`. URL: `http://dx.doi.org/10.1038/ncomms12964`.

[23]   Morten Kjaergaard, Mollie E. Schwartz, Jochen Braumüller, Philip Krantz, Joel I-Jan Wang, Simon Gustavsson, and William D. Oliver. "Superconducting Qubits: Current State of Play". In: (2019). URL: `http://arxiv.org/abs/1905.13641`.

[24]   John M. Martinis, S. Nam, J. Aumentado, and C. Urbina. *Rabi Oscillations in a Large Josephson-Junction Qubit*. Tech. rep. 11. 2002. DOI: `10.1103/PhysRevLett.89.117901`.

[25]   K. B. Cooper, M. Steffen, R. McDermott, R. W. Simmonds, Seongshik Oh, D. A. Hite, D. P. Pappas, and J. M. Martinis. "Observation of Quantum Oscillations between a Josephson Phase Qubit and a Microscopic Resonator Using Fast Readout". In: *Physical Review Letters* 93.18 (2004). DOI: `10.1103/PhysRevLett.93.180401`. URL: `ftp://ftp.boulder.nist.gov/pub/pappas/Talks/QC/2004%20PRL%20oscillations.pdf`.

[26]   Jens Koch, Terri M. Yu, Jay Gambetta, A. A. Houck, D. I. Schuster, J. Majer, Alexandre Blais, M. H. Devoret, S. M. Girvin, and R. J. Schoelkopf. "Charge-insensitive qubit design derived from the Cooper pair box". In: *Physical Review A - Atomic, Molecular, and Optical Physics* 76.4 (2007). DOI: `10.1103/PhysRevA.76.042319`. URL: `http://ee.princeton.edu/research/aahouck/sites/default/files/publications/reprints/PhysRevA_76_042319.pdf`.

[27]   K. K. Likharev and V. K. Semenov. "RSFQ Logic/Memory Family: A New Josephson-Junction Technology for Sub-Terahertz-Clock-Frequency Digital Systems". In: *IEEE Transactions on Applied Superconductivity* 1.1 (1991), pp. 3–28. DOI: `10.1109/77.80745`. URL: `http://ieeexplore.ieee.org/xpls/abs_all.jsp?arnumber=80745`.

[28]   W. Chen, A. V. Rylyakov, Vijay Patel, J. E. Lukens, and K. K. Likharev. "Rapid single flux quantum t-flip flop operating up to 770 GHz". In: *IEEE Transactions on Applied Superconductivity* 9.2

PART 3 (1999), pp. 3212–3215. DOI: `10.1109/77.783712`.

[29] Quentin P. Herr and Anna Y. Herr. "Ultra-low-power superconductor logic". In: *Journal of Applied…* (Mar. 2011). URL: `http://arxiv.org/abs/1103.4269%20http://www.arxiv.org/pdf/1103.4269.pdf%20http://scitation.aip.org/content/aip/journal/jap/109/10/10.1063/1.3585849`.

[30] D. E. Kirichenko, S. Sarwana, and A. F. Kirichenko. "Zero static power dissipation biasing of RSFQ circuits". In: *IEEE Transactions on Applied Superconductivity* 21.3 PART 1 (2011), pp. 776–779. DOI: `10.1109/TASC.2010.2098432`.

[31] O. A. Mukhanov. "Energy-Efficient Single Flux Quantum Logic". In: *Applied Superconductivity, IEEE Transactions on* 21.3 (2014), pp. 760–769. URL: `http://ieeexplore.ieee.org/xpls/abs_all.jsp?arnumber=5682046`.

[32] Mark B. Ketchen, John Timmerwilke, G. W. Gibson, and Manjul Bhushan. "ERSFQ Power Delivery: A Self-Consistent Model/Hardware Case Study". In: *IEEE Transactions on Applied Superconductivity* 29.7 (2019), pp. 1–11. DOI: `10.1109/TASC.2019.2907690`.

[33] T. Filippov, M. Dorojevets, A. Sahu, A. Kirichenko, C. Ayala, and O. Mukhanov. "8-bit asynchronous wave-pipelined RSFQ Arithmetic-Logic Unit". In: *IEEE Transactions on Applied Superconductivity* 21.3 PART 1 (2011), pp. 847–851. DOI: `10.1109/TASC.2010.2103918`. URL: `https://www.researchgate.net/publication/224217904`.

[34] Guang Ming Tang, Kensuke Takata, Masamitsu Tanaka, Akira Fujimaki, Kazuyoshi Takagi, and Naofumi Takagi. "4-bit Bit-Slice Arithmetic Logic Unit for 32-bit RSFQ Microprocessors". In: *IEEE Transactions on Applied Superconductivity* 26.1 (2016), pp. 1–6. DOI: `10.1109/TASC.2015.2507125`.

[35] Ryo Sato, Yuki Hatanaka, Yuki Ando, Masamitsu Tanaka, Akira Fujimaki, Kazuyoshi Takagi, and Naofumi Takagi. "High-Speed Operation of Random-Access-Memory-Embedded Microprocessor with Minimal Instruction Set Architecture Based on Rapid Single-Flux-Quantum Logic". In: *IEEE Transactions on Applied Superconductivity* 27.4 (2017), pp. 1–5. DOI: `10.1109/TASC.2016.2642049`.

[36]   Oleg A. Mukhanov, Dmitri Kirichenko, Igor V. Vernik, Timur V. Filippov, Alexander Kirichenko, Robert Webber, Vladimir Dotsenko, Andrel Talalaevskii, Jia Cao Tang, Anubhav Sahu, Pavel Shevchenko, Robert Miller, Steven B. Kaplan, Saad Sarwana, and Deepnarayan Gupta. "Superconductor digital-RF receiver systems". In: *IEICE Transactions on Electronics* E91-C.3 (2008), pp. 306–317. DOI: `10.1093/ietele/e91-c.3.306`.

[37]   P. Krantz, M. Kjaergaard, F. Yan, T. P. Orlando, S. Gustavsson, and W. D. Oliver. "A quantum engineer's guide to superconducting qubits". In: *Applied Physics Reviews* 6.2 (2019), pp. 1–57. DOI: `10.1063/1.5089550`. URL: `https://arxiv.org/pdf/1904.06560.pdf%20https://doi.org/10.1063/1.5089550`.

[38]   D. Sank. "Fast, Accurate State Measurement in Superconducting Qubits". PhD thesis. University of California Santa Barbara, 2014.

[39]   S. A. Caldwell, N. Didier, C. A. Ryan, and E. A. Sete. "Parametrically Activated Entangling Gates Using Transmon Qubits". In: *Physical Review Applied* 10.3 (Sept. 2018). DOI: `10.1103/PhysRevApplied.10.034050`.

[40]   J. Raftery, A. Vrajitoarea, G. Zhang, Z. Leng, S. J. Srinivasan, and A. A. Houck. "Direct digital synthesis of microwave waveforms for quantum computing". In: (2017), pp. 1–6. URL: `http://arxiv.org/abs/1703.00942`.

[41]   R. McDermott and M. G. Vavilov. "Accurate Qubit Control with Single Flux Quantum Pulses". In: *Physical Review Applied* 2.1 (2014). DOI: `10.1103/PhysRevApplied.2.014007`.

[42]   Edward Leonard. "Digital Control of Superconducting Quantum Bits". PhD thesis. University of Wisconsin-Madison, 2018.

[43]   Sidney Shapiro. "Josephson currents in Superconducting tunneling: The effect of microwaves and other observations". In: *Physical Review Letters* 11.2 (1963), pp. 80–82. DOI: `10.1103/PhysRevLett.11.80`.

[44]   J. Chow, J. M. Gambetta, L. Tornberg, Jens Koch, Lev S. Bishop, A. A. Houck, B. R. Johnson, L. Frunzio, S. M. Girvin, and R. J. Schoelkopf. "Randomized benchmarking and process tomography for gate errors in a solid-state qubit". In: *Physical Review Letters* 102.9 (2009), pp. 1–4.

DOI: `10.1103/PhysRevLett.102.090502`.

[45] Easwar Magesan, Jay M. Gambetta, and Joseph Emerson. "Characterizing quantum gates via randomized benchmarking". In: *Physical Review A - Atomic, Molecular, and Optical Physics* 85.4 (2012), pp. 1–16. DOI: `10.1103/PhysRevA.85.042311`.

[46] D. Rosenberg, S. Weber, D. Conway, D. Yost, J. Mallek, G. Calusine, R. Das, D. Kim, M. Schwartz, W. Woods, J. L. Yoder, and W. D. Oliver. "3D integration and packaging for solid-state qubits". In: (2019). URL: `http://arxiv.org/abs/1906.11146`.

[47] P. J. Liebermann and F. K. Wilhelm. "Optimal Qubit Control Using Single-Flux Quantum Pulses". In: *Physical Review Applied* 6.2 (2016). DOI: `10.1103/PhysRevApplied.6.024022`.

[48] Kangbo Li, R. McDermott, and Maxim G. Vavilov. *Hardware-Efficient Qubit Control with Single-Flux-Quantum Pulse Sequences*. Tech. rep. 1. 2019. DOI: `10.1103/PhysRevApplied.12.014044`. URL: `http://arxiv.org/abs/1902.02911`.

[49] A. Blais, RS Huang, and A. Wallraff. "Cavity quantum electrodynamics for superconducting electrical circuits: An architecture for quantum computation". en. In: *Physical Review A* 69.6 (June 2004). DOI: `10.1103/PhysRevA.69.062320`. URL: `http://link.aps.org/doi/10.1103/PhysRevA.69.062320%20http://pra.aps.org/abstract/PRA/v69/i6/e062320`.

[50] E. T. Jaynes and F. W. Cummings. "Comparison of Quantum and Semiclassical Radiation Theories with Application to the Beam Maser". In: *Proceedings of the IEEE* 51.1 (1963), pp. 89–109. DOI: `10.1109/PROC.1963.1664`.

[51] Diego Ristè, Brian Donovan, Thomas A. Ohki, Colm A. Ryan, and Blake R. Johnson. "Hardware for dynamic quantum computing". In: *Review of Scientific Instruments* 88.10 (2017), p. 104703. DOI: `10.1063/1.5006525`.

[52] Sebastian Krinner, Simon Storz, Philipp Kurpiers, Paul Magnard, Johannes Heinsoo, Raphael Keller, Janis Luetolf, Christopher Eichler, and A. Wallraff. "Engineering cryogenic setups for 100-qubit scale superconducting circuit systems". In: (2018). DOI: `10.1287/ijoc.1090.0342`. URL: `http://arxiv.org/abs/1806.07862`.

[53] R. Barends, J. Wenner, M. Lenander, Y. Chen, R. C. Bialczak, J. Kelly, E. Lucero, P. O'Malley,

M. Mariantoni, D. Sank, H. Wang, T. C. White, Y. Yin, J. Zhao, A. N. Cleland, John M. Martinis, and J. J A Baselmans. "Minimizing quasiparticle generation from stray infrared light in superconducting quantum circuits". In: *Applied Physics Letters* 99.11 (2011), pp. 99–101. DOI: 10.1063/1.3638063.

[54]   Antonio D. Córcoles, J. Chow, Jay M. Gambetta, Chad Rigetti, J. R. Rozen, George A. Keefe, Mary Beth Rothwell, Mark B. Ketchen, and M. Steffen. *Protecting superconducting qubits from radiation*. Tech. rep. 18. 2011. DOI: 10.1063/1.3658630. URL: http://arxiv.org/abs/1108.1383%0Ahttp://dx.doi.org/10.1063/1.3658630.

[55]   M. D. Reed, L. Dicarlo, B. R. Johnson, L. Sun, D. I. Schuster, L. Frunzio, and R. J. Schoelkopf. *High-fidelity readout in circuit quantum electrodynamics using the jaynes-cummings nonlinearity*. Tech. rep. 17. 2010. DOI: 10.1103/PhysRevLett.105.173601.

[56]   Bernard Yurke and John S Denker. "Quantum network theory Bernard". In: *Physical Review A* 29.3 (1984), pp. 1419–1437.

[57]   N. Bergeal, R. Vijay, V. E. Manucharyan, I. Siddiqi, R. J. Schoelkopf, S. M. Girvin, and M. H. Devoret. *Analog information processing at the quantum limit with a Josephson ring modulator*. Tech. rep. 4. 2010, pp. 296–302. DOI: 10.1038/nphys1516.

[58]   C. Macklin, K. O'Brien, D. Hover, M. E. Schwartz, V. Bolkhovsky, X. Zhang, W. D. Oliver, and I. Siddiqi. "A near-quantum-limited Josephson traveling-wave parametric amplifier". In: *Science* 350.6258 (2015), pp. 307–310. DOI: 10.1126/science.aaa8525.

[59]   Byeong Ho Eom, Peter K. Day, Henry G. Leduc, and Jonas Zmuidzinas. "A wideband, low-noise superconducting amplifier with high dynamic range". In: *Nature Physics* 8.8 (2012), pp. 623–627. DOI: 10.1038/nphys2356. URL: www.nature.com/naturephysics.

[60]   J. Kelly, R. Barends, A. G. Fowler, A. Megrant, E. Jeffrey, T. C. White, D. Sank, J. Y. Mutus, B. Campbell, Y. F. Chen, Z. Chen, B. Chiaro, A. Dunsworth, I. C. Hoi, C. Neill, P. J. O'Malley, C. Quintana, P. Roushan, A. Vainsencher, J. Wenner, A. N. Cleland, and J. M. Martinis. "State preservation by repetitive error detection in a superconducting quantum circuit". In: *Nature* 519.7541 (Mar. 2015), pp. 66–69. DOI: 10.1038/nature14270. URL: http://dx.doi.org/10.1038/

`nature14270%20http://10.0.4.14/nature14270%20https://www.nature.com/articles/`
`nature14270#supplementary-information`.

[61] J. Y. Mutus, T. C. White, R. Barends, Yu Chen, Z. Chen, B. Chiaro, A. Dunsworth, E. Jeffrey, J. Kelly, A. Megrant, C. Neill, P. J.J. O'Malley, P. Roushan, D. Sank, A. Vainsencher, J. Wenner, K. M. Sundqvist, A. N. Cleland, and John M. Martinis. "Strong environmental coupling in a Josephson parametric amplifier". In: *Applied Physics Letters* 104.26 (2014). DOI: `10.1063/1.4886408`. URL: `http://dx.doi.org/10.1063/1.4886408`.

[62] Luke C.G. Govia, E. J. Pritchett, Canran Xu, B. L. T. Plourde, Maxim G. Vavilov, Frank K. Wilhelm, and R. McDermott. "High-fidelity qubit measurement with a microwave-photon counter". In: *Physical Review A - Atomic, Molecular, and Optical Physics* 90.6 (2014), p. 62307. DOI: `10.1103/PhysRevA.90.062307`. URL: `https://journals.aps.org/pra/pdf/10.1103/PhysRevA.90.062307`.

[63] Y. F. Chen, D. Hover, S. Sendelbach, L. Maurer, S. T. Merkel, E. J. Pritchett, F. K. Wilhelm, and R. McDermott. "Microwave photon counter based on josephson junctions". In: *Physical Review Letters* 107.21 (2011), p. 217401. DOI: `10.1103/PhysRevLett.107.217401`. URL: `http://prl.aps.org/abstract/PRL/v107/i21/e217401`.

[64] G. J. Ribeill. "Qubit Readout with the Josephson Photomultiplier". PhD thesis. University of Wisconsin, Madison, 2016.

[65] R. W. Simmonds, K. M. Lang, D. A. Hite, S. Nam, D. P. Pappas, and John M. Martinis. *Decoherence in josephson phase qubits from junction resonators*. Tech. rep. 7. 2004. DOI: `10.1103/PhysRevLett.93.077003`.

[66] D. I. Schuster, A. Wallraff, A. Blais, and L. Frunzio. "ac Stark shift and dephasing of a superconducting qubit strongly coupled to a cavity field". In: *Physical review …* 94.12 (Mar. 2005). DOI: `10.1103/PhysRevLett.94.123602`. URL: `http://arxiv.org/abs/cond-mat/0408367%20http://www.arxiv.org/pdf/cond-mat/0408367.pdf%20http://prl.aps.org/abstract/PRL/v94/i12/e123602`.

[67] Dmitri V. Averin, Kristian Rabenstein, and V. K. Semenov. "Rapid ballistic readout for flux qubits".

In: *Physical Review B - Condensed Matter and Materials Physics* 73.9 (2006). DOI: `10.1103/PhysRevB.73.094504`.

[68] C. H. Van der Wal, A. C.J. Ter Haar, F. K. Wilhelm, R. N. Schouten, C. J.P.M. Harmans, T. P. Orlando, S. Lloyd, and J. E. Mooij. "Quantum superposition of macroscopic persistent-current states". In: *Science* 290.5492 (2000), pp. 773–777. DOI: `10.1126/science.290.5492.773`. URL: `www.sciencemag.orghttp://science.sciencemag.org/`.

[69] Arkady Fedorov, Alexander Shnirman, Gerd Schön, and Anna Kidiyarova-Shevchenko. "Reading out the state of a flux qubit by Josephson transmission line solitons". In: *Physical Review B - Condensed Matter and Materials Physics* 75.22 (2007), pp. 1–13. DOI: `10.1103/PhysRevB.75.224504`.

[70] Anna Y. Herr, Arkady Fedorov, Alexander Shnirman, E. Il'Ichev, and Gerd Schön. "Design of a ballistic fluxon qubit readout". In: *Superconductor Science and Technology* 20.11 (2007). DOI: `10.1088/0953-2048/20/11/S29`.

[71] I. I. Soloviev, N. V. Klenov, A. L. Pankratov, E. Il'Ichev, and L. S. Kuzmin. "Effect of Cherenkov radiation on the jitter of solitons in the driven underdamped Frenkel-Kontorova model". In: *Physical Review E - Statistical, Nonlinear, and Soft Matter Physics* 87.6 (2013), pp. 1–5. DOI: `10.1103/PhysRevE.87.060901`.

[72] I. I. Soloviev, N. V. Klenov, S. V. Bakurskiy, A. L. Pankratov, and L. S. Kuzmin. "Symmetrical Josephson vortex interferometer as an advanced ballistic single-shot detector". In: *Applied Physics Letters* 105.20 (2014). DOI: `10.1063/1.4902327`.

[73] I. I. Soloviev, N. V. Klenov, A. L. Pankratov, L. S. Revin, E. Il'ichev, and L. S. Kuzmin. "Soliton scattering as a measurement tool for weak signals". In: *Physical Review B - Condensed Matter and Materials Physics* 92.1 (2015), pp. 1–8. DOI: `10.1103/PhysRevB.92.014516`.

[74] N. V. Klenov, A. V. Kuznetsov, I. I. Soloviev, S. V. Bakurskiy, M. V. Denisenko, and A. M. Satanin. "Flux qubit interaction with rapid single-flux quantum logic circuits: Control and readout". In: *Low Temperature Physics* 43.7 (2017), pp. 789–798. DOI: `10.1063/1.4995627`.

[75] Kirill Fedorov, Anastasia V. Shcherbakova, Michael J. Wolf, Detlef Beckmann, and A. V. Ustinov.

"Fluxon readout of a superconducting qubit". In: *Physical Review Letters* 112.16 (2014), pp. 1–5. DOI: `10.1103/PhysRevLett.112.160502`.

[76]   Samuel Intiso, Jukka Pekola, Alexander Savin, Ygor Devyatov, and Anna Kidiyarova-Shevchenko. "Rapid single-flux-quantum circuits for low noise mK operation". In: *Superconductor Science and Technology* 19.5 (May 2006), S335–S339. DOI: `10.1088/0953-2048/19/5/S36`.

[77]   R. McDermott, M. G. Vavilov, B. L. T. Plourde, F. K. Wilhelm, P. J. Liebermann, O. A. Mukhanov, and T. A. Ohki. "Quantum-classical interface based on single flux quantum digital logic". In: *Quantum Science and Technology* 3.2 (2018), pp. 1–16. DOI: `10.1088/2058-9565/aaa3a0`. URL: `http://arxiv.org/abs/1710.04645%0Ahttp://dx.doi.org/10.1088/2058-9565/aaa3a0%20https://doi.org/10.1088/2058-9565/aaa3a0`.

[78]   S. V. Rylov, L.a. Bunz, D.V. Gaidarenko, M.a. Fisher, R.P. Robertazzi, and O. A. Mukhanov. "High resolution ADC system". In: *IEEE Transactions on Appiled Superconductivity* 7.2 (1997), pp. 2649–2652. DOI: `10.1109/77.621783`. URL: `http://ieeexplore.ieee.org/lpdocs/epic03/wrapper.htm?arnumber=621783`.

[79]   S. Whiteley. *wrcad.com*.

[80]   Pavel Shevchenko. *pscan2sim.org*. URL: `pscan2sim.org`.

[81]   *HYPRES Design Rules: https://www.hypres.com/wp-content/uploads/2010/11/DesignRules-6.pdf*. URL: `https://www.hypres.com/wp-content/uploads/2010/11/DesignRules-6.pdf`.

[82]   Thomas J. Walls, Timur V. Filippov, and Konstantin K. Likharev. "Quantum Fluctuations in Josephson Junction Comparators". In: *Physical Review Letters* 89.21 (2002). DOI: `10.1103/PhysRevLett.89.217004`. URL: `https://journals.aps.org/prl/pdf/10.1103/PhysRevLett.89.217004`.

[83]   Michael Wulf, Xingxiang Zhou, Jonathan L. Habif, Pavel Rott, Mark F. Bocko, and M.J. Feldman. "An unshunted comparator as a device for quantum measurements". In: *IEEE Transactions on Applied Superconductivity* 13.2 I (June 2003), pp. 974–977. DOI: `10.1109/TASC.2003.814117`. URL: `http://ieeexplore.ieee.org/document/1211768/`.

[84]   T. A. Ohki, Michael Wulf, M.J. Feldman, and Mark F. Bocko. "Unshunted QOS Comparator

for Qubit Readout". In: *Journal of Physics: Conference Series* 43.1 (June 2006), pp. 1413–1416. DOI: `10.1088/1742-6596/43/1/346`. URL: `http://stacks.iop.org/1742-6596/43/i=1/a=346?key=crossref.c7e77671116c4a75baca9c1b3eec44f1`.

[85] Thomas J. Walls, Dmitri V. Averin, and K. K. Likharev. "Josephson junction comparator as a quantum-limited detector for flux qubit readout". In: *IEEE Transactions on Applied Superconductivity* 17.2 (June 2007), pp. 136–141. DOI: `10.1109/TASC.2007.898632`. URL: `http://ieeexplore.ieee.org/document/4277792/`.

[86] Tom Ohki, Alexander Savin, Juha Hassel, Leif Grönberg, Tatiana Karminskaya, and A Kidiyarova-Shevchenko. "Balanced comparator for RSFQ qubit readout". In: *IEEE Transactions on Applied Superconductivity* 17.2 (June 2007), pp. 128–131. DOI: `10.1109/TASC.2007.897319`. URL: `http://ieeexplore.ieee.org/document/4277641/`.

[87] H. Ko and Theodore Van Duzer. "A New High-speed Periodic-Threshold Comparator for Use in a Josephson A/D Converter". In: *IEEE Journal of Solid-State Circuits* 23.4 (1988), pp. 1017–1021. DOI: `10.1109/4.355`.

[88] Paul Bradley and Huan Dang. *Design and Testing of Quasi-One Junction SQUID-Based Comparators at Low and High Speed for Superconductive Flash A/D Converters*. 1991. DOI: `10.1109/77.84627`.

[89] Darren K. Brock, Stephen S. Martinet, Mark F. Bocko, and John X. Przybysz. "Design and Testing of QOS Comparators for an RSFQ Based Analog to Digital Converter". In: *IEEE Transactions on Applied Superconductivity* 5.2 (June 1995), pp. 2244–2247. DOI: `10.1109/77.403032`. URL: `http://ieeexplore.ieee.org/document/403032/`.

[90] T.V. Filippov. "Quantum dissipation properties of a Josephson balanced comparator". In: *American Institute of Physics* (1995). URL: `http://jetpletters.ac.ru/ps/1209/article_18279.pdf`.

[91] F.C. Wellstood, C. Urbina, and John Clarke. "Hot-electron effects in metals". In: *Physical Review B* 49.9 (1994), pp. 5942–5955. URL: `http://journals.aps.org/prb/abstract/10.1103/PhysRevB.49.5942`.

[92] J. M. Martinis, K. B. Cooper, R. McDermott, M. Steffen, M. Ansmann, K. D. Osborn, K. Cicak, Seongshik Oh, D. P. Pappas, R. W. Simmonds, and Clare C. Yu. "Decoherence in Josephson qubits from dielectric Loss". In: *Physical Review Letters* 95.21 (Nov. 2005), pp. 1–4. DOI: `10.1103/PhysRevLett.95.210503`. URL: `https://link.aps.org/doi/10.1103/PhysRevLett.95.210503`.

[93] Dmitry Y. Zinoviev and Y. A. Polyakov. "Octopux: An advanced automated setup for testing superconductor circuits". In: *IEEE Transactions on Applied Superconductivity* 7.2 PART 3 (1997), pp. 3240–3243. DOI: `10.1109/77.622039`.

[94] Olivia Chen, Ruizhe Cai, Yanzhi Wang, Fei Ke, Taiki Yamae, Ro Saito, Naoki Takeuchi, and Nobuyuki Yoshikawa. "Adiabatic Quantum-Flux-Parametron: Towards Building Extremely Energy-Efficient Circuits and Systems". In: *Scientific Reports* 9.1 (2019). DOI: `10.1038/s41598-019-46595-w`. URL: `https://doi.org/10.1038/s41598-019-46595-w`.

[95] E. Charbon, F. Sebastiano, A. Vladimirescu, H. Homulle, S. Visser, L. Song, and R. M. Incandela. "Cryo-CMOS for quantum computing". In: *Technical Digest - International Electron Devices Meeting, IEDM* (2017), pp. 1–13. DOI: `10.1109/IEDM.2016.7838410`.

[96] Joseph C. Bardin, Evan Jeffrey, Erik Lucero, Trent Huang, Ofer Naaman, Rami Barends, Ted White, Marissa Giustina, Daniel Sank, Pedram Roushan, Kunal Arya, Benjamin Chiaro, Julian Kelly, Jimmy Chen, Brian Burkett, Yu Chen, Andrew Dunsworth, Austin Fowler, Brooks Foxen, Craig Gidney, Rob Graff, Paul Klimov, Josh Mutus, Matthew McEwen, Anthony Megrant, Matthew Neeley, Charles Neill, Chris Quintana, Amit Vainsencher, Hartmut Neven, and John Martinis. "29.1 A 28nm Bulk-CMOS 4-to-8GHz ¡2mW Cryogenic Pulse Modulator for Scalable Quantum Computing". In: *Digest of Technical Papers - IEEE International Solid-State Circuits Conference* 2019-Febru (2019), pp. 456–458. DOI: `10.1109/ISSCC.2019.8662480`.

[97] H. J. Van Weers, G. Kunkel, M. A. Lindeman, and M. Leeman. "Niobium flex cable for low temperature high density interconnects". In: *Cryogenics* 55-56 (2013), pp. 1–4. DOI: `10.1016/j.cryogenics.2012.10.006`. URL: `http://dx.doi.org/10.1016/j.cryogenics.2012.10.006`.

Vita

NAME	Caleb Jordan Howington
PLACE OF BIRTH	Morristown, Tennessee, United States of America
DATE OF BIRTH	August 20, 1992

EDUCATION

B.S. Physics, Rensselaer Polytechnic Institute, December 2013

PROFESSIONAL EXPERIENCE

Teaching Assistant, Syracuse University Department of Physics	2014
Research Assistant, Plourde Research Lab, Syracuse University Department of Physics	2014-2019
Trained User, Cornell Nanoscale Facility	2015-2019

PUBLICATIONS

C. Howington, A. Opremcak, A. Kirechenko, O. Mukhanov, R. McDermott, B.L.T. Plourde. Interfacing superconductingqubits with cryogenic digital logic: Measurement. *IEEE Transactions on Applied Superconductivity* 29.5, 2019

E. Leonard, M. A. Beck, J. Nelson, B.G. Christensen, T. Thorbeck, **C. Howington**, A. Opremcak, I.V. Pechenezhskiy, K. Dodge, N.P. Dupuis, M.D. Hutchings, J. Ku, F. Schlenker, J. Suttle, C. Wilen, S. Zhu,

M.G. Vavilov, B.L.T. Plourde, and R. McDermott. Digital coherent control of a superconducting qubit. *Phys. Rev. Applied*, 11:014009, 2019

A. Opremcak, I. V. Pechenezhskiy, **C. Howington**, B. G. Christensen, M. A. Beck, E. Leonard, J. Suttle, C. Wilen, K. N. Nesterov, G. J. Ribeill, T. Thorbeck, F. Schlenker, M. G. Vavilov, B. L. T. Plourde, and R. McDermott. Measurement of a superconducting qubit with a microwave photon counter. *Science*, 361(6408):1239–1242, 2018

PRESENTATIONS

2019	APS March Meeting	Design of a Cryogenic, Digital Measurement Circuit for Superconducting Qubits
2018	APS March Meeting	Cryogenic Digital Readout of Superconducting Qubits
	ASC	Interfacing superconducting qubits with cryogenic digital logic: Measurement
2017	APS March Meeting	Parity detection of multiple superconducting qubits
2016	APS March Meeting	Multi-qubit measurements with a Josephson Photomultiplier
	ASC	Qubit parity measurements with a Josephson Photomultplier
2015	APS March Meeting	Readout of superconducting qubits with a Josephson Photomultiplier